DEVELOPING A MULTIFUNCTIONAL NANOCOMPOSITE USING ALBUMIN-ENCAPSULATED RARE-EARTH DOPED NANOPARTICLES FOR TUMOR TARGETING

by

DOMINIK JAN NACZYNSKI

A Dissertation submitted to the

Graduate School-New Brunswick

Rutgers, The State University of New Jersey

in partial fulfillment of the requirements

for the degree of

Doctor of Philosophy

Graduate Program in Chemical and Biochemical Engineering

written under the direction of

Dr. Prabhas V. Moghe and Dr. Charles M. Roth

and approved by

_____

_____

_____

_____

_____

New Brunswick, New Jersey

October 2012

ABSTRACT OF THE DISSERTATION

Developing a Multifunctional Nanocomposite using Albumin-Encapsulated Rare-Earth Doped Nanoparticles for Tumor Targeting

By DOMINIK JAN NACZYNSKI

Dissertation Director:

Dr. Prabhas V. Moghe and Dr. Charles M. Roth

Optically guided imaging of diseases and surgical procedures is challenged by the lack of photoluminescent probes that can be sensitively detected within living tissues and tracked in real-time. The use of visible light for the detection of conventional probes suffers from poor tissue penetration and non-specific fluorescence. Emerging probes excited using near infrared light (NIR) reduce undesired tissue absorbance, however light scattering resulting from the complex heterogeneity of biological tissues limits the penetration depth of light propagation. Optical probes that emit over a new window of electromagnetic radiation in the short wavelength infrared (SWIR) region can significantly improve in vivo imaging sensitivity compared to NIR. However, current SWIR-detectable probes lack the optical tunability and biocompatibility requisite for biological implantation in vivo.

This doctoral dissertation is focused on investigating albumin-derived, biologically interactive nanoparticles as a platform system that can be designed with

distinct multifunctional properties, particularly, SWIR imaging and the delivery of therapeutic cargo. The bulk of the thesis is focused on conceptualizing and developing a new class of SWIR-detectable nanomaterials for targeted imaging of cancerous tissues. Conventionally fabricated rare-earth doped nanoprobes (REs) are weakly bioavailable, lack functional surface groups for tissue targeting and exhibit potential cytotoxicity. A major research effort of this thesis was to develop albumin nanoshells around rare-earth nanoprobes for establishing highly biocompatible and biologically targetable RE nanocomposites with controlled sizes and pharmacodynamic behaviors.

This study also produced the first evidence reported to date of multi-spectral, real-time SWIR imaging at anatomical resolution in vivo and demonstrated the prospects of REs for targeted molecular imaging. The albumin-encapsulated, inorganic-organic nanocomposite of REs showed enhanced SWIR signal intensity in diseased tissue through accumulation of REs at tumor sites and extended the *in vivo* retention of REs. Further modifications were made to the albumin coating to create a multifunctional nanoparticle with tumor-penetrating and therapeutic delivery properties for both imaging and drug delivery applications.

The cumulative findings of this thesis lay the groundwork for the design of new biomedical probes and imaging methods that have the potential to significantly advance surveillance of a range of diseases with complex molecular etiologies, from cancers to heart disease.

ACKNOWLEDGEMENTS

Although the path toward the completion of my doctoral research has been a profoundly personal and self-challenging experience, I could not have accomplished the work presented in this thesis with the support of numerous individuals.

The support, freedom and opportunities that both Dr. Prabhas Moghe and Dr. Charles Roth, my thesis advisors, have provided over the years have allowed me to grow as a scientist and as an individual. Their mentorship has fundamentally changed the way I approach science and given me strength, confidence and a foundation on which (not "that") I can build my scientific career. Prabhas and Charlie, with my deepest gratitude, thank you.

Next I would like to thank our collaborator, Dr. Richard Riman. Rik has given me an enormous amount of advice over the years, providing guidance both academically and professionally. His expertise and perspective have helped advance and shape this project into something truly exciting.

My warmest gratitude goes to Dr. Suzie Chen, who adopted me into her group toward the end of my degree. Suzie has been instrumental in the progression and development of all animal studies presented here. I am very fortunate to have met a professor as inspiring as her. Suzie, thank you so much for welcoming me into your lab and for the support you have given me.

I also thank the fifth member of my committee Dr. Patrick Sinko, who has provided objectivity and perspective on my research. He has also offered valuable guidance on my future career and I thank him for his time and advice.

Next I would like to thank my funding sources, including the Rutgers - UMDNJ Biotechnology Training Program. They have given me the opportunity to conduct my research and supported my travel to numerous conferences. The feedback and exposure my work has received at these conferences has been invaluable toward my degree.

I also thank Dr. Martin Yarmush who has been an inspirational figure to me. His mentorship and intellectual advice have helped guide me over the years. I thank Dr. Mark Pierce for his technical guidance in optical imaging.

Not every graduate student is fortunate to work with a dedicated post-doctoral mentor who is both patient and willing to train a new scientist. I was fortunate to have the guidance of several. Dr. Tamar Andelman and Dr. Mei Chee Tan, thank you for your advice, support and showing me what it means to be a good scientist. I also thank Dr. Adam York, Dr. Craig Griffith and Dr. Maria "Pia" Rossi who have all guided me through the difficulties of this degree.

I thank Brian Wall for the time he took away from his own thesis to assist me with the animal work presented in this thesis. His dedication has been without question, and the training he has provided me has been as invaluable as the friendship I gained. I also thank Margot Zevon for her assistance in many aspects of this work, including the analysis of tissue samples. I am proud that she will be the graduate student who will continue my work. I wish her the best and have every confidence in her ability to succeed.

I thank the undergraduates who have assisted me in my research, including Anthony Kulesa, Kyle Minor and David Pal. Tony's contribution to my project has far exceeded my expectations and I expect he will have great success as a scientist in the

future. Both Kyle and Dave have assisted me in the development of several research projects, while aiding in my development as a scientific teacher and mentor. I wish them many successes in their futures.

My experience at Rutgers was strongly influenced by my friends in the graduate program. Their friendships have guided me through both research and life. I have gained remarkable colleagues and lifelong friends. I especially would like to thank Jocie, Lavanya, Jeff, Dan, Sebastian, Joe, George, Kapil, Jing, Aina and Carolyn for helping me.

I would like to thank the Esparza family for their support, and particularly Patty, who helped edit much of this thesis. I would also like to thank my old friends from high school and Cornell who were always eager to remind me that I was still a student, which gave me ample motivation to complete my degree.

And for all those who I have not mentioned, but have helped me over these years – I thank you.

DEDICATION

This work is dedicated to my family, whose love and support have given me the strength to work with all my ability and finish this degree. Their support has helped me to overcome the hardest challenges I have faced during my doctoral research. From the bottom of my heart, thank you.

My father, Marian Naczynski, has been my role model. He introduced me to science and mathematics at an early age, fostering my intellectual growth all throughout my life. He is my teacher and my inspiration. He kept science fascinating, captivating my attention with our first telescope, allowing my scientific curiosities to be explored with a basement laboratory and helping me understand scientific principles with countless science projects. Dad, thank you so much for supporting me during my studies and throughout my life. I have nothing but respect for you and I hope I have made you proud.

My mother, Aniela Naczynski, has been an infinite source of love and support. She has been a constant source of advice and inspiration in all aspects of my life. Watching her tireless work ethic as I grew up has molded me into the person that I am today. Mom, thank you for listening to me, taking care of me and showing me what unconditional love truly means.

And to Erica Esparza, you have been my source of strength. Your love, patience, honesty and support have given me confidence during the hardest times of my degree. For all the presentations you have heard me practice, for all the countless hours I have dragged you into lab, for all the times I have been late because an experiment ran over

and for so much more, thank you. I only hope that we can now make up for all our lost time together.

I love and thank you all.

PRIOR PUBLICATIONS

Several sections of this dissertation have been published elsewhere, or are being prepared for publication. The following publications are acknowledged:

- Chapter 2 has been published in its entirety and has the following citation: **Naczynski, D.J., Andelman, T., Pal, D., Chen, S., Riman, R. E., Roth, C. M., Moghe, P. V.** Albumin nanoshell encapsulation of near-infrared-excitable rare-earth nanoparticles enhances biocompatibility and enables targeted cell imaging. *Small* **6**, 1631-1640 (2010).

- Sections of Chapters 3 and 4 are being prepared for publication elsewhere as part of an article entitled: "Rare-earth doped nanoparticles as bioactive probes for shortwave infrared in vivo imaging" **D.J. Naczynski, M.C. Tan, M. Zevon, B. Wall, J. Kohl, A. Kulesa, S. Chen, C.M. Roth, R.E. Riman, P.V. Moghe**

- Sections of Chapter 5 are currently being prepared for publication elsewhere as part of an article entitled: "Collagenase modified albumin nanoparticles for enhanced tumor penetration and multi-drug delivery" **D.J. Naczynski, M. Zevon, M. Cui, C.M. Roth, P.V. Moghe**

TABLE OF CONTENTS

LIST OF TABLES

LIST OF FIGURES

CHAPTER 1

AN INTRODUCTION TO BIOMEDICAL IMAGING PRINCIPLES AND TECHNIQUES

1.1. Biomedical Imaging

Identification of the molecular species involved in cancer pathogenesis and progression has resulted in more accurate disease prognoses and wider range of clinical treatment strategies, ushering in an age of personalized patient care and molecularly targeted therapies. Technologies for imaging molecular cues and events are ever so critical when monitoring the complex behavior demonstrated by many diseases such as cancer.[1,2] Molecular imaging can provide researchers and clinicians a window into the nature of cancer signaling pathways,[3] allowing researchers to study the mechanisms and hallmarks of cancer in situ. The development of molecular imaging tools and their clinical adoption will have broad implications for drug discovery, prognostic screening, and clinical monitoring.[4] In particular, molecular imaging probes which can monitor and predict treatment response can be used as part of a complementary strategy in the clinic, enabling clinicians to make decisions on whether to change or refine a treatment.[5,6]

Currently, clinical imaging in oncology primarily focuses on the identification and characterization of gross anatomical features such as tumor location, staging, volume and metastasis.[7] These imaging approaches are the most frequently used tools for evaluating cancer clinically,[8,9,7,10-12] and constitute the fastest growing component of healthcare expense in the United States.[8,13] Nonetheless, there is a tremendous return on investment in clinical imaging in the form of improved patient care,[14] more accurate diagnoses,[15-17] and more successful surgical interventions.[18-20] Despite their widespread utility, the most ubiquitous imaging modalities provide limited sensitivity and coarse molecular information at the level of the tumor, leaving untapped the potential of more precise diagnoses that can be used as the basis of patient-specific treatments.[21] Indeed,

present imaging techniques can only detect solid tumors once they have grown over a centimeter in diameter (approximately 10^9 cells), leaving significant uncertainty when cancer is in clinically-determined "remission."[11]

Molecular imaging aims to revolutionize cancer imaging by visualizing biological events on a subcellular level in living systems.[7] Targeted imaging of tumor biomarkers is one of numerous molecular imaging strategies currently being investigated toward improving both the detection and understanding of critical molecular events that promote tumorigenesis. This strategy has great implications for the early detection of cancer, which in turn has been linked to more effective treatment and greater likelihood of survival in patients.[22] By combining the increased sensitivity of molecular imaging with tumor biomarker targeted probes, clinicians will potentially be able to rapidly identify cancer in patients and identify key molecular targets for subsequent treatment.[7] Beyond diagnosis and initial treatment, targeted molecular imaging probes can be utilized to monitor disease progression, such as metastasis, and track the spatio-temporal response of tumors to drug therapies.[21] Combined with conventional imaging approaches, molecular imaging can be integrated with traditional anatomical imaging ultimately leading to a more comprehensive portrait of disease states for improved patient care.

1.2. Overview of Imaging Systems

Imaging modalities can be broadly categorized as primarily anatomical/physiological or primarily molecular imaging systems (**Table 1.1**).[6] Macroscopic imaging systems such as X-ray computed tomography (CT), magnetic resonance imaging (MRI) and ultrasound which provide anatomical and physiological information on disease, are currently used clinically.[23] Molecular imaging systems include optical imaging and nuclear imaging modalities such as positron-emission tomography (PET) and single-photon-emission tomography (SPECT).

Technique	Resolution*	Depth	Time†	Quantitative‡	Multi-channel	Imaging agents	Target	Cost*§	Main small-animal use	Clinical use
MRI	10–100 μm	No limit	Minutes to hours	Yes	No	Paramagnetic chelates, magnetic particles	Anatomical, physiological, molecular	$$$	Versatile imaging modality with high soft-tissue contrast	Yes
CT	50 μm	No limit	Minutes	Yes	No	Iodinated molecules	Anatomical, physiological	$$	Imaging lungs and bone	Yes
Ultrasound	50 μm	cm	Seconds to minutes	Yes	No	Microbubbles	Anatomical, physiological	$$	Vascular and interventional imaging‖	Yes
PET	1–2 mm	No limit	Minutes to hours	Yes	No	^{18}F-, ^{64}Cu- or ^{11}C-labelled compounds	Physiological, molecular	$$$	Versatile imaging modality with many tracers	Yes
SPECT	1–2 mm	No limit	Minutes to hours	Yes	No	^{99m}Tc- or ^{111}In-labelled compounds	Physiological, molecular	$$	Imaging labelled antibodies, proteins and peptides	Yes
Fluorescence reflectance imaging	2–3 mm	<1 cm	Seconds to minutes	No	Yes	Photoproteins, fluorochromes	Physiological, molecular	$	Rapid screening of molecular events in surface-based disease	Yes
FMT	1 mm	<10 cm	Minutes to hours	Yes	Yes	Near-infrared fluorochromes	Physiological, molecular	$$	Quantitative imaging of fluorochrome reporters	In development
Bioluminescence imaging	Several mm	cm	Minutes	No	Yes	Luciferins	Molecular	$$	Gene expression, cell and bacterium tracking	No
Intravital microscopy¶	1 μm	<400–800 μm	Seconds to hours	No	Yes	Photoproteins, fluorochromes	Anatomical, physiological, molecular	$$$	All of the above at higher resolutions but limited depths and coverage	In development#

*For high-resolution, small-animal imaging systems. (Clinical imaging systems differ.) †Time for image acquisition. ‡Quantitative here means inherently quantitative. All approaches allow relative quantification. §Cost is based on purchase price of imaging systems in the United States: $, <US$100,000; $$, US$100,000–300,000; $$$, >US$300,000. ‖Interventional means used for interventional procedures such as biopsies or injection of cells under ultrasound guidance. ¶Laser-scanning confocal or multiphoton microscopy. #For microendoscopy and skin imaging. (Table adapted, with permission, from ref. 85.)

Table 1.1 – Overview of Imaging Systems. Magnetic resonance imaging (MRI); computed tomography (CT); positron-emission tomography (PET); single-photon-emission CT (SPECT); fluorescence-mediated tomography (FMT). This figure was

reproduced from: Weissleder, R. & Pittet, M.J. Imaging in the era of molecular oncology. *Nature* **452**, 580-589 (2008)[4] and Rudin, M. & Weissleder, R. Molecular imaging in drug discovery and development. *Nature Reviews Drug Discovery* **2**, 123-131 (2003).[24]

1.2.1. Properties of Anatomical and Physiological Imaging Modalities

CT uses X-ray attenuation caused by tissues with high atomic numbers (such as calcium-based bone) or exogenous contrast agents to reconstruct a 3-D image in a patient.[11]

Although there are different types of MRI approaches, the fundamental principle relies on the nuclear magnetic resonance properties of hydrogen nuclei in water following an interaction with a strong magnetic field and radio frequency current.[5] This interaction causes a change in the spin of the protons in the magnetic field, which returns to equilibrium or undergoes "relaxation" when the radio frequency current is turned off. Contrast agents, such as gadolinium chelates and iron oxide, shorten the relaxation time of the protons which undergo spin changes, providing a means to distinguish organs and soft tissues. MRI captures the radio frequency signal generated from relaxation to reconstruct a three-dimensional image.

Ultrasound uses high-frequency sound that is transmitted in very short pulses to create echoes from structures within the body. Microbubbles can be used as contrast agents for ultrasound by enhancing the acoustic signal of blood during sound pulsing.[25]

Anatomical and physiological imaging techniques generally exhibit high spatial resolutions in the micron range (50-100 μm), with new MRI techniques capable of spatial

resolutions as small as 10 μm.[5] These techniques also provide imaging data which is inherently quantifiable.[23] Both MRI and CT approaches have no limit on penetration depth enabling full-body imaging, while ultrasound is limited to penetrating through centimeters of tissue.[23] MRI and ultrasound also use non-ionizing energy for visualization, which is relatively safer and less damaging to tissue than ionizing sources.[26-28] Ultrasound techniques however, have excellent temporal resolution, capable of imaging on the order of seconds. MRI and CT approaches generally take minutes, or hours for certain cases of MRI, preventing applicability towards real-time imaging.[4] All anatomical imaging modalities require that the local concentration of exogenous contrast agents must be relatively high for detection, effectively limiting sensitivity.[29]

1.2.2. Molecular Imaging Modalities

Molecular imaging involves the resolution and quantification of fundamental molecular changes that occur during disease at the cellular and subcellular scale.[6] Though recent advances in MRI techniques have pushed the limits of this technology into the molecular domain,[30] nuclear and optical imaging techniques have traditionally been associated with molecular imaging. Future research holds promise for the development of all three approaches (MRI, nuclear and optical) as molecular imaging tools, but the focus here will be on imaging using nuclear and optical technologies.

Both PET and SPECT require the use of a radiotracer that produces γ-rays that are subsequently detected with specialized instrumentation or cameras. Software algorithms are then used for three-dimensional reconstruction of the captured images.[29]

Optical imaging relies on the detection of photons following their interaction with tissue or an exogenous contrast agent to generate visual information. As light travels through increasing depths of tissue, however, photons are either scattered or absorbed reducing optical signal.[31]

Although nuclear and optical imaging techniques generally exhibit poor spatial resolution, they are highly sensitive, capable of detecting contrast agents at the nanomolar to picomolar levels.[29] Both modalities, but in particular optical imaging, are capable of multispectral imaging or the detection of more than one probe signal simultaneously. Nuclear approaches generally exhibit no limit on penetration depth while optical approaches may be able to resolve only at depths of several millimeters.[6] In terms of practicality, however, nuclear approaches generally require expensive machinery, such as cyclotrons for the production of radionuclides, while optical imaging tends to be faster and easier to perform with low cost instruments for near surface imaging.[6,54]

1.2.3. Imaging Modality Integration and Opportunities

Each individual imaging technique has certain advantages and disadvantages. Choosing the appropriate technique is largely dependent on the specific biological questions being asked. Ideally, imaging techniques must have both high spatial resolution as well as the necessary sensitivity to detect small changes in molecular events over time.[6] This has led to the development of multimodal-based imaging approaches, ones that integrate multiple imaging platforms to extract visual information on several spatial scales simultaneously. Clinically, some of the best examples of multimodal imaging systems can be seen with PET-based systems, such as PET-SPECT, PET-CT and PET-

MRI scanner hybrids. Co-registering anatomical and molecular information can provide both the spatial localization and structure of diseases such as cancer as well as functional, metabolic and cellular characteristics.[32,33] In addition, multimodality can also be used for preoperative or intraoperative imaging.[34] For example, MRI- or PET-CT-optical approaches can be used to first identify the anatomical location of a tumor using MRI or PET-CT imaging. Subsequently, clinicians can utilize optical imaging approaches to delineate the exact cellular margins of disease guiding surgical intervention and accurate resection of the tumor.[33,35,36] Clinically, multimodal imaging platforms are already proving capable of significantly improving disease diagnosis,[37-39] treatment development[40-42] and therapeutic evaluation[43-47] in patients compared to single modality imaging approaches.[48]

While optical imaging remains a pre-clinical tool for in vitro and ex vivo applications, it is gaining more widespread attention for clinical translation.[29,49-51] This is due to a unique set of characteristics that distinguish it from all other imaging modalities. Optical imaging is inherently safe due to its reliance on non-ionizing radiation which can be applied (within limits of exposure time, excitation power density and wavelength)[52,53] for prolonged periods of time without damaging tissue.[54] Optical imaging is also exceptionally sensitive and highly specific when compared to other modalities.[55] Currently, optical techniques are able to detect signals from contrast agents present at concentrations below 10^{-15} moles/L millimeters in tissue, enabling excellent signal-to-noise capabilities.[6] Optical imaging generally employs relatively low-cost, easy-to-use and portable instruments,[6] which are amenable to ready adoption by clinicians and technicians. Fiber endoscopy and fluorescence endoscopy are just a few examples of the

growing advances in miniaturized clinical imaging.[56,57] Approaches such as these open the possibilities for real-time, high throughput molecular imaging, which combined with anatomical imaging techniques, can provide valuable insight into pathological states.

1.3. Optical Imaging

There are two broad types of optical imaging approaches: planar and tomographic imaging. Planar imaging generally involves irradiating a specimen (cell, tissue or organism) with light tuned to a particular wavelength or excitation. The particular wavelength depends on the fluorophore or contrast agent of interest and can be either endogenous (e.g. tissue components) or exogenous (e.g. organic dyes). Depending on whether the emitted light is collected on the same side as the excitation or through the specimen, planar imaging can be either reflectance- or transillumination-based, respectively. Planar imaging is the simplest, fastest and most frequently used optical imaging technique.[51] Fluorescence-based optical imaging, also known as fluorescence reflectance imaging (FRI), and bioluminescence imaging (BLI) are examples of planar optical imaging.

Tomographic imaging, which is considerably slower than planar imaging but can have up to an order of magnitude better penetration depth (~10 cm compared to ~1 cm),[4] relies on transilluminated light that has been absorbed and scattered from multiple projections. Using tomographic imaging in combination with fluorescent reporters, or fluorescence mediated molecular tomography (FMT), opens the possibility for using this technique to identify molecular features deeper than possible with planar imaging.[58,51]

In all cases, however, the fundamental principles behind optical imaging lie in the way light interacts with tissue (**Fig. 1.1**). Light can be absorbed, scattered, refracted or reflected during its propagation through bulk tissue samples. Most significantly, optical attenuation arises from signal losses which occur through absorption and scattering.

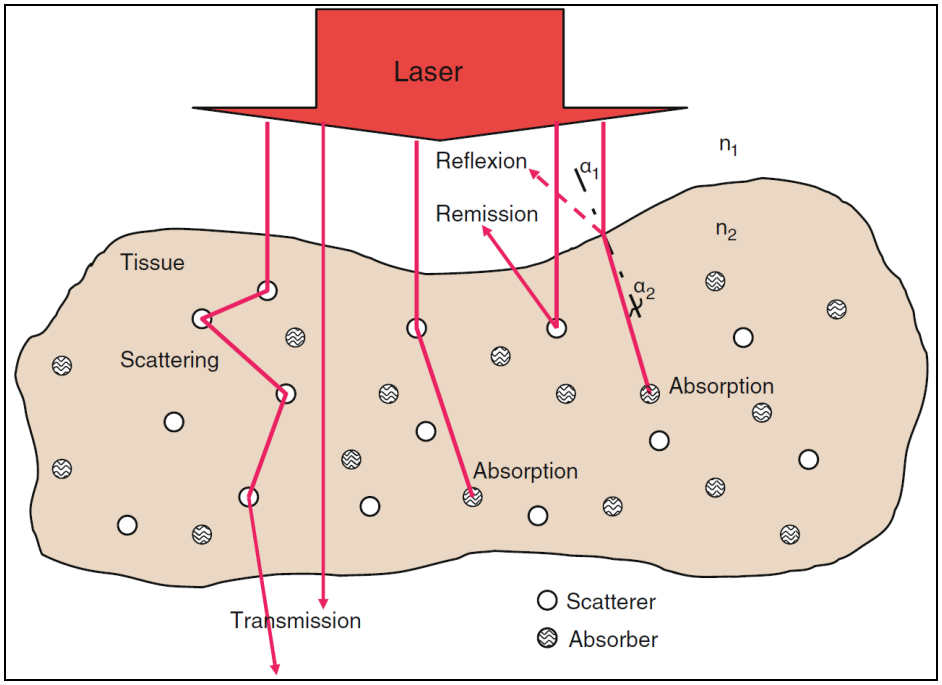

Figure 1.1 – Light-Tissue Interactions. The interaction of light with tissue can lead to various optical events, such as scattering, absorption or reflection (here reflexion). This figure was reproduced from Chapter 2 (by Rudolf Steiner) of: Anderson, R.R. & Ross, E.V. Laser-tissue interactions. *Cutaneous Laser Surgery. Mosby: Philadelphia, PA* **9**(1994).[53]

1.3.1. Principles Governing Light-Tissue Interactions - Absorption

Light incident on biological tissues interacts with various intracellular and extracellular components and is absorbed, generally resulting in heat dissipation within the absorbing medium. The result of absorption is a reduction in the intensity of light that propagates though a medium. The biological components that absorb light, called tissue

chromophores, exhibit unique absorption spectra (**Fig. 1.2**). In heterogeneous tissue, the total attenuation of light through absorption is caused by the sum of each chromophore's unique absorption values, or extinction coefficients, highly dependent on concentration.[50]

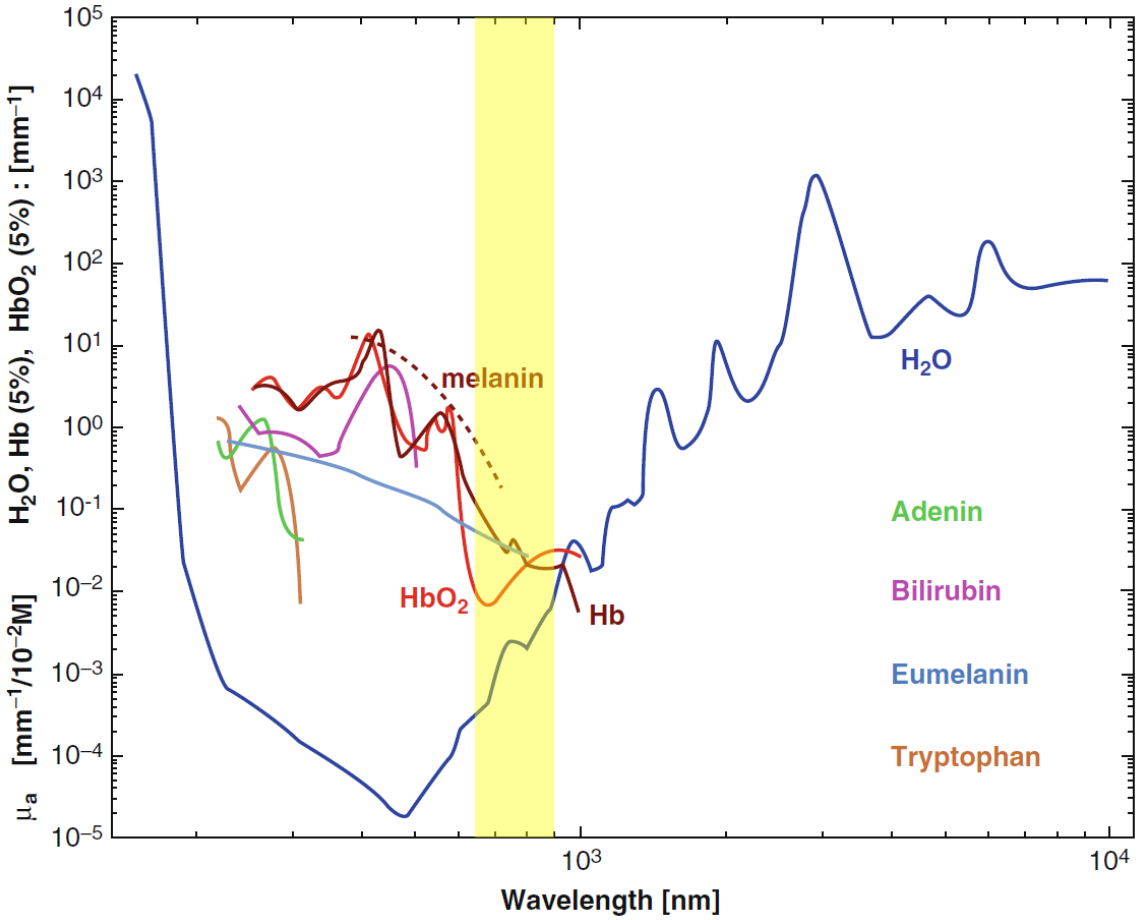

Figure 1.2 – Absorption Spectra of Common Biological Chromophores. The absorption spectra of various tissues has been important for optical probe design. The relatively low absorption of various biological components in the NIR (highlighted in yellow) has led to interest in this wavelength region for optical imaging. This figure was

reproduced from Chapter 2 (by Rudolf Steiner) of: Anderson, R.R. & Ross, E.V. Laser-tissue interactions. *Cutaneous Laser Surgery. Mosby: Philadelphia, PA* **9**(1994).[53]

Water, hemoglobin, lipids and melanin are some of the strongest absorbers in biological tissues.[50,59] Proteins and nucleotides found in DNA and RNA also act as strong absorbers, particularly of ultraviolet (UV) light. The aliphatic amino acids, such as glycine, alanine and leucine, absorb at wavelengths before 240 nm while aromatic amino acids such as phenylalanine, tyrosine and tryptophan absorb above 240 nm.[60] The purine and pyrimidine bases in DNA and RNA absorb UV light between 230-300 nm.[23] Broadly speaking, proteins and nucleotides primarily absorb UV light, hemoglobin and melanin absorb visible light and water acts as a strong infrared absorber.

Water, the most abundant chemical in the body, does not have any significant absorption bands in the UV or visible region. Water begins to absorb light above 900 nm in the infrared.[23] In practice, however, water is considered to be weakly absorbing above 1,300 nm, with more pronounced peaks above 2,900 nm.[61]

Hemoglobin is a metalloprotein found in red blood cells which carries oxygen around the bloodstream. Hemoglobin has unique absorbance spectra based on whether it is in an oxygenated (HbO_2) or de-oxygenated (Hb) state. The profiles for the two states are significantly different, particularly in the red region of the visible and the near-infrared (NIR).[62] Together with water, these two compounds represent the major absorbers of visible and infrared light. Within their spectra is a region in the near infrared, between 650-900 nm, with relatively low absorption.[49] Light in this range is

much more effective at propagating through tissues, opening a "window" for biomedical optical imaging.[31]

Lipids and melanin can exhibit strong absorption in the NIR, significantly contributing to attenuation. Lipids have a sharp absorption band around 930 nm but otherwise share a very similar absorption spectrum to water.[63] Melanin, a pigment found in the epidermal layer of skin, significantly absorbs both visible and NIR light.[64] It exhibits broad absorption in the visible region but decreases in magnitude with increasing wavelength. The importance of these two chromophores, however, is greatly dependent on the tissue being imaged. The lipid and melanin content varies drastically from tissue to tissue and often the attenuation effects due to water and hemoglobin content dominate as the major absorbing components.

In all instances, the absorption of light by chromophores can result in tissue-induced fluorescence emission (**Fig. 1.3**). Tissue "autofluorescence" can severely limit the signal-to-background ratio and is a particularly significant problem when using visible light for in vivo imaging.[50] The amount of autofluorescence determines the sensitivity that can be achieved for detecting a contrast agent of interest. Chromophores such as elastin, collagen, tryptophan and porphyrins can significantly contribute to tissue autofluorescence and generally have absorption bands in the visible and UV regions of the spectrum.[65] It has also been shown that the chlorophyll found in alfalfa in standard mouse chow contributes significantly toward NIR autofluorescence.[66]

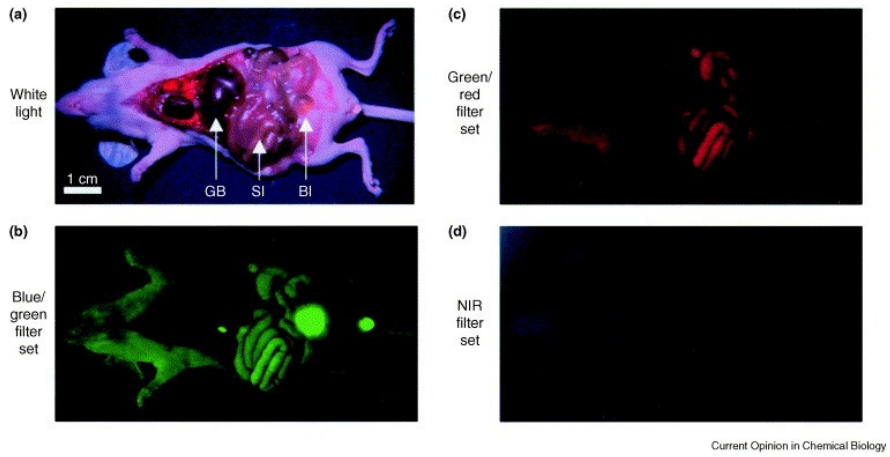

Figure 1.3 – Tissue Autofluorescence. Wavelength-dependent tissue autofluorescence can be see when the mouse (a) is irradiated with various excitation/emission filter sets: (b) blue/green and (c) green/red. The NIR filter set, on the other hand, shows significantly less tissue autofluorescence. This figure was reproduced from: Frangioni, J.V. In vivo near-infrared fluorescence imaging. *Curr Opin Chem Biol* **7**, 626-634 (2003).[67]

1.3.2. Principles Governing Light-Tissue Interactions - Scattering

Light scattering is a significant cause of signal attenuation in tissues and dominates over absorption in certain regions of the spectrum.[48] As light propagates through heterogeneous tissues, cellular components such as nuclei, cellular membranes, lipids, mitochondria and water all contribute to multiple scattering events.[68,69] Scattering leads to the spreading, or defocusing, of optical signal. This both changes the original directionality of propagating light and obscures the information carried by light. There

are two main types of light scattering that can occur in tissue: inelastic and elastic scattering.[23]

Inelastic scattering results in a change of frequency and wavelength between the incident and scattering photons. Raman scattering is a type of inelastic scattering that produces excitation of molecular vibrations and can be useful for determining chemical and structural changes in disease tissues. The magnitude of Raman scattering, however, is inherently weak and occurs at the rate of approximately 1 inelastically scattered photon for every 10^7 elastically scattered photons.[70] Surface enhanced Raman scattering (SERS) further increases the gain of Raman intensity and improves the detection limits using specific molecules adsorbed onto noble metal nanoparticles.[71]

Elastic scattering, on the other hand, results in both the incident and scattered photons having the same frequency and wavelength. While there are two primary forms of elastic scattering, Rayleigh and Mie, neither appears to accurately describe the scattering that occurs in tissue.[20] Rayleigh scattering occurs from particles of a smaller size compared to the wavelength of the incident light. In tissue, these particles can be certain subcellular components, such as cellular membranes or organelles. For scattering centers which are ~10 times smaller than the incident wavelength (**Fig. 1.4**), Rayleigh scattering is governed by λ^{-4}.[72] This strong dependence on the wavelength of light results in greater amounts of Rayleigh scattering occurring with bluer light, compared to red and infrared light. In addition to particle size and wavelength, Rayleigh scattering is highly dependent on the refractive index mismatch between the scattering particle and the surrounding medium.[23]

Mie scattering occurs in instances where the wavelength of the incident light is comparable to the size of the scattering center in tissues (**Fig. 1.4**). Much like Rayleigh scattering, refractive indices mismatches between a scattering particle and the surrounding medium strongly influence Mie scattering.[48] However, unlike Rayleigh scattering, it is governed by much weaker wavelength dependence, by λ^{-x}, where x is generally between 0.4 and 0.6 for specific tissues.[72,23] Scattering occurs primarily in the forward direction for Mie scattering, while the amount of forward and backward Rayleigh scattered light is approximately equal.[73]

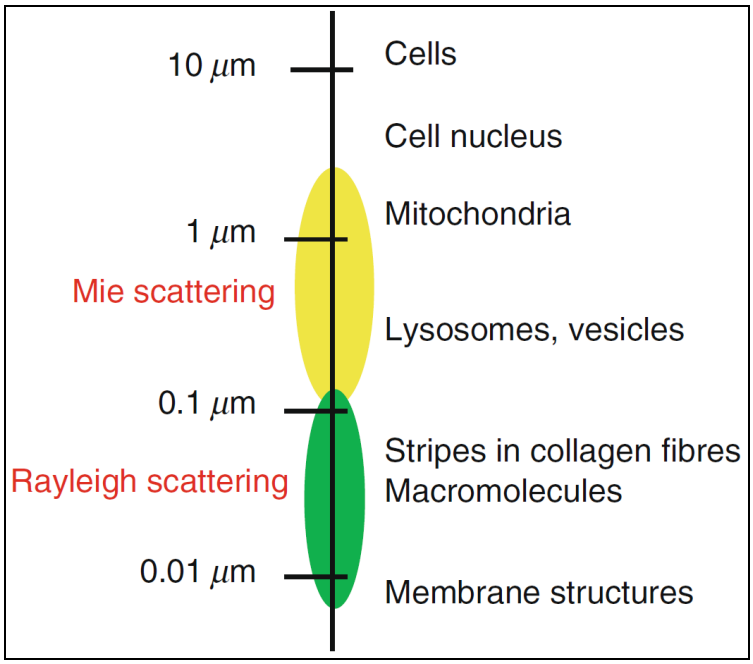

Figure 1.4 – Elastic Scattering. Light scattering from tissues can undergo either Mei or Rayleigh scattering depending on the size of the scattering center. This figure was reproduced from Chapter 2 (by Rudolf Steiner) of: Anderson, R.R. & Ross, E.V. Laser tissue interactions. *Cutaneous Laser Surgery. Mosby: Philadelphia, PA* **9**(1994).[53]

1.4. Contrast Agents for Optical Imaging

The translation of molecular imaging requires the specific targeting of key cellular features in order to ascertain relevant information. Resolving at the molecular scale requires approaches that can target and enhance the contrast of specific molecular features resulting in high signal-to-noise ratios (S/N) over non-targeted structures. For all imaging modalities, but particularly those such as optical imaging which aim to resolve molecular features, contrast enhancement can be achieved by using either endogenous or exogenous contrast agents.[74]

1.4.1. Endogenous Contrast Agents

For optical imaging, contrast using endogenous detection methods generally relies on measuring the differences between various light-tissue interactions. Although this method removes the need for introducing exogenous agents and the challenges that arise from regulatory approval,[12] endogenous contrast generally does not provide useful imaging due to low sensitivity or specificity.[11,74]

1.4.2. Exogenous Contrast Agents

Exogenous contrast agents have become important as probes which can be used for detection by imaging modalities. Various classes of exogenous contrast agents exist, such as small organic molecule fluorophore, antibody, peptide and nanoparticle reporters.[74] In order to extract detailed information from imaging, these contrast probes must be engineered to achieve quantitative, sensitive and specific high-resolution imaging of multiple molecular events in situ.

Small organic fluorophores, such as NIR-emitting FDA-approved indocyanine green (ICG or Cardio-Green), have been commonly used as reporters for in vitro and pre-clinical optical imaging.[75] Yet these reporters suffer from a number of drawbacks that limit translation for molecular imaging. In addition to suffering from low photostability which leads to photobleaching, the optical tunability of organic fluorophores is difficult to control.[50] Furthermore, organic fluorophores, antibodies and peptides can be rapidly cleared from circulation due to their small size, resulting in poor biodistribution and pharmacokinetics.[11,76]

Nanoparticles are submicron-sized colloidal systems that are composed of one or more inorganic and/or organic materials which can include polymers, lipids, viruses, metals and organometallic compounds.[77-81] Nanoparticles possess unique physical and dimensional properties that offer numerous advantages for engineering effective imaging agents.[82]

Nanoparticles can be used to sequester large amounts of diverse cargos, such as fluorophores or therapeutics, into discrete, self-contained structures. By loading nanoparticles with large amounts of contrast agents, for example, and controlling their in vivo biodistribution, contrast agent accumulation can be greatly enhanced at targeted sites resulting in signal amplification.[83] Formulating contrast agents or drugs into nanoparticles can also improve cargo stability, enhance efficacy and protect non-targeted tissues from the delivered payload. In addition, one of the greatest impediments toward clinical application of molecular imaging is poor pharmacokinetics of new imaging agents.[7] The physical and chemical tunability of nanoparticles can lead to prolonged circulation and reduced clearance, which result in improved cargo pharmacokinetics and

lead to a greater likelihood of disease targeting.[11] Furthermore, controlling the physical and chemical properties of nanoparticles such as size, surface charge and targeting ligand presentation can drastically influence their in vivo biodistribution. Finally, the presentation of ligands targeting specific for cellular receptors can improve the specificity of nanoparticle targeting and lead to "multivalent" effects.

1.5. Nanoparticle Design Considerations

Nanoparticle design exerts significant influence on the behavior of nanoparticles in a biological environment.[83,84] Various properties including size, charge and surface modification must be taken into careful consideration when engineering nanoparticles for a specific application. Shape has also been shown to effect nanoparticle interactions with cells, however the mechanisms behind the differences are not yet fully understood.[85-87]

1.5.1. Nanoparticle Size

Size is an important physical property that has been shown to greatly affect nanoparticle behavior for in vivo cancer targeting. The lower boundary of nanoparticle size is generally considered to be around 10 nm in diameter, the estimated threshold for first-pass elimination by the kidneys. The upper boundary, however, is less defined and not entirely clear. Many tumor vessels tend to exhibit irregular branching patterns and abnormal architecture, a consequence of poorly-aligned endothelial cells with wide fenestrations and loose focal intercellular openings. These unique properties of the tumor microenvironment lead to a "leaky" endothelium, enabling larger macromolecules, such as nanoparticles, to accumulate in tumor tissue much more than in normal, healthy tissue (**Fig. 1.5**).[88] Experiments have shown that the threshold for this so-called Enhanced Permeability and Retention Effect (EPR) in liposomes is approximately 400 nm and that sizes of carriers below 150 nm are more effective at accumulating in the tumor tissue.[89-92] Evidence has confirmed that this phenomenon occurs in humans as well as in animal models. Nanoparticle delivery which relies on the EPR effect is commonly referred to as

"passive targeting" and can result in the selective extravasation of certain type of particles into solid tumors.

1.5.2. Nanoparticle Charge

In addition to size, surface properties play a critical role in determining the fate and biological interactions of nanoparticles. In vivo experiments have shown that slightly negative, slightly positive or neutral nanoparticles can penetrate and be effectively transported through tissue.[84,93,94] Nanoparticles can be further tailored with amphiphilic coatings, such as polyethylene glycol (PEG) polymers, which further aid to both promote biocompatibility and limit nonspecific interactions with biomolecules.[95] Amphiphilic coatings can also be used to reduce the self-aggregation tendency of nanoparticles in aqueous solutions by creating a hydrated layer around each nanoparticle, separating them in suspension.[95] Greater surface charges, whether positive or negative, increase the likelihood for nanoparticle opsonization, a process by which certain serum proteins adsorb onto the surface of nanoparticles and interact with monocytes or certain tissue macrophages. Opsonization leads to macrophage scavenging and greater clearance of nanoparticles by the reticuloendothelial system (RES), which consists of phagocytic cells in the liver, spleen and lymph nodes.[84] While nanoparticle clearance is fundamentally important, minimizing rapid losses is crucial to realizing the utility of nanoparticles in vivo.

1.5.3. Nanoparticle Active Targeting

Although charge and steric stabilization provide improvements in systemic nanoparticle pharmacokinetics, non-uniform and untargeted biodistribution are limiting factors that prevent nanoparticles from effectively accumulating at diseased tissues.[96] This has led to the development of targeting ligands, which can be anchored to the surface of nanoparticles usually through covalent interactions. The result is commonly referred to as a "functionalized" or "targeted" nanoparticle system. In contrast to passive delivery, targeting nanoparticles to specific molecular receptors using ligands is known as "active delivery" (**Fig. 1.5**). The targeting ligands themselves can be chemical or biological moieties including compounds such as small molecules,[97] peptides,[98] or antibodies.[99] Such ligands improve or direct specific nanoparticle-cell interactions, enabling enhanced and modified accumulation at diseased tissue. Selecting the appropriate ligand is dependent on the properties of the targeted receptor and optimal targets should be readily accessible (cell surface), expressed either highly or only within the desired target tissue, not shed from cell surface and broadly expressed across several disease states.[100] Ideally, the ligand should have high target binding affinity, in the low to sub-nanomolar range,[101] and the ligand-receptor interaction should exhibit a large dissociation constant (K_d) to promote stable binding.[102,103]

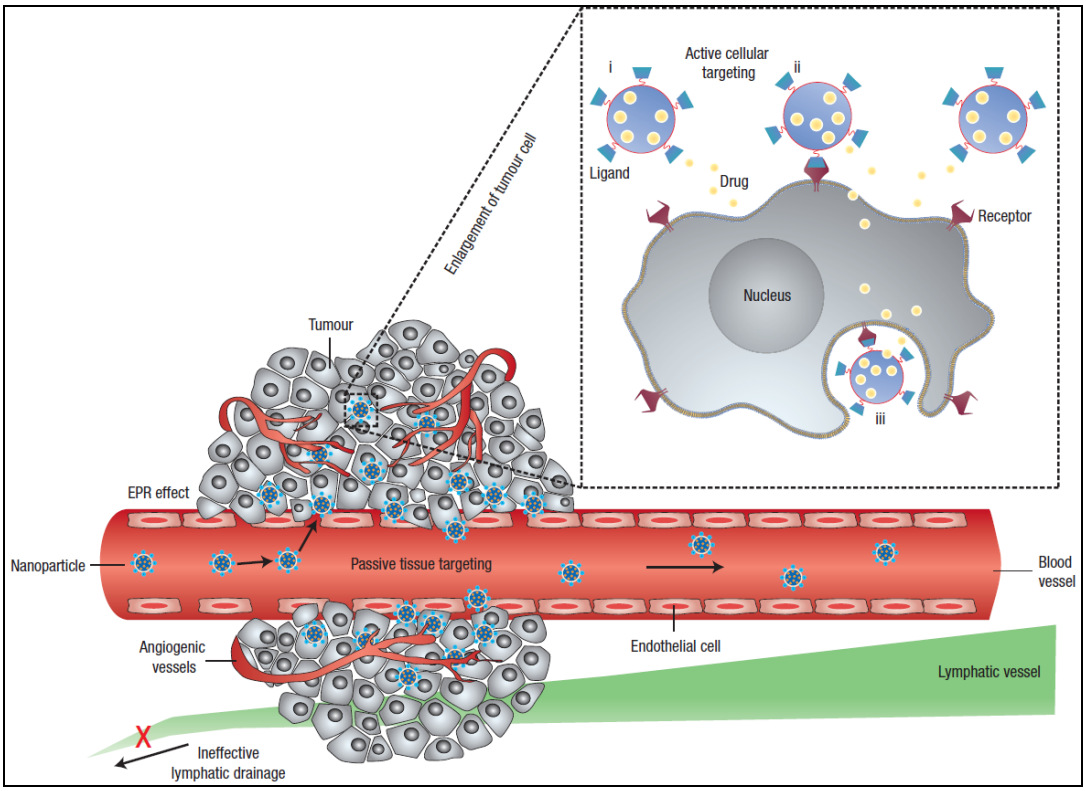

Figure 1.5 – Tumor Targeting Using Nanoparticles. Schematic representing the different mechanisms of nanoparticle uptake in tumors. This figure was reproduced from: Peer, D., *et al.* Nanocarriers as an emerging platform for cancer therapy. *Nat. Nanotechnol.* **2**, 751-760 (2007).[104]

Generally, a single targeting agent molecule attached to a nanoparticle will not generate enough binding force to anchor or target a specific biological site.[105] However, it has been shown that the simultaneous binding of multiple ligands to specific receptors promotes greater targeting efficacy and results in "multivalent" interactions.[102,103] The greater avidity which results from multivalency is generally due to a reduction in the off-rate (k_d) or ligand-receptor dissociation while the on-rate (k_a) or ligand-receptor binding

remains relatively unchanged.[102,105,106] Based on their high surface-to-volume ratio, nanoparticles can be used to display numerous targeting ligands on their surface to facilitate multivalent binding. Improvements in cell avidity through multivalency using ligand functionalized nanoparticles have been reported to exist in several ligand-receptor interactions, including receptors targeted by folic acid,[102] cyclic arginine-glycine-aspartic acid (cRGD),[98] glucose and mannose.[107] Multivalent interactions can also open the possibility for using high densities of ligands with individually low receptor affinities.

There are several important considerations that must be addressed when proceeding with an active targeting strategy for nanoparticles. Although multivalent targeting is desired, arbitrarily functionalizing nanoparticles with a large number of ligands may not necessarily lead to a greater degree of disease targeting. In addition to the physical changes that may occur with high density functionalization, such as increased aggregation and lowered stability both resulting from changing the surface properties of nanoparticles, the interactions of particles in a biological setting may also change. Furthermore, the effectiveness of multivalency is largely dependent on the context in which it is used, whether at a two-dimensional cellular-level or three-dimensional organism-level.[108,109]

In vitro studies have shown that there may exist an optimum ligand density for particle binding avidity beyond which only modest gains in avidity occur.[102] Furthermore, targeted disease sites present a finite number of receptors which can interact with ligand functionalized nanoparticles. As the amount of targeted particles binding to these receptors increases, so does the degree of receptor and binding saturation. Targeted

nanoparticles which are unable to bind to receptors at the site of interest will now exhibit a pharmacokinetic profile similar to that of untargeted particles.[105,110]

A potential solution to this problem in vivo could be to utilize only low densities of high affinity ligands, yet this solution could result in what is known as a "binding site barrier."[111] It has been reported that nanoparticles displaying high affinity ligands exhibit decreased penetration into a solid tumor compared to ones functionalized with ligands of less affinity toward the targeted receptor.[112] Other potential solutions to receptor saturation have been reported, including strategies that introduce more targetable sites in tumors using the in vivo assembly of nanoparticles,[113] amplify targeting by using "signaling" and "receiving" nanoparticles that induce new binding sites in tumors,[114,115] and improve tumor penetration using tissue penetrating peptides linked to tumor targeting motifs.[116]

A final consideration for conjugating a ligand onto a nanoparticle is the nature of the conjugation linker used. The length of the linker may influence targeting by either facilitating multivalent interactions[117] and/or reducing steric hindrance between ligand moieties.[118] Furthermore, the chemical structure of certain crosslinking agents, such as sulfosuccinimidyl 6-(3′-[2-pyridyldithio]-propionamido) hexanoate (SPDP) or sulfosuccinimidyl 6-[α-methyl-α-(2-pyridyldithio)toluamido] hexanoate (SMPT), contain labile disulfide linkages which are susceptible to degradation under certain conditions.[119] In contrast, nonlabile maleimide crosslinkers appear to be more stable for certain nanoparticle-based delivery applications.[119] While numerous other conjugation chemistries and linkers can be utilized,[120] the availability of specific nanoparticle functional groups will ultimately determine the approach to be used.

1.6. Rare Earth Nanoparticles as Optical Imaging Contrast Agents

As mentioned previously, nanoparticles can be composed of a wide range of organic or inorganic materials. For many instances, fluorescence dyes can be sequestered into liposomes,[121] dendrimers,[122] micelles[123] and many other nanoparticle systems. However, certain nanostructures such as gold nanoparticles,[124] single-walled carbon nanotubes,[125,126] quantum dots[127] and rare earth-doped nanoparticles[128] have all been shown to have inherent contrast capabilities for optical imaging.

Rare earth-doped nanoparticles (REs) are the primary contrast agents of focus for this dissertation. REs are ceramic nanoparticles which contain rare earth ions. REs can be excited with NIR and upconvert the energy for visible emissions (**Fig. 1.6**).[129] In addition, REs are also able to generate infrared (IR) emissions after NIR excitation through traditional downconversion fluorescence mechanisms.[130]

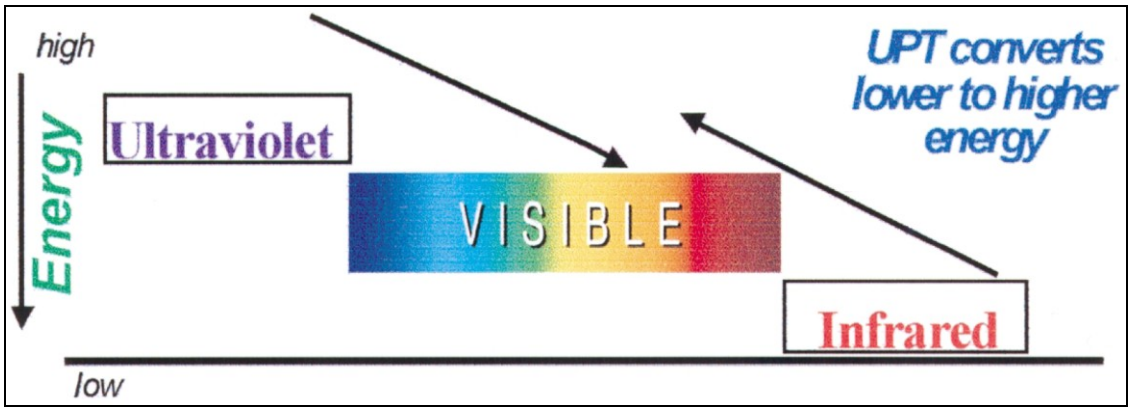

Figure 1.6 – Upconversion Fluorescence. Principle of upconversion fluorescence (here UPT). This figure was reproduced from: van de Rijke, F., *et al.* Up-converting phosphor reporters for nucleic acid microarrays. *Nat. Biotechnol.* **19**, 273-276 (2001).[129]

1.6.1. Fabrication of Rare Earth Doped Nanoparticles

There are two primary methods for synthesizing REs: thermal decomposition[131,132] and hydrothermal synthesis.[133,134] Thermal decomposition involves dissolving organic trifluoroacetate precursors in solvents using surfactants such as oleic acid or oleylamine under high temperatures (250–350°C).[135] This process of RE formation occurs over four distinct and consecutive stages: nucleation in a delayed time, size growth by monomer supply, size shrinkage by dissolution, and aggregation.[136] The method yields high quality nanoparticles that exhibit monodisperse populations of small sizes and high crystallinity. By varying such parameters as reaction time, concentration of reagents and reaction temperature, various sizes and shapes of REs can also be obtained.[136]

Hydrothermal or hydro(solvo)thermal synthesis likewise generates controllable nanoparticle sizes and shapes, including prisms, rods, spheres, and flower patterned disks, by varying reaction parameters such as fluoride source, organic additives and pH.[137,138] Synthesis can occur at significantly lower temperatures than thermal decomposition (160–220 °C). It is a solution-based synthesis approach, utilizing solvents under pressures and temperatures above their critical point to increase the solubility and reaction kinetics of RE precursors.[139]

1.6.2. Design Considerations for Rare Earth Doped Nanoparticles

For $NaYF_4$ co-doped REs, upconversion fluorescence occurs following the non-radiative transfer of excitation energy from a sensitizer, generally Yb, to an activator such as Er or Tm, resulting in the emission of photons.[140] For this transfer to occur, however, the excited energy levels of both the sensitizer and activator must be nearly equal (or

resonant) and the two ions must be in close proximity with one another to permit the transfer of energy. Trivalent Yb is well resonant with several typical upconverting lanthanide ions, such as Er, Tm, Ho, Pr, Gd, Nd, and Dy,[141] acting as a very efficient sensitizer for energy transfer.[142]

The selection of the host material is also important to ensure high upconversion efficiency. Ideal host materials should exhibit low lattice phonon energies which will minimize the non-radiative transfers that occur during upconversion while maximizing radiative emissions. Fluorides, such as $NaYF_4$, have been shown to display low phonon energies, high chemical stability and high optical transparency ideal for upconversion processes.[142] In addition, the crystalline structure of the host can influence the efficiency of upconversion. For example, hexagonal phase $NaYF_4$ hosts have been shown to exhibit significantly greater upconversion efficiencies compared to cubic phase $NaYF_4$ hosts.[135] This may be due to the low symmetry of hexagonal phase $NaYF_4$ hosts, resulting in uneven components of crystal-fields which enhance the probability of sensitizer to activator energy transfer.[143]

Finally, when synthesizing upconverting nanoparticles, generally a core-shell scheme is adopted. The nanoparticle core contains the host material and dopants, for example $NaYF_4$:Yb,Er, while a thin shell composed of the inert host material surrounds the inner doped structure. In addition to protecting the dopants from degradation, the shell acts to both minimize surface quenching effects and improve upconversion efficiency.[144]

1.6.3. Mechanisms of Fluorescence

While numerous studies involving REs focus on imaging with upconversion fluorescence,[140,142] REs are also able to emit through traditional fluorescence mechanisms in the short wavelength infrared (SWIR) region (1000-1700 nm) after NIR excitation.[130]

Upconversion fluorescence occurs during the excitation of trivalent rare earth ions by the sequential absorption of two or more NIR photons, which results in the nanoparticles reaching a higher excited energy level.[145] Unlike two-photon excitation which occurs after the simultaneous absorption of photons, upconversion fluorescence does not require high powered pulsed lasers relying instead on inexpensive continuous wave laser diodes.[135] Furthermore, upconversion fluorescence is much more efficient than two-photon absorption.[146] The upconversion fluorescence process can occur through three main mechanisms: excited state absorption (ESA), photon avalanche and energy transfer upconversion (ETU). Of these three, co-doped $NaYF_4$ nanoparticles rely primarily on ETU for upconversion (**Fig. 1.7**),[142] and the ETU mechanism is considered to be the most efficient upconversion process known.[140]

REs can also emit SWIR after NIR excitation through traditional fluorescence mechanisms (**Fig. 1.7**).[147-149] Examples of SWIR emissions can be seen with Nd:YAG (Nd-doped yttrium aluminum garnet),[150] a solid state laser material that emits at 1064 nm after 800 nm excitation, and Er-doped silicate glass fibers,[151] which are commonly used in the telecommunications industry and emit at 1550 nm after 980 nm excitation.[130]

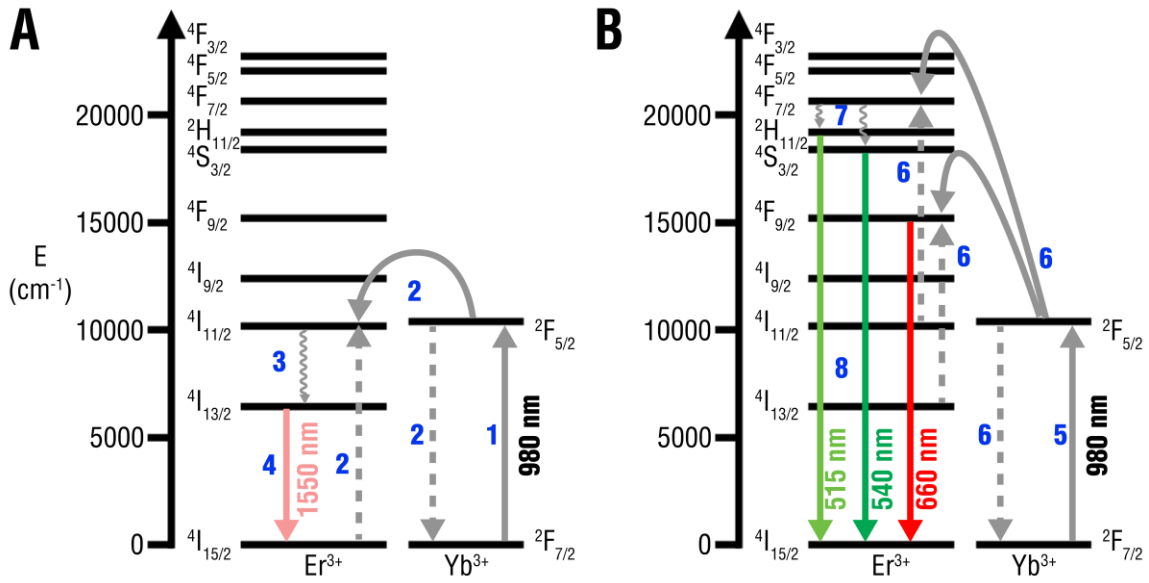

Figure 1.7 – Energy Diagram for NaYF4 Yb:Er nanoparticles. Energy diagram for downconversion fluorescence (A) and upconversion fluorescence (B) of $NaYF_4$ Yb:Er nanoparticles after 980 nm NIR excitation. After Yb^{3+} is excited to the $^2F_{5/2}$ state (1), it can act as a sensitizer and transfer energy to the unexcited Er^{3+} (2) bringing it from $^4I_{15/2}$ to the $^4I_{11/2}$ excited state. Er^{3+} can relax to $^4I_{13/2}$ (3) and emit at 1550 nm (downconversion) from the $^4I_{13/2} \rightarrow {}^4I_{15/2}$ transition (4). In addition, Yb^{3+} can be further excited (5) and transfer more energy to Er^{3+} before relaxation occurs (6). This can bring Er^{3+} to the $^4F_{7/2}$ and $^4F_{9/2}$ excited states (6), which can relax to the $^2H_{11/2}$ or $^4S_{3/2}$ state (7) and emit at 515 nm, 540 nm and 660 nm. This figure was adapted from: Manseau, M.P. Lanthanides-based upconverting biolabels in the near-infrared. *Department of Chemistry, University of Victoria* (2009).[152]

1.7. Albumin Nanoparticles as Delivery Agents

Recently, non-targeted nanoparticles composed of human serum albumin carrying paclitaxel (Abraxane ®, Abraxis BioScience Inc.) have been approved by the FDA for clinical use in the treatment of metastatic breast cancer. Abraxane was the first commercially available nanoparticle formulation containing a drug for the treatment of a disease in human history.[153] In phase III trials, the formulation increased both the bioavailability and circulation half-life of paclitaxel while reducing its toxicity in vivo.[154]

Taxanes, such as paclitaxel, are an important class of antitumor agents that rely on solvent-based delivery vehicles. These compounds act to stabilize microtubules causing mitotic arrest and have broad activity in a range of solid tumors.[155-158] Unfortunately, the clinical effectiveness of taxanes has been limited by delivery strategies that relied heavily on solvents such as polyethoxylated castor oil (Cremophor® EL or CrEL), which has been linked to a number of serious side effects such as neutropenia, peripheral neutropathy and axonal degeneration.[159,160] In addition to toxicity, CrEL may attenuate the effects of paclitaxel by forming micelles around the drug resulting in decreased delivery of the compound into tumor cells.[161,162]

In an effort to both reduce the toxicity of previous paclitaxel formulations while increasing its bioavailability, Abraxis Biosciences developed *nab*-paclitaxel (Abraxane ®), or nanoparticle albumin-bound paclitaxel. *Nab*-paclitaxel is prepared by high-pressure homogenization of paclitaxel in the presence of human serum albumin resulting in a nanoparticle colloidal suspension having an average size of approximately 130 to 150 nm.[163]

Nab-paclitaxel is not only the first FDA approved drug that uses albumin nanoparticles for human therapy, it is also the first FDA approved nanoparticle-based drug delivery system. FDA approval, as well as the inherent physical and chemical properties of monomeric albumin, has sparked growing interest in utilizing protein nanoparticles for a broad spectrum of biological applications.

1.7.1. Albumin Exhibits Highly-Desirable Properties as a Delivery Agent

Albumin is an acidic, soluble protein with a molecular weight of 66.5 kDa (**Fig. 1.8**). It is the most abundant plasma protein (35-50 g/L human serum), having a half-life of approximately 19 days after being synthesized in the liver. Albumin has a number of functions in vivo it: 1) maintains the colloidal osmotic pressure and buffers pH in the circulatory system; 2) solubilizes and transports fatty acids (FA) to the liver; 3) binds metal ions such as copper (II), nickel (II), calcium (II) and zinc (II), enabling transport through blood; 4) binds to bilirubin, a degradation product of heme; 4) binds to numerous therapeutic drugs such as penicillin, sulfonamides and benzodiazepines and; 5) after degradation, provides amino acids to peripheral tissues.[164] Albumin's ability to bind readily with a number of therapeutic drugs, coupled with its biodegradability, lack of toxicity or immunogenicity and preferential uptake into tumor tissues, has made it an ideal candidate for both drug and contrast agent delivery purposes.

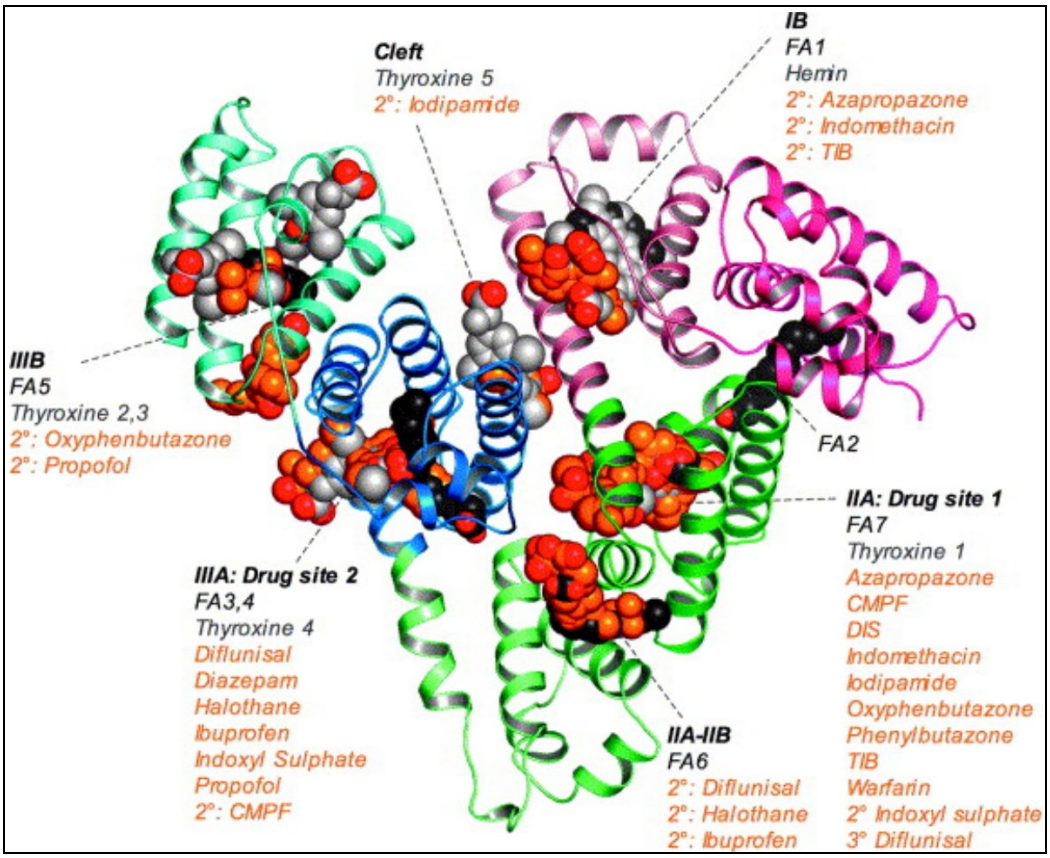

Figure 1.8 – Structure and Drug Binding Sites of Human Serum Albumin. Albumin possesses two main drug-binding sites, however there are numerous reports of secondary binding sites on the protein. (FA – fatty acid). Energy diagram for upconversion fluorescence using $NaYF_4$ Yb:Er nanoparticles. This figure was reproduced from: Ghuman, J., *et al.* Structural basis of the drug-binding specificity of human serum albumin. *J. Mol. Biol.* **353**, 38-52 (2005).[165]

1.7.2. Pharmacological Profile of Abraxane ®

During circulation, *nab*-paclitaxel is taken up by tumors through the endothelial wall which is mediated by both a leaky vascular (EPR effect) and through albondin

(gp60), an albumin receptor. Preclinical work has indicated that the albondin receptors transport albumin-bound drugs in a manner similar to free albumin.[166,167] The binding of albumin to gp60 results in the glycoprotein receptor interacting with the intracellular caveolin-1 protein, triggering cell membrane invagination and forming transcytotic vesicles known as caveolae.[168]

Additionally, preliminary evidence suggested that another albumin-binding protein, secreted protein acidic and rich in cysteine (SPARC or also osteonectin), which is produced in high concentrations by tumors into the tumor interstitium and onto the tumor surface, increases the effectiveness of *nab*-paclitaxel.[169] Elevated expression of SPARC has been correlated with increased tumor invasiveness and metastasis, which can lead to poor prognosis in a number of tumors such as melanoma, breast, prostate, colorectal, liver, lung, kidney, bladder, thyroid and brain cancers.[170]

These results indicate that *nab*-paclitaxel may utilize both gp60 and caveolae-mediated albumin transport pathways to pass through blood vessel endothelial lining and into the tumor (**Fig. 1.9**). Once there, SPARC acts to retain the nanoparticles within the tumor. The result is that the *nab*-paclitaxel has been shown to exhibit preferential uptake by tumors compared to free paclitaxel leading to decreased side effects and better patient response rates.[171]

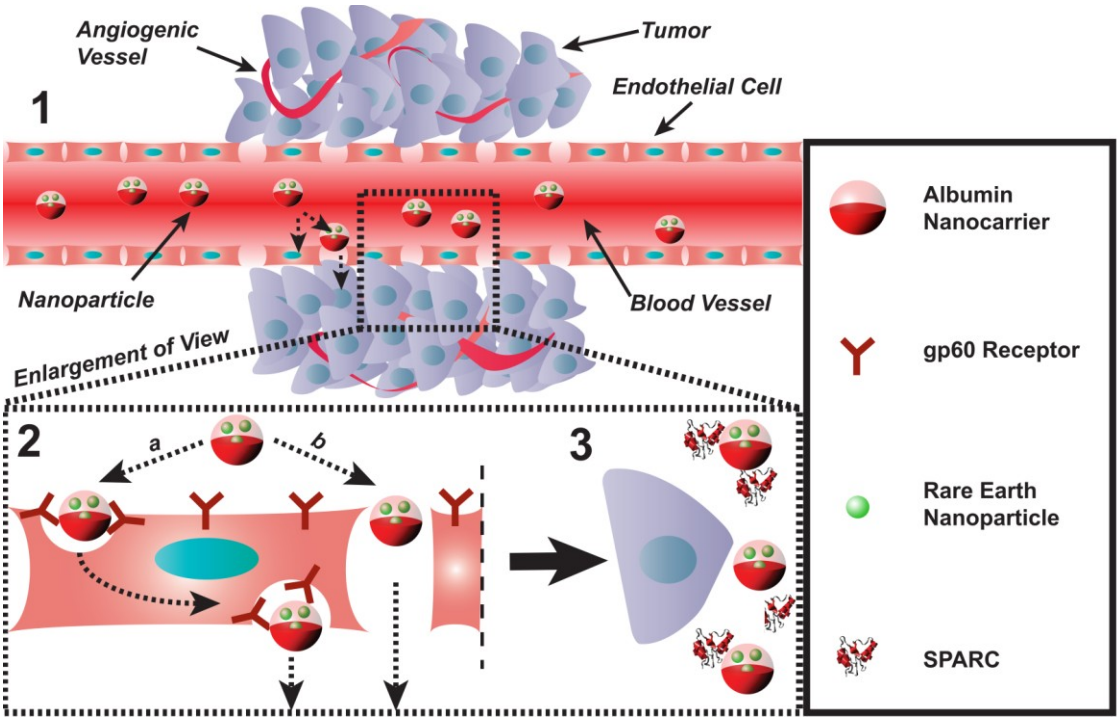

Figure 1.9 – Proposed In vivo Mechanism of Albumin Nanocarrier Accumulation in Tumors. Step 1: Albumin nanocarriers will circulate through the bloodstream and eventually arrive near the site of the tumor. Step 2: Albumin nanocarriers will have the opportunity to enter into the tumor interstitium by either a) binding to the gp60 (albondin) and undergoing transcytosis through endothelial cells by caveolae or b) passing through the leaky vasculature and spacing between endothelial cells near the tumor (EPR effect or passive targeting). Step 3: Albumin nanocarriers will interact and bind with SPARC, which will aid in retaining the nanoparticles at the tumor site.

1.7.3. Fabrication of Albumin Nanoparticles

Although *nab*-paclitaxel is manufactured through high-pressure homogenization of paclitaxel in the presence of human serum albumin,[166] there are several other ways of

preparing albumin nanoparticles that are commonly found in literature. Albumin nanoparticles can be fabricated through a variety of techniques including emulsification, controlled desolvation and thermal denaturation.[172] Here, the focus will be on preparing albumin nanoparticles by the process of controlled desolvation or coacervation. This process offers the advantage of being relatively simple to perform, easily controllable and yielding reproducible nanoparticles both in size and in polydispersity.

In the process of controlled desolvation, an aqueous solution of albumin is treated with a coacervation agent, usually an organic solvent such as ethanol, followed by chemical crosslinking (**Fig. 2.1**)[128]. The coacervation agent acts indirectly on the albumin's tertiary structure through its interaction with the surrounding water. As the solvent is added to the aqueous solution, water molecules will preferentially bind to the solvent through hydrogen binding resulting in a binary mixture that becomes an increasingly marginal solvent for the albumin.[173] Hydrophobic groups, previously buried within the albumin, become increasingly exposed in the desolvated protein and facilitate aggregation.[174] In addition, the dielectric constant of the solution significantly decreases, facilitating stronger electrostatic interactions between charged regions of the albumin monomers.[175] Together, these phenomenon bring monomers of albumin in close proximity through electrostatic interactions, yielding the self-assembly of albumin aggregates.

As the aggregates grow, there is a dramatic increase in the turbidity of the solution – a transition from transparent to opaque. Generally, without further processing, the aggregates are unstable, and can dissolve back into monomeric albumin if the coacervation agent is removed.[176] In order to allow resuspension of the aggregates in

water or buffers, a stabilization step must be performed after coacervation. One such stabilization mechanism involves chemical crosslinking of the aggregates through the use of glutaraldehyde, a homobifunctional crosslinker. Glutaraldehyde acts to couple the amine groups located predominately on lysine and arginine groups present in albumin.[177,178] Following crosslinking, purification of the particles is accomplished through repeated washing and centrifugation steps.

This process is heavily dependent on parameters such as pH, temperature, salt presence and type of coacervating agent used. Hence, the process can be controlled by carefully monitoring these parameters during the synthesis of albumin nanoparticles. By changing certain parameters, particle size, polydispersity and yield are ultimately influenced. Langer et al. have published comprehensive studies on the outcomes of several parameter variations.[179]

1.8. Dissertation Hypothesis and Overview

The objective of this dissertation is to investigate a nanomaterial approach for the conception and development of a multifunctional imaging probe along with a NIR/SWIR imaging system for the ultimate applications of targeting, identifying and treating disease states. The major imaging model system involves the controlled presentation of human serum albumin (HSA) on the surface of near infrared light (NIR) excitable rare earth-doped nanoparticles (REs). The thesis research aspires to combine multiple functionalities into a single inorganic-organic composite nanoparticle including:

1.) Optical detection both in vitro and in vivo

2.) Molecular targeting of oncogenic receptors

3.) Therapeutic delivery and controlled release

We further hypothesize that encapsulating the REs within a "shell" of albumin will

1.) Improve biocompatibility and aqueous dispersion

2.) Introduce functional groups for ligand conjugation

3.) Enhance tumor accumulation through molecular interactions

4.) Present domains which could act as regions for drug-binding

To address all of the above requirements, a two-component nanoparticle system consisting of REs and albumin nanocarriers was engineered. The REs serve as the contrast agent, which can be used for detection or tracking in a biological environment. REs can be excited with tissue transparent NIR and generate both visible and short wavelength infrared (SWIR) emissions. The benefit of using REs is rooted in their optical properties. The NIR excitation of the REs results in visible emissions through an upconversion fluorescence mechanism. Furthermore, REs also are able to generate

emissions in the SWIR through traditional downconversion fluorescence mechanisms. The SWIR emissions can be tuned by modifying the dopants in the nanoparticles without modifying any of their physical parameters. Compared to NIR, light in the SWIR has been shown to exhibit similarly low tissue absorbance with a greater reduction in light scattering. We therefore hypothesize that SWIR emissions could prove to be very useful for in vivo imaging applications.

This dissertation proposes to exploit both the optical features of REs and the biological benefits of ANCs for the purposes of tumor detection and therapy using optical imaging. First wee formulate a novel nanomaterial consisting of rare earth-doped nanoparticles in encapsulated albumin nanocarriers ((RE)ANCs or, for Chapter 2, albumin 'nanoshells', (RE)ANS). Chapter 2 focuses primarily on the in vitro characterization of the (RE)ANS system and its application toward cancer cell targeting. Chapters 3 and 4 describe the extension of this system toward in vivo imaging applications. Chapter 3 is primarily concerned with developing the tools necessary to perform SWIR-based imaging using the REs. Chapter 4 is the in vivo continuation of Chapter 2's (RE)ANS system (referenced as '(RE)ANCs' in Chapter 4) and is aimed at investigating the potential of (RE)ANCs to image cancer within a transgenic melanoma mouse model. Chapter 5 concludes with the re-engineering of albumin nanoparticles for the simultaneous delivery of multiple therapeutic agents using an advanced drug delivery approach. The overall thesis aims are as follows:

1.) To develop, characterize and molecularly target human serum albumin nanocarriers with encapsulated rare earth-doped nanoparticles for the purpose of in vitro tumor cell imaging.

2.) To demonstrate the potential of SWIR-based in vivo imaging for real-time probe detection, detailed anatomical resolution, and multi-spectral imaging using rare earth-doped nanoparticles.

3.) To evaluate the tumor targeting of (RE)ANCs in a melanoma murine model using optical techniques as a function of size and surface properties.

4.) To disrupt tumor cell growth in vitro and more effectively deliver therapeutic agents using advanced tumor penetrating drug delivery strategies.

CHAPTER 2

ALBUMIN NANOSHELL ENCAPSULATION OF NEAR INFRARED EXCITABLE RARE EARTH NANOPARTICLES ENHANCES BIOCOMPATIBILITY AND ENABLES TARGETED CELL IMAGING

Note: Sections of this chapter have been reproduced from the following publication:

Naczynski, D.J., Andelman, T., Pal, D., Chen, S., Riman, R. E., Roth, C. M., Moghe, P. V. Albumin nanoshell encapsulation of near-infrared-excitable rare-earth nanoparticles enhances biocompatibility and enables targeted cell imaging. *Small* **6**, 1631-1640 (2010).

Abstract

The use of traditional fluorophores for in vivo imaging applications is limited by poor quantum yield, poor tissue penetration of the excitation light, and excessive tissue autofluorescence, while the use of inorganic fluorescent particles that offer high quantum yield is frequently limited due to particle toxicity. Rare-earth doped nanoparticles that utilize near infrared upconversion overcome the optical limitations of traditional fluorophores, but are not typically suitable for biological application due to their insolubility in aqueous solution, lack of functional surface groups for conjugation of bio-molecules, and potential cytotoxicity. We report here a new approach to establish highly biocompatible and biologically targetable nanoshell complexes of luminescent rare-earth doped $NaYF_4$ nanoparticles (REs) excitable with 920-980 nm near infrared light for biomedical imaging applications. Our approach involves the encapsulation of $NaYF_4$ nanoparticles doped with Yb and Er within human serum albumin nanoshells to create water dispersible, biologically functionalizable composite particles. These composite particles exhibit narrow size distributions around ~200 nm and are stable in aqueous solution for over four weeks. The albumin shell conferred cytoprotection and significantly enhanced the biocompatibility of REs even at concentrations above 200 μg REs/mL. Composite particles conjugated with cyclic arginine-glycine-aspartic acid (cRGD) specifically target both human glioblastoma cell lines and melanoma cells expressing $a_v b_3$integrin receptors. Taken together, these findings highlight the promise of albumin encapsulated rare-earth nanoparticles for imaging cancer cells in vitro and the potential for targeted imaging of disease sites in vivo.

2.1. Introduction

In order to study biological and disease processes at the cellular level, fluorescent probes for in vitro and in vivo imaging are required.[127,180] To image effectively in a biological environment, optical labels must be tailored to provide both sensitivity as well as optical stability under physiological conditions.[181] Currently, the most commonly used optical labels are fluorescent organic dyes.[182] However, poor photostability and low quantum efficiency constitute major drawbacks that have limited the widespread use of organic dyes, particularly in vivo.[182-185] Semiconducting quantum dots have gained popularity as a potential alternative due to their greatly enhanced photostability and quantum yields. Quantum dots, however, also face major drawbacks due to their highly cytotoxic nature,[186,187] as well as intermittence in emission or "blinking",[185] effectively limiting their widespread use in living systems and time-resolved imaging.

Most importantly, both quantum dots and organic dyes are excited through ultraviolet (UV) or short wavelength visible light.[188] Both forms of radiation are limited by short penetration depth into biological tissues (microns),[189,190] significant autofluorescence from tissue components resulting in poor signal-to-noise ratio and, in the case of UV radiation, potentially carcinogenic and cytotoxic effects.[188,191,192] Near infrared radiation (NIR), on the other hand, generates very little autofluorescence in biological samples and is capable of penetrating tissue orders of magnitude deeper (millimeters to centimeters)[127] than UV with greatly attenuated cytotoxicity.[50,192,193]

Upconversion fluorescence imaging exploits low-energy NIR excitation to induce visible emission. $NaYF_4$ nanoparticles co-doped with ytterbium and erbium or ytterbium and thulium, in particular, are reported as being very efficient at generating visible

photons via NIR excitation (Fig 6).[194] Furthermore, Yb/Er and Yb/Tm doped $NaYF_4$ materials exhibit the highest upconversion efficiencies.[135,194,195] However, these rare-earth doped nanoparticles (REs) as synthesized are not suitable for biological applications due to their insolubility and tendency to agglomerate in aqueous solution.[196] Additionally, REs are limited by a lack of functional groups for surface attachment of ligands or other biomolecules for actively targeted delivery,[188,193,196,197] and may potentially have dose- and time-dependent cytotoxic effects.[198]

Previous approaches to render $NaYF_4$ nanoparticles hydrophilic include surface modification with silica,[198,199] mercaptopropionic acid,[200] diphosphonic acid,[201] and polymer surfactants such as polyethyleneimine (PEI) and polyvinylpyrrolidone (PVP).[188,192,196] While coating with silica has been reported to increase the fluorescence intensity from quantum dots, it can be difficult to coat nanoparticles uniformly, and further surface modification steps are required to generate functional groups on the silica for bioconjugation.[192] Additionally, many of the reagents used for silica surface modification are toxic, and care must be taken to remove residual reagents before using the particles in living systems. There has been some success with PEI surface modification, but its high cationic charge density imparts significant cytotoxicity.[202] PVP treatment results in particles dispersible in water and organic solvents, but, as with silica, subsequent steps are needed to generate functional groups on the surface for bioconjugation.

Human serum albumin nanoshells (ANS) have been demonstrated to be bio-compatible with many cell types, exhibit long half life in vivo, capable of delivering a number of biologically relevant compounds and have numerous functional entities

available for conjugating ligands, antibodies and other peptides which can bind to specific molecular receptors.[179,203-212] Nanoparticles composed of human serum albumin are also in use clinically. For example, ABI-007 (Abraxane®, Abraxis BioScience Inc, Los Angeles, CA) is a commercial, albumin-bound paclitaxel delivery vehicle,[154] which points to the translational relevance of albumin-based functional nanoparticles.

Herein, we report on the encapsulation of $NaYF_4$:Yb,Er nanoparticles (REs) in coacervated human serum albumin nanoshells functionalized with arginine-glycine-aspartic acid (cRGD) tripeptide. We observed that the composite particles were highly biocompatible in vitro, capable of selectively targeting cancerous cell lines exhibiting higher expression of cancer-specific integrin markers, and amenable to fluorescence imaging with high fidelity. Thus, these composite particles have great potential for a variety of biomedical applications ranging from imaging to drug delivery.

2.2. Methods

2.2.1. RE Synthesis

Nanoparticles of $NaYF_4$:20%Yb, 2%Er with a doped core and undoped $NaYF_4$ shell were prepared in oleylamine by a thermal decomposition method.[144] Briefly, yttrium (III) acetate hydrate (9.75 mmol), ytterbium (III) acetate hydrate (2.5 mmol) and erbium (III) acetate hydrate (0.25 mmol) were dissolved in excess trifluoroacetic acid to yield rare earth trifluoroacetate precursors. For the undoped shell, yttrium (III) acetate hydrate alone was dissolved in trifluoroacetic acid. Precursors were dried at 70°C until trifluoacetic acid evaporated, and were re-dissolved in oleylamine to yield a stock solution of 0.5 M concentration. In a typical synthesis, stock solution (2 mL), oleylamine (20 mL) and sodium trifluoroacetate (2 mmol) were stirred in a three-neck flask and gradually heated up to 100°C in vacuo over 10 min. Vacuum was stopped and the solution was then rapidly heated to 340°C under Argon for 30 min to form nanoparticles. An undoped sodium yttrium fluoride shell was created around the nanoparticles by dripping in to the reaction a solution of yttrium trifluoroacetate (1 mmol) and sodium trofluoroacetate (2 mmol) in oleylamine (5 mL) at a rate of approximately 1 mL min^{-1}. The solution was heated for another 30 min, and the reaction was then allowed to cool to room temperature. Nanoparticles were separated from the mother liquor by centrifugation at 6,000 x g, 5 min, and then washed multiple times (>4) with ethanol and methanol by repeated cycles of redispersion with sonication and centrifugation. The resulting powder was then dried at room temperature in vacuo.

2.2.2. ANS Synthesis

ANS were prepared through a modification of an established controlled coacervation technique.[179] Briefly, a 2% (w/v) solution of human serum albumin in NaCl (10 mM) at pH 8.50 ± 0.02 was prepared and adjusted with 0.1 M NaOH. Under continuous stirring at 700 RPM and room temperature, ethanol (2 mL) was added by a syringe at 1.5 mL min^{-1} to the HSA solution (500 ml). Immediately following ethanol addition, 0.24 ml of the glutaraldehyde solution/mg HSA was added to stabilize and crosslink the nanoparticles suspension. Particles were left to crosslink overnight under stirring and at room temperature.

2.2.3. (RE)ANS Synthesis

ANS were prepared with REs by sonicating the rare earth particles (0.5 mg mL^{-1}) in ethanol for approximately 75 min to ensure dispersion. Following sonication, ANS were prepared as described above using the rare earth-enriched ethanol.

2.2.4. ANS and (RE)ANS Purification

ANS were purified through three rounds of centrifugation at 16,100 x g, 8 min., 4°C followed by washing and redispersion of the pellet to the original volume with PBS. Redispersion was performed in an ultrasonication bath for 15 min.

2.2.5. Physical Characterization

To ensure that the REs were encapsulated within the ANS and to characterize the physical properties of the complexes, (RE)ANS were studied using dynamic light

scattering (DLS), transmission electron microscopy (TEM), scanning electron microscopy (SEM), and thermogravimetric analysis (TGA). Particle size distributions, polydispersity indexes and zeta potential calculations were determined using a Malvern Zetasizer. Samples were diluted 1:50 in deionized water for z-average size, or intensity mean, and polydispersity measurements and diluted 1:50 in PBS (pH 7.4) for zeta potential calculations. Z-average sizes and polydispersity indexes of three sequential sample scans (3 runs $scan^{-1}$, 120 s $scan^{-1}$) were measured at a 90° scattering angle at 37°C. Z-average potential calculations were also performed over three sequential sample scans (20 runs $scan^{-1}$, 10 s $scan^{-1}$) using the Smoluchowski model. At least 5 separate batches of particles were measured and averaged in this manner, for all tested parameters. For particle stability in cell culture media, samples were diluted 1:50 in U87-LUC culture media and analyzed as previously outlined.

REs, ANS and (RE)ANS were visualized using transmission electron microscopy, TEM, operated at 80 kV, and scanning electron microscopy, SEM, operated at 5 kV. For TEM, the (RE)ANS or ANS solutions were diluted in water then deposited on a 400 mesh Formvar backed carbon-coated copper grid. REs were diluted in chloroform and likewise added onto a copper grid. All solutions were dried at room temperature under vacuum before imaging. Samples were treated similarly for energy-dispersive X-ray spectroscopy (EDS) measurements. Energy dispersive spectra were recorded with a TOPCON 002B TEM operated at 200 kV, equipped with a PGT Omega (Princeton Gamma-Tech, Princeton, NJ) EDS detector. Samples were tilted 10 degrees and acquisition times varied due to sample stability. For SEM imaging, ANS, (RE)ANS, REs, and a mixture of unloaded ANS and REs were each diluted in water, and a drop of

diluted solution was deposited on an aluminum sample holder and dried at room temperature under vacuum. A layer of Pt was sputtered on top of the dried film. Images were captured using an in lens detector. To determine the weight percent of REs present in (RE)ANS, thermogravimetric analysis (TGA) was performed on dried powders of the samples under air at a flow rate of 20 mL min^{-1}. Samples were rapidly heated to 250°C and held at that temperature for 30 min. The temperature was then increased to 1050°C at a rate of 25°C min^{-1} and held at the final temperature for 2.5 h.

2.2.6. Emission Spectra of Nanoparticles

Prior to imaging under NIR excitation, ANS, (RE)ANS, and REs were dried to a loose powder at room temperature under vacuum. The powder was then placed on a glass slide, and the sample was excited with 980 nm laser light and emission spectra were recorded with a TCS SP2 laser-scanning confocal fluorescence microscope.

2.2.7. Functionalization of (RE)ANS

Integrin targeting cRGD and cRAD groups were attached to the (RE)ANS through a standard protein crosslinking protocol with Sulfo-LC-SPDP. Briefly, nanoparticles were resuspended in PBS-EDTA (PBS with 1 mM EDTA and 0.02% sodium azide, pH 7.5) in the final stage of purification. 1 mM of Sulfo-LC-SPDP was introduced to 2 mg of nanoparticles for 30 min under agitation. For quantification analysis, DTT was used to reduce the SPDP-albumin nanoparticles to yield the pyridine-2-thione leaving group, which has a characteristic absorbance at 343 nm. Approximately 50 mg of cRAD or cRGD was added and reacted with the SPDP-(RE)ANS for 2 h. Products were purified

through centrifugation and redispersed in PBS.

2.2.8. Protein Quantification

For determination of particle protein content, the supernatants during purification were collected, diluted 1:5 in PBS and assayed by bicinchoninic acid (BCA), using bovine serum albumin as a standard.

2.2.9. Cell Culture

U87-LUC, a human glioblastoma cell line with constitutive expression of firefly luciferase, was generously provided by Dr. Xu-Li Wang (Department of Pharmaceutics and Pharmaceutical Chemistry, University of Utah). Cells were maintained in minimal essential medium containing 10% FBS, G418 (300 mg ml^{-1}), streptomycin (100 mg ml^{-1}), and penicillin (100 U ml^{-1}). Human glioblastoma A172 cells were cultured in DMEM containing 10% FBS, 1% L-glutamine, streptomycin (100 mg ml^{-1}) and penicillin (100 U ml^{-1}). WM239A human melanoma cells were cultured in RPMI-1640 containing with 10% FBS, streptomycin (100 mg ml^{-1}) and penicillin (100 U ml^{-1}). All cells were cultured at 37°C under an atmosphere of 5% CO_2

2.2.10. Cell Metabolic Activity

The metabolic activity of viable cells was assessed by CellTiter 96 Aqueous One Solution Reagent (3-(4,5-dimethylthiazol-2-yl)-5-(3-carboxymethoxyphenyl)-2-(4-sulfophenyl)-2H-tetrazolium, MTS), which measures tetrazolium reduction by viable cells. Reduction was measured by absorbance at 490 nm using a microplate reader.

The U87-LUC and WM239A cells were cultured on 96-well tissue culture polystyrene plates at 5,000 cells well^{-1} and incubated with ANS, (RE)ANS and REs suspended in PBS. After 24 h, MTS reagent (20 ml) was added to each well of the 96-well assay plate containing the samples in culture medium (100 ml). Plates were incubated for 4 h at 37°C in a 5% CO_2 atmosphere. Background absorbance was corrected by preparing a set of control wells without cells containing the same volumes of culture medium, test samples and MTS reagent. All measurements were done in quadruplicate. The cellular metabolic activity was calculated using the equation:

$$(1)\quad \text{Cellular Metabolic Activity} = \left(\frac{[\text{Corrected Absorbance}]_{sample}}{[\text{Corrected Absorbance}]_{control}} \right) \times 100\%$$

2.2.11. Cell Viability Assay

The numbers of both dead and live cells were quantified with the CytoTox-Glo Cytotoxicity Assay. The assay uses a luminogenic peptide substrate to measure a distinct dead cell protease release by cells with compromised membranes. Measurements were performed using a luminometer following the manufacturer's protocol. U87-LUC and WM239A cells were seeded in using 96-well, black-wall clear bottom tissue culture polystyrene plates and treated as for the MTS assay. All measurements were done in quadruplicate. The percent of dead cells was calculated using the following equation:

$$(2)\quad \text{Degree of Cytotoxicity} = \left(\frac{[\text{Corrected Dead Cell Luminescence}]_{sample}}{[\text{Corrected Dead Cell Luminescence}]_{control}} \right) \times 100\%$$

Long term cytotoxicity studies of the nanoparticles were performed using the U87-LUC cells. Cells were seeded as before and incubated with nanoparticles for 24 h. Media and nanoparticles were then removed and fresh media added every day for 7 days. On the final day, the relative number of live cells compared to a PBS negative control was determined using the following equation:

(3)

$$\text{Cell Viability} = \left(\frac{[\text{Corrected Total Cell Luminescence}]_{sample} - [\text{Corrected Dead Cell Luminescence}]_{sample}}{[\text{Corrected Total Cell Luminescence}]_{control}} \right) \times 100\%$$

2.2.12. Active Targeting of Functionalized (RE)ANS

To examine the active targeting of (RE)ANS, U87-LUC cells, with elevated expression of the $a_v b_3$ integrin, and A172 cells, with low expression of the integrins, were cultured on poly-D-lysine (PDL)-coated Lab-Tek chambers, 50 mg ml^{-1} PDL per well, at 20,000 cells $well^{-1}$ and incubated with cRGD or cRAD functionalized (RE)ANS for 4 h. The WM239A human melanoma cells were cultured similarly to the glioblastoma cell culture protocols and treated equivalently with cRGD or RAD functionalized (RE)ANS for 4 h. Cells were then fixed, washed and stained with DAPI. Near infrared imaging was performed using a Titanium-sapphire laser on a Leica TCS SP2 fluorescence microscope.

2.2.13. Quantification of Fluorescence Co-localization on Cells

To quantify the relative degree of co-localized fluorescence arising from the albumin shell and the REs on cells, U87-LUC and A172 cells were treated with cRGD, cRAD and unfunctionalized (RE)ANS for 4 hours. Cells were fixed, washed and stained with DAPI prior to imaging. Five sets of fluorescent images were taken for each test condition with a 40x objective. Fluorescence from the albumin shell, REs and DAPI was captured for each set of images, maintaining the same gains and offsets for each group. An established co-localization protocol was followed for image processing.[213] Briefly, all green and red fluorescence images from the albumin shell and the REs, respectively, were binarized by adjusting the image threshold to a common value. The binary images were then merged, and all yellow (green and red co-localized) pixels were selected for further processing. Masks of the cellular bodies were created using the corresponding DAPI images of the cells. The masks were applied to the yellow fluorescence images and the total yellow pixel area was quantified. The number of individual cell masks was used to normalize all results (**Supplementary Fig. S2.1**).

2.3. Results

2.3.1. Physical and Chemical Characterization of Nanoparticles

Rare-earth nanoparticles (REs) were encapsulated to form rare-earth albumin nanoshells ((RE)ANS) using controlled coacervation of human serum albumin (HSA) in an aqueous solution (**Fig. 2.1**).[179] REs dispersed in hexanes are approximately 20 nm in size as measured with transmitted electron microscopy (TEM) images (**Supplementary Fig. S2.2**). These nanoparticles are dispersible in hexanes or chloroform, but not in polar or aqueous solutions. (RE)ANS were approximately 210 nm in aqueous solution as measured by dynamic light scattering (DLS), significantly larger than 140 nm ANS formed at identical synthesis conditions. All particles exhibited low polydispersity values and negative zeta potentials in phosphate buffered saline (PBS, pH 7.4). Protein assay (BCA) indicates that ~85% of the starting HSA was incorporated into the (RE)ANS (**Table 2.1**).

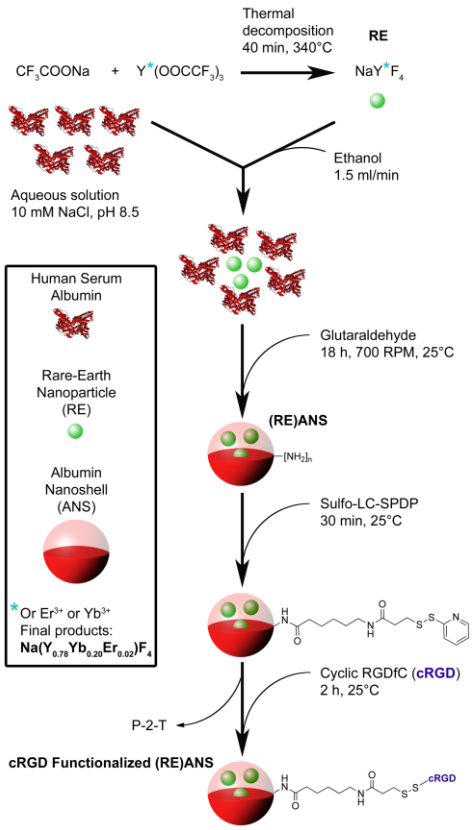

Figure 2.1 – Synthesis and Functionalization of Albumin Encapsulated Rare-Earth Nanoparticles. Schematic of the synthesis and ligand functionalization of rare-earth nanoparticles within albumin nanoshells. REs, dispersed in ethanol, are introduced to a solution of human serum albumin at a controlled rate, driving the protein monomers to aggregate around the rare earth nanoparticles. The aggregates are chemically stabilized to form (RE)ANS using glutaraldehyde, a homobifunctional crosslinker which acts on the amine groups present on the albumin. The free amine groups on the particle surface are then reacted by Sulfo-LC-SPDP, which is subsequently used for conjugating ligands containing a cysteine group, such as RGDfC (cRGD). The conjugation generates pyridine-2-thione (P-2-T), a detectable by-product which can be used to measure the extent of reaction.

The size stability of the (RE)ANS incubated in phosphate buffered saline (PBS) at 4°C was assessed over time through DLS. (RE)ANS size appeared to increase 10-15% after a period of 4 weeks with no significant aggregates forming (**Table 2.1**). Also, (RE)ANS retained their mean size when dispersed in cell culture growth media containing serum (**Table 2.1**), while showing an increase in polydispersity.

Sample	*Solvent Present*	*Size [nm]*	*Polydispersity*	*Zeta Potential* [214]	*Protein Content [μg/ml]*	*Protein Content [% yield]*
RE	Hexanes	18±1	0.320±0.018	—	—	—
RE	PBS	1525±700	1.000	—	—	—
ANS	PBS	143±5	0.059±0.035	-17.1±0.9	2970±111	59±2
ANS after 4 wks	PBS	146±1	0.073±0.004	—	—	—
(RE)ANS	PBS	208±3	0.075±0.019	-13.5±0.7	4220±76	84±2
(RE)ANS aft 4 wks	PBS	234±2	0.059±0.017	—	—	—
ANS	Media	168±4	0.260±0.037	—	—	—
(RE)ANS	Media	206±2	0.219±0.010	—	—	—

Table 2.1 – Summary of Physical Characterization of Nanoparticles – Hydrodynamic radii (size), polydispersity index, zeta potential and protein content of REs, ANS and (RE)ANS under various conditions. REs are readily dispersible in hexanes, but aggregate in aqueous solution. After encapsulation within the albumin nanoshells, the RE composites, (RE)ANS, are larger than either REs or ANS alone yet still exhibit narrow size distribution in PBS. (RE)ANS are stable in PBS at 4°C for over one month, showing only a moderate rise in size during this time. Zeta potential calculations for both ANS and (RE)ANS in PBS are negative, while percentage of HSA used during the encapsulation of the REs dramatically rises compared to the ANS alone (from approximately 60% to 85%). Furthermore, both ANS and (RE)ANS appear to retain their size when dispersed in cell culture media. ±SD.

In order to provide evidence of RE encapsulation within the nanoparticles, ANS, (RE)ANS, REs and a mixture of ANS and REs were dispersed in water, dried, and imaged with scanning electron microscopy (SEM). The images of the ANS and (RE)ANS reveal mainly spherical, fairly monodispersed and non-aggregated particles (**Fig 2.2**). In contrast, the RE and mixture samples showed extremely large agglomerates (**Supplementary Fig. S2.3**). These results were also confirmed through DLS.

The degree of RE loading within the ANS was quantified with thermogravimetric analysis (TGA). All organic matter pyrolyzes during the TGA analysis; therefore, any remaining sample mass can be attributed to the inorganic REs (**Supplementary Fig.**

S2.4). The (RE)ANS had approximately 7 wt.% remaining, which is less than the 10 wt.% of REs that were added during the synthesis of the (RE)ANS. The weight discrepancy of the (RE)ANS analysis can be attributed to residual water as well as residual oleylamine associated with the nanoparticle, adding to the total weight of the sample to reduce the weight percentage of the REs. The TGA profile of the REs alone reveals a weight loss of approximately 30 wt.% at around 1000°C, which reflects the residual oleylamine burning off the surface of the nanoparticles. The 30 wt.% loss seen with the REs alone also explains the 3 wt.% discrepancy of the REs present in the (RE)ANS analysis.

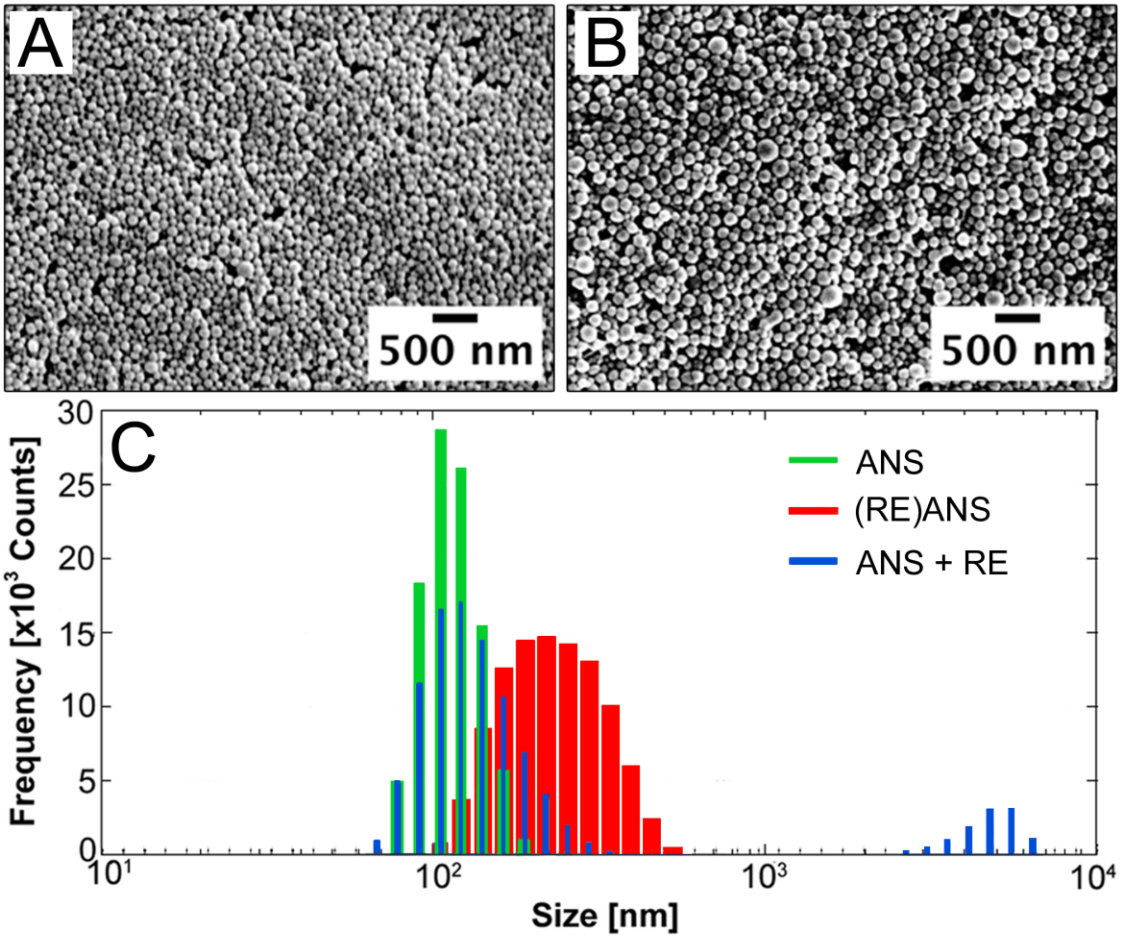

Figure 2.2 – Albumin Nanoshells and Albumin Encapsulated Rare-earth Nanoparticles are Monodisperse. In lens scanning electron microscope images of: (A) albumin nanoshells and (B) albumin encapsulated rare-earth nanoparticles, dried from water. Both albumin nanoshells and albumin encapsulated rare-earth nanoparticles appear monodisperse and spherical. (C) Dynamic light scattering (DLS) results confirm electron microscopy observations with ANS and (RE)ANS displaying monomodal size distributions, while a mixture of both pre-formed ANS and rare-earth nanoparticles contains two distinct size populations. REs alone aggregated beyond the measuring capabilities of DLS when dispersed in water.

Electron Dispersive Spectroscopy (EDS) and X-ray photoelectron spectroscopy (XPS) was performed on REs, ANS, (RE)ANS and a mixed population of REs and ANS to further confirm RE encapsulation (**Fig. 2.3A and Supplementary Fig S2.5**). The deposition of the samples on the copper grid accounts for its detection by the EDS. The characteristic ionization energies for yttrium, erbium and ytterbium were detected for RE samples. Energies for ytterbium and, to a lesser extent, erbium, were also detected for the mixed population samples, but not for ANS or (RE)ANS. These results suggest that, in the (RE)ANS sample, the REs were being shielded from the EDS X-rays by the albumin shell, confirming that the REs were encapsulated.

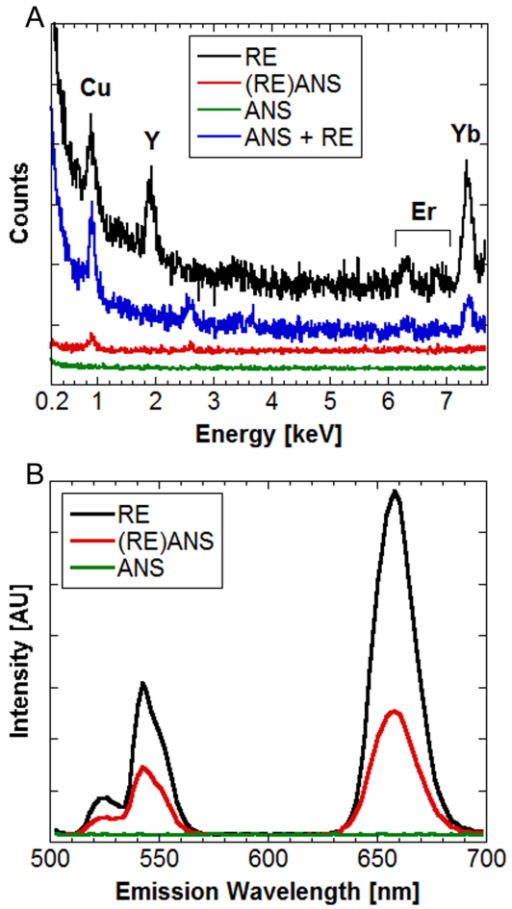

Figure 2.3 – Encapsulation of Rare-Earth Nanoparticles within Albumin Nanoshells. (A) Energy-dispersive X-ray spectroscopy (EDS) measurements for rare-earth nanoparticles and the mixed population show a distinct peak, assigned to yttrium, which arises from the rare earth dopant in the rare-earth nanoparticles. Albumin encapsulated rare-earth nanoparticles lack this peak due to shielding of the dopant from X-rays by the albumin cladding. The data are arbitrarily shifted along the y-axis for better visualization. (B) Qualitative emission spectra of samples demonstrate that albumin nanoshells alone do not emit upon 920 nm excitation, whereas emission is detected with rare-earth nanoparticles and albumin encapsulated rare-earth nanoparticles.

2.3.2. Photoluminescence of Nanoparticles

Glutaraldehyde cross-linking of the albumin present in the ANS and (RE)ANS imparted detectable fluorescence across a range of excitation wavelengths.[215] Unloaded ANS displayed strong, green emission when excited with 488 nm light, enabling the albumin shells to be localized during in vitro studies. The emission spectra upon 920 nm excitation of a dried powder sample of REs, (RE)ANS, and ANS were recorded to determine the effects of the albumin shell on the optical properties of the REs. The ANS showed no emission upon near infrared (920 nm) excitation. The peak positions of the REs and the (RE)ANS were similar, the only difference being intensity (**Fig. 2.3B**).

2.3.3. In vitro Cytotoxicity of Nanoparticles

Following the characterization of the particles, we performed in vitro testing to determine cytotoxicity and specific targeting. Both the MTS and Live/Dead assays were performed on U87-LUC human glioblastoma and WM239A human melanoma cells incubated with varying concentrations of (RE)ANS for 24 h. The MTS assay measures the metabolic activity of viable cells whereas the Live/Dead assay measures directly the number of dead cells in cell populations. The MTS assay reveals that non-encapsulated REs caused significantly greater cytotoxicity compared to (RE)ANS at 2.5 mg REs ml^{-1} for U87-LUC cells and 25 mg ml^{-1} for WM239A cells (Fig 10a, c). The Live/Dead assay showed that REs elicited significantly higher levels of cell death than (RE)ANS at every tested concentration in both cell lines (**Fig. 2.4B,D**).

In addition, (RE)ANS appear to reduce the degree of cell death in U87-LUC cells compared to REs at concentrations of 25 mg ml^{-1} and higher over the course of 7 days

(**Supplementary Fig S2.6**). After exposing the cells to nanoparticles for 24 h, media and nanoparticles were removed and fresh media added daily to cells for 1 week. Encapsulation in the form of (RE)ANS attenuated RE-induced cytotoxicity at 25 mg ml^{-1} concentrations and significantly improved the biocompatibility of the rare-earth nanoparticles at 250 mg ml^{-1}.

2.3.4. Active Integrin Receptor Targeting using cRGD Functionalized Nanoparticles

(RE)ANS were functionalized with various cyclic tripeptides using a standard crosslinking procedure conjugating the free amine groups on the albumin shell to thiol groups present on the ligands. The coupling procedure utilized the heterobifunctional crosslinker, Sulfo-LC-SPDP, to covalently link the tripeptide ligands to the primary amine groups on the albumin shell surface. The concentration of Sulfo-LC-SPDP reacted with the nanoshells was used to control the extent of coupling. The conjugation of the tripeptides, which were added to the Sulfo-LC-SPDP modified shells in excess, generated pyridine-2-thione, a detectable by-product displaced from the thiol reactive portion of Sulfo-LC-SPDP that was monitored to estimate the degree of ligand conjugation. (RE)ANS, conjugated with either cRGD or cRAD, generated approximately 80 nmoles of pyridine-2-thione per mg of human serum albumin following coupling corresponding to the amount of ligands bound to the nanoshells.

(RE)ANS were functionalized with either cRGD, which targets the integrin a_vb_3, or, as a negative control, cyclic arginine-alanine-aspartic acid (cRAD), which does not have affinity for a_vb_3. To confirm receptor specific targeting, (RE)ANS functionalized with cRGD were incubated with highly a_vb_3 expressing U87-LUC and with low a_vb_3

expressing A172 cells (Fig 11). [216] Near infrared-excited, fluorescent images of cRGD functionalized particles incubated with the U87 cells show particles distributed in a punctate pattern primarily throughout the cellular cytoplasmic space. The U87 cells treated with non-functionalized or cRAD functionalized (RE)ANS showed little particle accumulation. Fluorescent images of the A172 cells incubated with cRGD particles show little to no association of particles with cells, and appear similar to the images of A172 cells treated with cRAD functionalized (RE)ANS or un-functionalized (RE)ANS (data not shown). Quantification of fluorescence within the cell body was significantly elevated in U87-LUC cell line treated with cRGD functionalized (RE)ANS over 4 h in relation to that seen in the A172 cells.

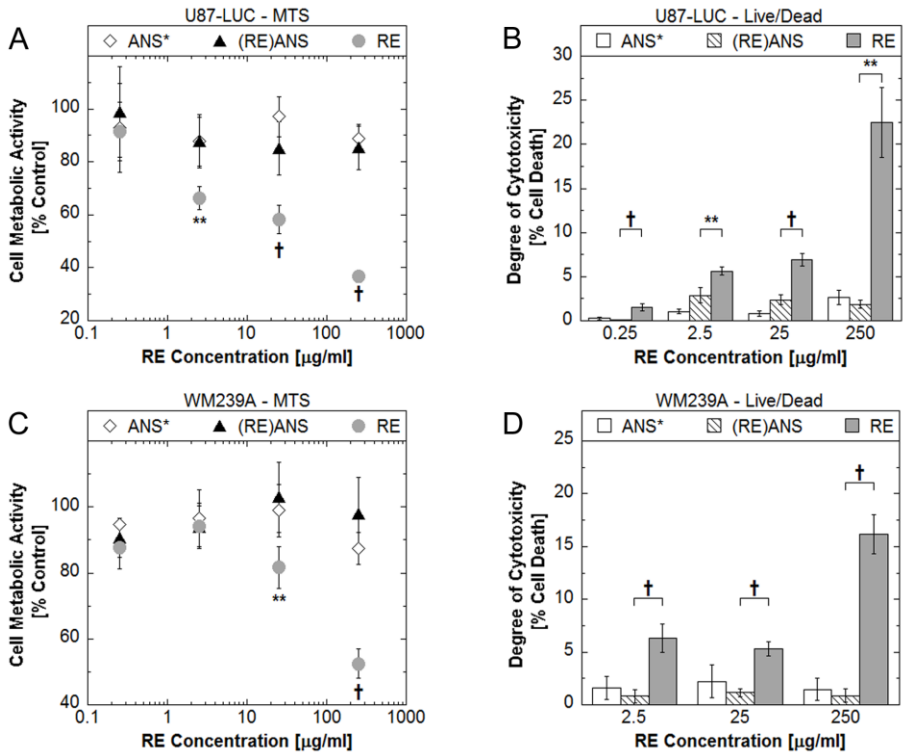

Figure 2.4 – Albumin Encapsulation of Rare-Earth Nanoparticles Provides Cyto-Protective Effect. (A) MTS and (B) Live/Dead assays of U87-LUC cells, and (C) MTS and (D) Live/Dead assays of WM239A cells incubated with samples for 24 h reveal that the albumin cladding enhances the biocompatibility of rare-earth nanoparticles at elevated concentrations. The MTS assays show a significant reduction in cellular viability, relative to a PBS control, in the U87-LUC and WM129A cells at 25 µg/ml and greater concentrations of rare-earth nanoparticles, but not when exposed to albumin encapsulated rare-earth nanoparticles (A, C). Similar results were seen in the Live/Dead assays of the U87-LUC and WM129A cells exposed to the nanoparticles (B, D). The assays show significant cell death when both cell types were exposed to all tested concentrations of rare-earth nanoparticles, while no change when incubated with the

albumin encapsulated rare-earth nanoparticles. The albumin encapsulated rare-earth nanoparticles were normalized to the total amount of rare-earth nanoparticles encapsulated. *ANS concentrations were normalized to protein content in (RE)ANS. ± SD; †, $P < 0.01$; ** $P < 0.05$, REs compared to (RE)ANS (*t* test).

Particles were also incubated with WM239A human melanoma cells, which are known to express high levels of the $a_v b_3$ integrin.[217] After 4 h, the (RE)ANS functionalized with cRGD accumulated around the WM239A cells whereas nonfunctionalized and cRAD conjugated particles showed low levels of cellular association, as was seen with the U87-LUC cells (**Supplementary Fig. S2.7**). Furthermore, cRGD functionalized particles exhibited significantly more cellular internalization compared with non-functionalized particles during the same incubation times.

2.4. Discussion

The overall goal of this work was to investigate a new approach to encapsulate $NaYF_4$:Yb,Er nanoparticles to yield water dispersible, biocompatible, luminescent nanoparticles capable of targeting specific cell types for multifunctional applications. Typically, $NaYF_4$:Yb,Er nanoparticles are hydrophobic as synthesized and thus require further surface modification to become dispersible in water. Many of the existing coating methods have issues of toxicity, poor stability in water, or require numerous steps to create functional groups on the particle surface for further conjugation to bio-molecules. We demonstrate that our nanoparticles can be efficiently fabricated, are water dispersible, show enhanced biological stability and viability and feature active targeting to tumor cell lines, while retaining their optical properties.

The encapsulation of $NaYF_4$:Yb,Er nanoparticles within albumin nanoshells was enabled by the controlled coacervation of monomeric human serum albumin around the nanoparticles. The DLS, TEM, and SEM data reveal that the (RE)ANS samples are very similar in size and morphology to ANS control samples, and they differ in size and appearance from a sample of pre-formed ANS simply mixed with REs. The size discrepancy between DLS and TEM/SEM for the ANS arises from hydration effects. The EDS data also supports encapsulation, for if the REs were surface bound to the ANS or otherwise associated with them, characteristic X-rays of ytterbium and erbium would be detected via EDS, as seen in a mixed population of pre-formed ANS and REs. However, because the REs are within the ANS, the X-rays from the EDS do not penetrate to the core, and thus no signal is seen from the rare earth elements. Therefore, based on the

EDS data, taken in conjunction with the DLS, TEM, SEM and the emission data, we determined that the REs are encapsulated within the ANS.

The REs exhibited cytotoxicity at concentrations of 2.5 mg mL^{-1}, while the (RE)ANS exhibited significantly reduced cytotoxicity after 24 h incubation with cells even at the maximum tested concentration (250 mg mL^{-1}). The toxicity of the REs may be due to remnant oleylamine (the nanoparticle solvent and stabilizing agent on the surface of these particles), which has been shown to elicit cytotoxicity.[218] The TGA profile of the REs alone reveals a weight loss attributable to residual oleylamine on the surface of the nanoparticles. We believe that the albumin shell shields the cells from the oleylamine and that as a consequence the (RE)ANS confer enhanced cyto-compatibility to the REs. We have imaged cells incubated with (RE)ANS for approximately 5 days *(*data not shown*)* and still observe fluorescence from the cross-linked albumin, suggesting that the albumin shell has maintained its integrity over this time course. The long-term cytotoxicity studies of nanoparticle exposure support these observations.

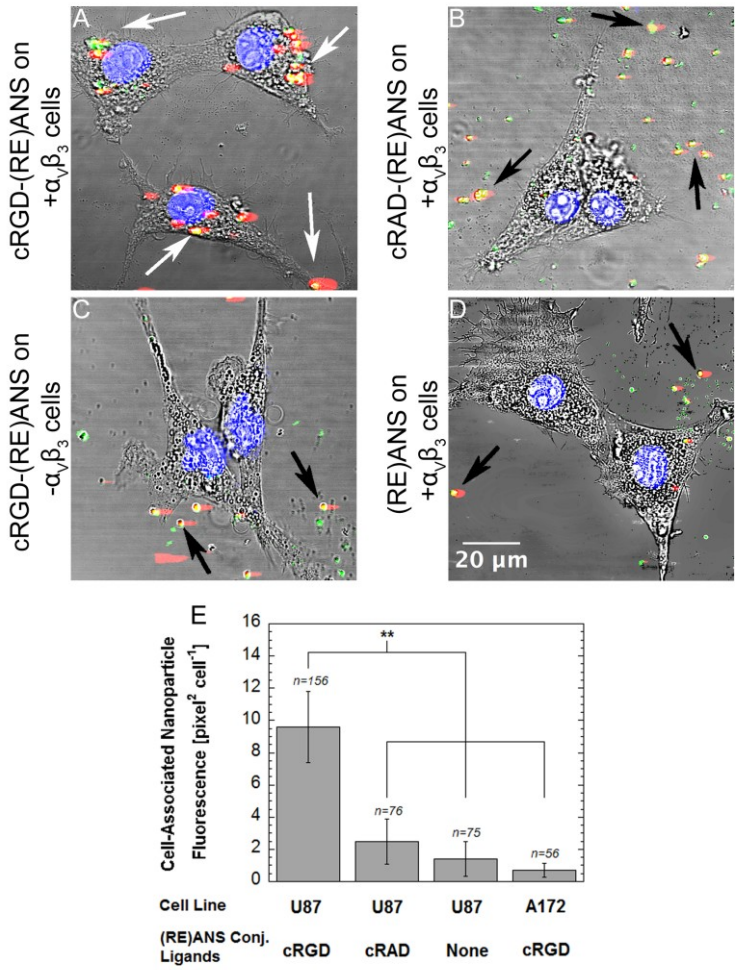

Figure 2.5 – Receptor-Mediated Targeting of Albumin Encapsulated Rare-earth Nanoparticles to Differential Integrin Expressing Human Glioblastoma Cells. Near infrared-excited fluorescent images of human glioblastoma cells with high and low expression of the $\alpha_v\beta_3$ integrin incubated for 4 h with: (A,C) 25 µg/ml cRGD functionalized albumin encapsulated rare-earth nanoparticles (B) cRAD functionalized, and (D) unfunctionalized albumin encapsulated rare-earth nanoparticles. Transmitted light and fluorescence image merges show that the highly integrin expressing U87-LUC cells readily internalize albumin encapsulated rare-earth nanoparticles conjugated with

cRGD, as shown by the white arrows, but not when conjugated with (B) cRAD or (D) unfunctionalized, indicated by the black arrows. (C) A172 cells with reduced expression of $\alpha_v\beta_3$ integrin show no significant cellular uptake of particles when incubated with cRGD functionalized (RE)ANS for 4 hours. Green – autofluorescent, internalized albumin nanoshells; red – REs; yellow – co-localization of signal; blue – nuclear stain. 63x immersion, 2.5x zoom. (E) Quantification of co-localized nanoparticle fluorescence signal by pixel area per cell (*n* represents number of cells counted). Values of fluorescence around cells confirm targeting of cRGD conjugated (RE)ANS seen in selected images. ± SEM; ** $P < 0.05$, one-way ANOVA, Tukey post-hoc.

Once the biocompatibility of the particles was established, we then functionalized the particles with a ligand (cRGD) to selectively target cells which over express the a_vb_3 integrin receptor. Integrins are a family of heterodimeric transmembrane proteins that mediate both cell-to-cell and cell-to-extracellular matrix (ECM) adhesion. Involved in development, tissue repair, immune responses and hemostasis,[219] integrins are present on the surface of many cells, but certain members of this family are highly expressed on tumor cells[220-222]. The $\alpha_v\beta_3$ integrin, in particular, has been shown to play a role in angiogenesis and metastasis in many tumors,[223,224] including melanoma, glioma, neuroblastoma, breast and prostate cancer.[220,225-227] For this reason, $\alpha_v\beta_3$ is an attractive targeting marker for locating and identifying cancer cells.[220,226,228,229] Antagonists of $\alpha_v\beta_3$, such as the cyclic arginine-glycine-aspartic acid (cRGD) tripeptide motif, are capable of

blocking both tumor cell metastasis and angiogenesis while providing a means of targeting cancer cells expressing the integrin.[230,231]

Cells incubated with (RE)ANS were imaged by near-infrared excitation fluorescence microscopy. The characteristic streaking of the RE emission arises from the significantly slower emission decay of the particles compared with a conventional organic fluorophores.[195,232,233] Even when a particular spot is no longer being excited, emission will still be detected because the microscope scan speed is too rapid to allow for the extended decay time. From the fluorescence images, it is clear that the highest degree of particle association with cells occurs in the case of cRGD functionalized particles with U87 glioblastoma cells. This is due to the targeting of the ligand cRGD on the surface of the particles to the receptor $a_v b_3$ on the surface of these cells, indicating that the receptor binding properties of the ligand are maintained after functionalization, and that the composite nanoparticles are capable of specific cell targeting. By 4 hours, the functionalized nanoparticles were not internalized but mostly sequestered at the membrane (**Supplementary Fig. S2.8**) whereas a low level of uptake is observed for the unmodified nanoshells, which is not unexpected since it has been shown that albumin nanoparticles are passively internalized by cells.[179]

The focus of this work was to show that cRGD-functionalized (RE)ANS can effectively and preferentially target a molecular marker on cell surfaces expressing a cognate receptor, enabling detection of cancer cells in vitro. The nanoshell system size falls within the range appropriate for cell/tissue targeting and visualization. Several other groups have modified albumin nanoshells of sizes comparable to or larger than nanoshells reported here for similar *in vitro* and in vivo applications.[207,209,211,234]

Experiments have shown that the threshold for this effect in liposomes is approximately 400 nm and that sizes of carriers below 200 nm are more effective at vascular penetration.[89-92] The target size of the designed (RE)ANS composite particles in this study was approximately 200 nm, however, it is feasible to fabricate (RE)ANS configurations down to about 100 nm in diameter by modulating the salt concentration, should size be a limiting factor in vivo. We selected ~20 nm RE particles for this study, although in theory we could have explored a range of particle sizes, which in turn could influence the signal to noise ratio. Using variable RE sizes and ANS sizes, a controlled range of (RE)ANS can be developed in the future and the near infrared excitation intensity quantified as a function of RE size and concentration. In addition to imaging, the RE-ANS may prove useful, with further development, for therapeutic purposes as well. Indeed, the Abraxane formulation of paclitaxel in albumin nanoparticles is approved for clinical use by the U.S. Food and Drug Administration, and research has been reported on the use of albumin nanoparticles for drug and nucleic acid formulation and delivery.[207,211] The ability of albumin nanoparticle to release the therapeutic cargo within cells in such a way that it becomes accessible to its intracellular target would be integral to these applications. The (RE)ANS system also combines features of drug carriers with imaging modalities, a multifunctional platform that can optically track the tumor cells to which drug has penetrated, which would be relevant to evaluation of the efficacy of nanoparticle-based therapeutics.

2.5. Conclusion

The nanocomposite materials developed and presented here exhibit narrow size distribution, cellular targeting, and are capable of imaging tumor cells in vitro. Our results indicate that the albumin nanocarrier encapsulation of REs yields a significant reduction of RE toxicity, an aqueous-dispersible encapsulate, and surface groups capable of chemical conjugation for the purpose of cellular targeting. Functionalization of (RE)ANS with cRGD allowed for rapid and selective targeting of established cell surface receptors commonly over-expressed in a wide range of tumors.

2.6. Supplementary Figures

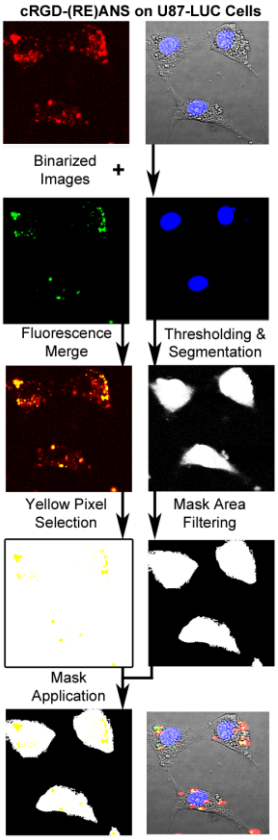

Supplementary Figure S2.1 – Quantification of Cell-Associated Nanoparticle Fluorescence – Representative images quantified for cRGD-(RE)ANS targeting around U87-LUC cells using the nanoparticles' fluorescence. Green and red fluorescence images from the albumin shell and the REs, respectively, were first binarized and merged generating a composite image. Yellow pixels were then selected and filtered for further processing. In parallel, masks of the U87-LUC cell bodies were created from the DAPI-stained nuclei images. The masks were filtered by area then applied to the filtered fluorescence images.

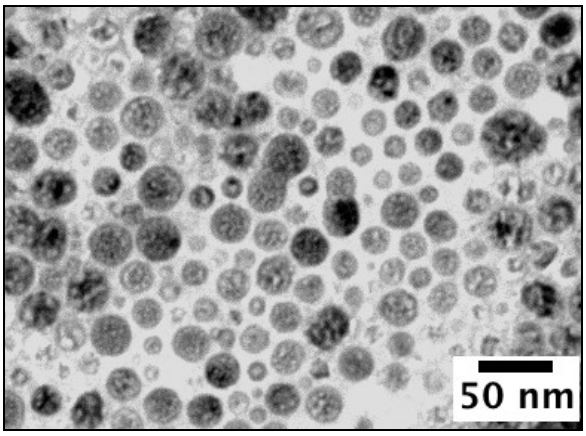

Supplementary Figure S2.2 – TEM of REs. REs appear spherical in morphology and are approximately 20 nm in diameter as seen by TEM.

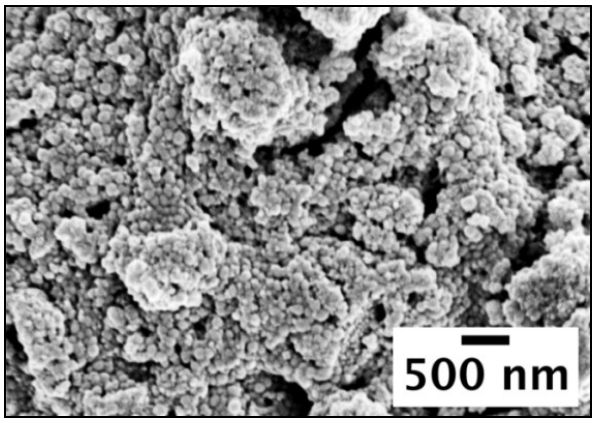

Supplementary Figure S2.3 – SEM of Pre-Formed ANS Mixed with REs. Significant aggregation and irregular morphology can be observed with SEM imaging of a mixture composed of pre-formed ANS mixed with REs. The images strongly indicate a lack of encapsulation between the ANS and REs, strikingly different from SEM images of (RE)ANS samples seen in Figure 2.2

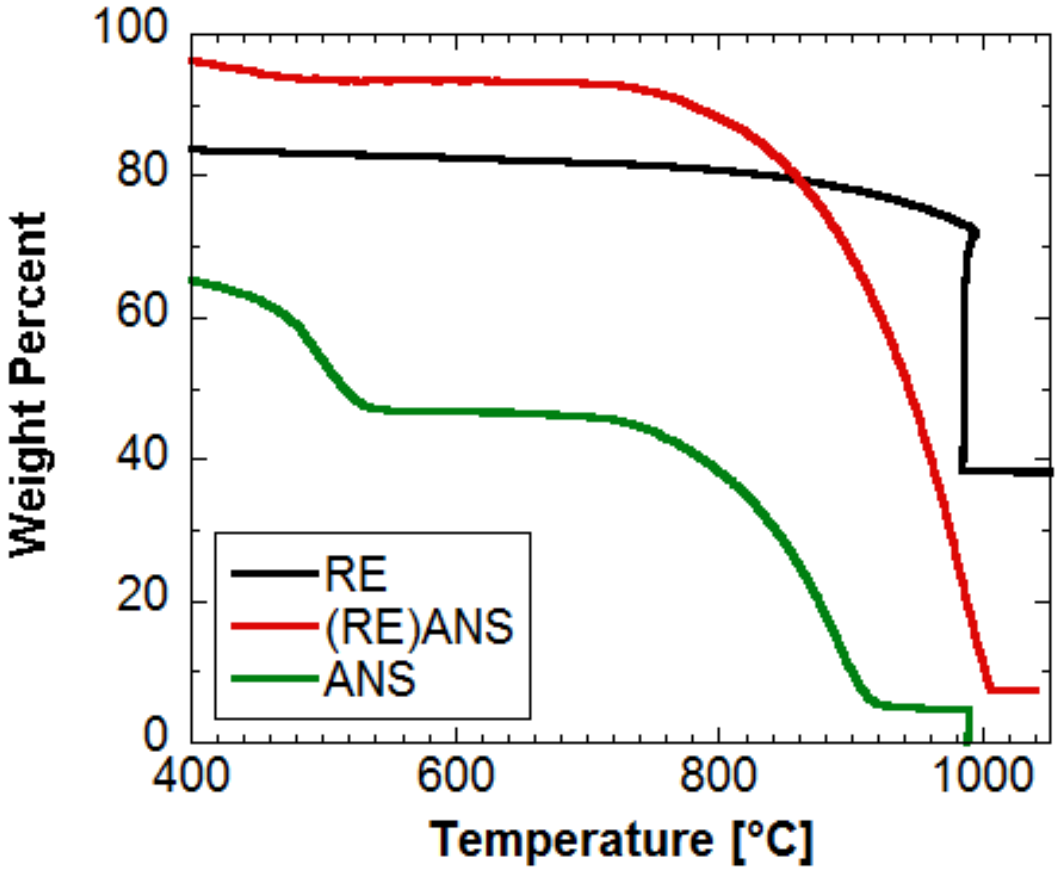

Supplementary Figure S2.4 – Confirmation of Rare-earth Nanoparticle Incorporation Within Albumin Nanoshells Via Thermogravimetric Analysis. Thermogravimetric analysis (TGA) of samples reveals that albumin nanoshells disintegrate completely at elevated temperatures while albumin encapsulated rare-earth nanoparticles loaded with approximately 10% rare-earth nanoparticles (w/w) show approximately 7% weight remaining. All samples began at approximately 100 weight percent but the graph has been truncated up to 400°C to call attention to the final sample weight.

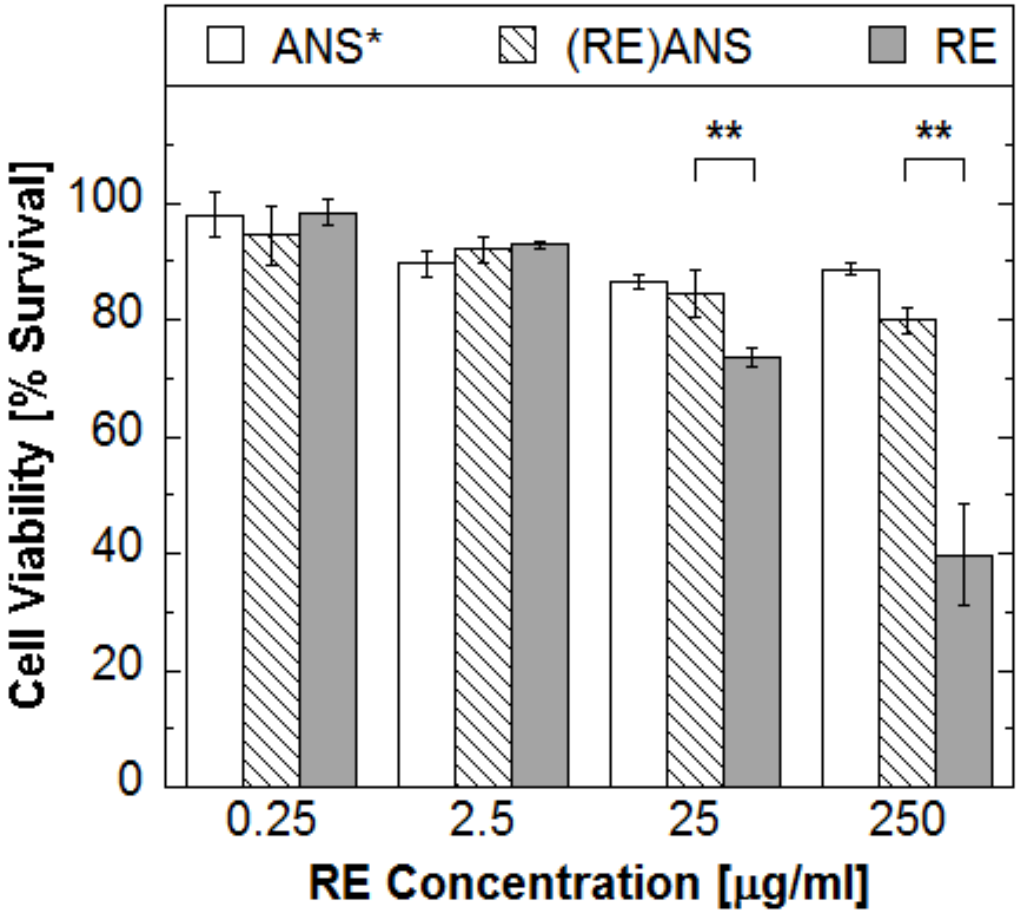

Supplementary Figure S2.6 – Albumin Encapsulation of Rare-Earth Nanoparticles Provides Extended Cyto-Protective Effect. Live/Dead assay of U87-LUC cells incubated with samples for 24 h. After 1 week, the assay reveals that the albumin coated rare-earth nanoparticles do not exhibit significant cytotoxicity. Furthermore, the total number of live cells relative to the control is reduced when exposed to 25 µg/ml and greater concentrations of rare-earth nanoparticles. The albumin encapsulated rare-earth nanoparticles showed significant improvements in the biocompatibility of the rare-earth nanoparticles at those concentrations. *ANS concentrations were normalized to protein content in (RE)ANS. ± SD; ** $P < 0.05$, REs compared to (RE)ANS (*t* test).

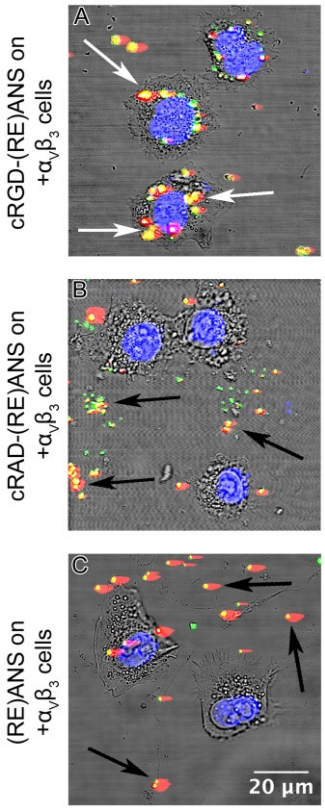

Supplementary Figure S2.7 – Receptor-Mediated Targeting of Albumin Encapsulated Rare-Earth Nanoparticles to Human Melanoma Cells. Near infrared-excited fluorescent images of WM239A human melanoma cells incubated for 4 h with: (A) 25 µg/ml cRGD functionalized albumin encapsulated rare-earth nanoparticles, (b) cRAD functionalized, or (c) unfunctionalized albumin encapsulated rare-earth nanoparticles. Cells were fixed then stained with DAPI (blue). Co-localization (yellow) of albumin nanoshells (green) and REs (red) is seen predominately around the cell body for cRGD, as indicated by white arrows, but not in cRAD functionalized sample or unfunctionalized sample. 63x immersion, 2.6x zoom.

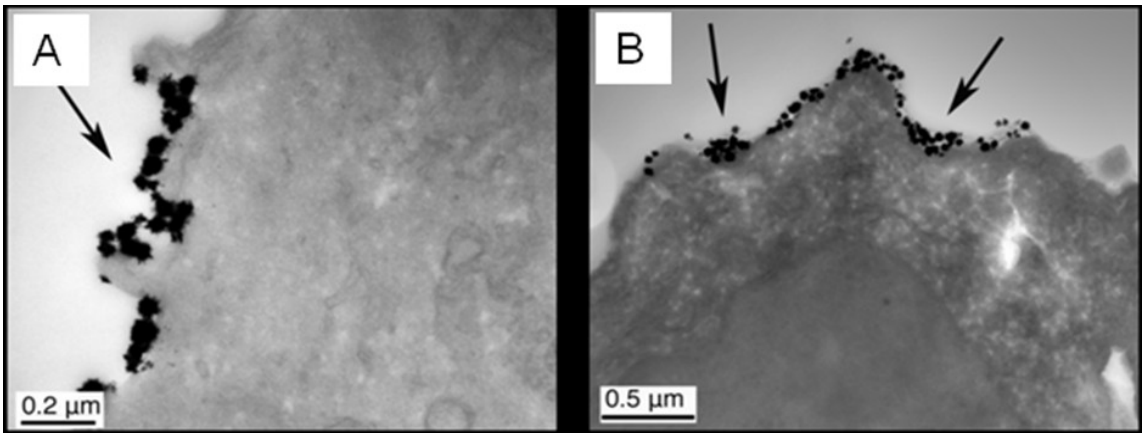

Supplementary Figure S2.8 – TEM Imaging of Glioblastoma Cells Targeted with cRGD Functionalized (RE)ANS. TEM images of U87 cells (+$\alpha_v\beta_3$) treated with cRGD functionalized (RE)ANS reveal localization on cell surface after 4 h of exposure (A, B).

CHAPTER 3

INVESTIGATION OF RARE-EARTH DOPED NANOPARTICLES AS PROBES FOR SHORTWAVE INFRARED IN VIVO IMAGING

Sections of this chapter are currently being prepared for publication elsewhere as part of an article entitled:

"Rare-earth doped nanoparticles as bioactive probes for shortwave infrared in vivo imaging"

D.J. Naczynski, M.C. Tan, M. Zevon, B. Wall, J. Kohl, A. Kulesa, S. Chen, C.M. Roth, R.E. Riman, P.V. Moghe

Abstract

The utility of in vivo optical imaging toward rapid disease screening and image-guided surgical interventions relies on brightly-emitting, tissue-specific probes that can circulate and target efficiently in vivo and be amenable to real-time imaging. Commonly used optical imaging probes have limited widespread clinical application due to their dependence on visible light, which exhibits significant absorption, scattering, and autofluorescence following photon interaction with biological tissue. While the imaging properties of near infrared light (NIR) probes are superior to visible light probes with respect to absorbance, light scattering resulting from the complex heterogeneity of biological tissue limits their penetration depth. It has been recently suggested that a new biomedical imaging window exists within the short wavelength infrared light (SWIR) region which can improve imaging sensitivity significantly over NIR. This chapter is focused on investigating the tools for establishing multi-spectral, real-time SWIR imaging at anatomical resolutions using REs. To this end, $NaYF_4$ co-doped nanoparticles (REs) were formulated and were shown to generate highly efficient SWIR emissions, providing useful luminescence for biological imaging. These findings lay the groundwork for prospects of a new generation of low-cost, rapid biomedical imaging techniques for screening disease progression.

3.1. Introduction

Real-time, non-invasive optical imaging is limited by the availability of optical probes capable of being detected and resolved in living tissues[4]. Probe detection is governed by emission intensity as well as the extent of photon propagation and volumetric energy distribution, which are linked to the absorption and scattering properties of biological media and tissues.[72] Most significantly, water, hemoglobin, melanin and lipids act as major absorbers of light while the size, composition and morphology of biological tissues control light scattering.[67,235,236] Near infrared light (NIR, 700-1000 nm) is absorbed less by tissue components than visible light[237] resulting in greater penetration and permitting deeper imaging[238] in the first "tissue transparent window." Recently, simulations have led to predictions of a second "tissue transparent window" using SWIR (above 1000 nm) exhibiting over a 30-fold reduction in scatter losses compared to NIR.[72] Reducing the amount of scattered light in optical imaging can result in better imaging fidelity and integrity by improving the amount of light transmission.[239]

Unfortunately, there are few materials that can efficiently generate SWIR and exhibit properties for safe translation into biomedical applications thereby greatly limiting the exploration and use of SWIR.[240] Currently available SWIR-emitting probes have numerous shortcomings including high toxicity, broad spectral emission and low quantum yield that must be overcome prior to clinical translation. SWIR-emitting semiconducting quantum dots (QDs) made from materials such as HgTe, CdHgTe, InP, InAs, PbS, PbSe, and PbTe are comprised of several well-known toxic elements reducing their applicability in biomedical imaging.[241,242] Weakly infrared-emitting single-walled

carbon nanotubes (SWNTs) generate broad emissions and require high-powered, pulsed excitation sources.[243,244] Broad emissions prevent the simultaneous use of multiple contrast agents for imaging pathological states limiting the amount of information that can be obtained during a single imaging session.[245,246] A unique property of optical imaging is the ability to perform "multispectral" imaging of several events or targets at several distinct wavelengths simultaneously.[247] Imaging approaches that can only resolve individual targets provide an incomplete portrait of the heterogeneous nature and complex relations among various species in many disease states.[248] Classes of optical probes must therefore be engineered to be optically tunable while still having desirable excitation and emission properties for tissue imaging. Furthermore, probes that require high-powered excitation have limited clinical translation due to the potential for tissue damage from prolonged exposure to heat.[249]

NIR-excitable rare-earth doped $NaYF_4$ nanoparticles (REs) have gained attention for biomedical imaging due to their relatively biocompatible composition in contrast to QDs. They have favorable optical properties, including narrow emission bandwidths, large Stokes shifts, long fluorescence lifetimes and photostability.[142,250-252] To date, imaging with REs has been focused primarily on exploiting upconversion fluorescence, an anti-Stokes process whereby low energy NIR light is used by REs to generate higher energy visible or ultraviolet (UV) emission.[253] Recently, there has been growing interest in utilizing the highly efficient SWIR emissions which are also produced by exciting REs, opening the possibility for SWIR-based biomedical imaging.[130,141]

However, comprehensive studies evaluating the physical and optical properties of REs for in vivo SWIR imaging are lacking. Here, we report on the systematic

engineering of a multispectral library consisting of uniquely-emitting SWIR REs which can be excited by a single, low-powered laser source. In the process, we have designed and tested a highly translatable in vivo SWIR imaging system and post-processing workflow methodology. Our findings confirm the dramatic improvements of SWIR transmittance through several major tissue absorbers over visible light and highlight the reduced scattering of SWIR compared to NIR, examining the potential of SWIR-based imaging approaches. We have presented proof-of-concept applications for improving biomedical optical imaging using SWIR extending the current paradigm for non-invasive, deep tissue imaging using light-based probes.

3.2. Methods

3.2.1. Synthesis of REs – In Collaboration with Dr. Richard Riman's Group

$NaYF_4$:Yb,Ln (Ln = erbium (Er), holmium (Ho), praseodymium (Pr) and thulium (Tm)) powders (RE(Ln)) were prepared using either a solvothermal decomposition or hydrothermal method to synthesize nano- and micron-scale particles, respectively.

The nano-scale REs in vivo imaging studies were synthesized through solvothermal decomposition of rare earth trifluoroacetate precursors in oleylamine as described previously.[128] Core precursor solution was prepared by dissolving stoichiometric amounts of 99.9% erbium triflouroacetate, 99.9% yttrium trifluoroacetate, 99.9% ytterbium trifluoroacetate (GFS Chemicals, Columbus, OH) and 98% sodium trifluoroacetate (Sigma Aldrich, St. Louis, Missouri) were dissolved in oleylamine. The shell solution was prepared by dissolving stoichiometric amounts of the sodium and yttrium trifluoroacetates in oleylamine. The core solution was then heated to 340°C under vigorous stirring in an inert argon atmosphere to allow the formation of the core particles. The shell precursor was then added and, after cooling, the synthesized nanoparticles were washed three times in ethanol by centrifuging at 15 000×g (Beckman Coulter Inc., Avanti J-26 XP, Fullerton, CA) and freeze-dried at -40°C (SP Industries Inc., VirTis AdVantage Plus Warminster, PA).

The micron-sized REs used for optical measurements were synthesized using a hydrothermal process.[254] Stoichiometric amounts of 99.8% yttrium (III) nitrate, 99.9% ytterbium (III) nitrate, 99.9+% lanthanide (III) nitrate (where lanthanide = holmium, praseodymium, and thulium), 99.0% sodium fluoride, and polyvinyl-pyrrolidone (Sigma Aldrich, St. Louis, Missouri) were mixed in 20% ethanol. The mixture was then heated at

240° C forming particles which were then washed three times in ethanol followed by three times in deionized water by centrifuging at 10,000×g (Beckman Coulter Inc.), and dried at 70°C in an oven (Thermo Scientific Thermolyne, Waltham, Massachusetts).

Pellets were made using RE(Er)s prepared by solvothermal decomposition. Approximately 0.2 g of freeze-dried RE(Er) powder was pressed (Carver Laboratory Press, Menomonee Falls, WI) for 30 seconds with 2 tons of force creating a 2 cm pellet.

3.2.2. Physical and Optical Characterization of Phosphors

REs were chemically, physically and optically characterized using transmission electron microscopy (TEM), energy dispersive x-ray spectroscopy and optical spectroscopy.

Particles were visualized by using a TEM instrument (JEOL 2010F, Tokyo, Japan) operated at 200 kV. After synthesis, REs were washed with an ethanol/methanol solution and resuspended in toluene, sonicated and deposited on a 400-mesh Formvar-backed carbon-coated copper grid (EMS, Hatfield, PA). Solutions were dried in an oven at 60°C before imaging. To determine the average size of REs, approximately 100 particles were measured from acquired TEM images.

Energy-dispersive X-ray (EDX) spectroscopy area scans of the powder samples were completed to determine their elemental composition. The measurements were done using the Carl Zeiss Σigma field emission scanning electron microscope (Carl Zeiss, Carl Zeiss SMT Inc., Peabody, MA) at an accelerating voltage of 25 kV with a working distance to 8.5 mm for an aperture of 30 μm. The EDX elemental composition was

determined by comparing relative peak intensities together with the corresponding sensitivity factors of each element and assuming their total intensities to be 100%.

The emission spectra of powdered REs held in a 0.5 cm path length cell were recorded following excitation using a 2.5 W 975 nm photodiode (model BWF-OEM 975, BW Tek, Newark, NJ). The emission from the sample was collected using a FSP920 Edinburgh Instruments spectrometer (Edinburgh Instruments, Livingston, United Kingdom) that was equipped with a Hamamatsu G5852-23 thermoelectrically cooled shortwave infrared sensitive InGaAs photodiode.

Optical efficiency measurements were performed using a modification of the C9220-03 quantum yield measurement system from Hamamatsu (Hamamatsu, Bridgewater, NJ) as described previously.[255] We have demonstrated optical efficiency (OE), which is defined as the ratio of emitted to incident power, can be used to measure the relative emission intensity of the REs. Briefly, an integrating sphere was set up in the reflectance mode to measure total integrated reflectance of a pressed phosphor pellet (2 cm diameter, ~0.2 g). The PD300-IR power detector (Ophir-Spiricon, Logan, UT) which measures the power of emitted light was used in place of the photomultiplier tube that was originally on the C9220-03 quantum yield measurement system

Images of variously formulated phosphors in cuvettes were taken using a digital camera (Canon Powershot SD780IS, Lake Success, NY) after excitation with an infrared laser diode (WSTech, Toronto, Ontario) operating at 980 nm and 100 mW. RE(Ln) (Ln = Er, Ho, Tm, Pr) were sonicated in DMSO at various concentrations (Er and Ho = 1 mg ml^{-1}, Tm = 4 mg ml^{-1}, Pr = 10 mg ml^{-1}) and the visible emission captured after excitation.

3.2.3. Tissue Attenuation and Scattering Measurements

Scattering of light at 1525 nm and 808 nm was captured with a thermoelectric-cooled Indium Gallium Arsenide (InGaAs) SWIR camera (Goodrich, Princeton, NJ) with a detection range from 800 to 1700 nm fitted with a 25 mm focal length SWIR Lens (StingRay Optics, Keene, NH). A pressed pellet of RE(Er) nanoparticles was irradiated with 975 nm light generating 1525 nm emission and imaged through increasing depths of phantom tissue. Excitation was performed with a 975 nm photodiode coupled to a 600 μm fiber optic cable placed directly underneath the 2 cm pellet. Phantoms were made from 1% agarose and 1% Intralipid as the primary scattering source. Parallel experiments were performed with 808 nm light emitted from a 600 μm fiber optic cable coupled 808 photodiode (BW Tek, Newark, NJ). Appropriate filters were positioned in front of the camera for each set of measurements. An 1100 nm longpass and an 850 nm shortpass filter (Thor Labs, Newton, NJ) were used for the SWIR and NIR measurements, respectively. Measurements were quantified by mean intensity around an ROI using camera software. The initial intensities of both SWIR and NIR signals were adjusted to similar values before phantoms were applied using the camera software quantification to more accurately compare attenuation.

Absorption measurements of mouse tissue and organs were carried out using an integrating sphere of a double beam spectrophotometer (Perkin-Elmer Lambda 9, Wellesley, MA). Samples in 0.5 cm cuvettes were mounted in the path of the incoming beam of the integrating sphere and their absorption was measured. Various biological tissue samples including liver, spleen, kidneys, lungs, heart, brain, muscle, fat, bone, skin, peritoneum cavity and tumors were taken from TGS mice following perfusion of the

animals. All samples were rinsed and left in PBS after harvesting. Blood samples were also collected in EDTA collection tubes for the analysis. All samples were left on ice and measurements were taken within several hours of harvesting.

In order to measure the tissue transmittance of SWIR compared to visible light, optical efficiency measurements were performed using the infrared and visible emission of a pressed pellet of RE(Er) nanoparticles as previously described.[255] All experiments were repeated with three different sets of organs, tumors and blood samples.

For comparing the loss of signal resolution between SWIR and visible light, ~0.2 g of RE(Er)s were patterned into an "R" using multipurpose glue (Elmer's, Westerville, OH). TGS mice were sacrificed and intestinal tracts removed. The patterned RE(Er)s were placed directly below the animal and irradiated with 980 nm light. Images were captured with either an InGaAs camera equipped with an 1100 nm longpass and two 1152 nm bandpass filters (Thor Labs, Newton, NJ) for SWIR images or a standard camera with a silicon-based image detector (Canon Powershot SD780IS, Lake Success, NY) equipped with a 900 nm shortpass filter (Thor Labs, Newton, NJ) for visible images. Two intensities of 980 nm light were used, 0.14 W cm^{-2} (low) and 0.5 W cm^{-2} (high), to excite the patterned RE(Er)s.

3.2.4. Animal Models – In Collaboration with Dr. Suzie Chen's Group

Tissue attenuation studies were performed using mutant mice that are predisposed to developing multiple melanomas (TG-3), developed by the Chen group, as described previously.[256] These transgenic mice develop spontaneous melanin-containing dermal lesions in the absence of any known carcinogen or ultraviolet radiation as early as 10-12

days. Pigmented tumors on distant organs are observed by 3-4 months. Hairless versions of the TG-3 animal, TGS, were developed for ease of tumor visualization and were used in this study. Animals were inspected for tumor development twice weekly.

Initial imaging studies were conducted using nude mice purchased from Taconic (Hudson, NY). Human melanoma cells, C8161, were injected into the dorsal area at 10^6 cells per site. All animal studies were approved by the Institutional Review Board for the Animal Care and Facilities Committee of Rutgers University and performed in accordance with institutional guidelines on animal handling.

3.2.5. Imaging Prototype and Post-Processing

A prototype of a small animal SWIR-imaging system was utilized to investigate the photonic behaviors of the nanocomposites using noninvasive fluorescence imaging. The in-house SWIR-imaging prototype consists of fiber-coupled NIR laser photodiode which operates at 980 nm and 1.4-1.5 W, and an InGaAs camera (Goodrich, Princeton, NJ) positioned approximately 12 in above the imaging surface. A collimator with a NA = 0.25 and f = 37 mm (Thor Labs, Newton, NJ) was attached to the excitation fiber to enable a uniform and constant excitation beam radius which is independent of the distance between source and animal subject. Based on the power output and collimation, the animal was irradiated with approximately 0.13-0.14 W cm^{-2} of 980 nm light. During the imaging, the excitation fiber was held at an arbitrary distance above the animal and slowly scanned across the animal's body. The distance of the fiber above the animal was held within 12 in of the animal, within the limits where the incident beam remains collimated. Any SWIR emissions were then simultaneously captured in real time by the

SWIR camera that was positioned in a fixed height above the animal. Videos were captured at 19-22 frames per second (i.e. detection exposure time 45-53 msec). Optical filters were fitted, as described earlier, onto the SWIR camera to eliminate detection of the NIR excitation source to confidently determine that only the SWIR emissions were captured. An incandescent Xe flashlight (Mini Maglite AA-Cell Flashlight, Maglite, Ontario, CA) was also to provide backlight to partially resolve the location of the mouse. Finally, black Neoprene rubber or a latex-paint-coated cardboard was used as the background surface on which the mouse was placed to reduce the amount of ambient reflected light and produce a favorable signal-to-noise ratio. Acquired SWIR video files were processed using a series of MATLAB codes to generate a background-corrected heatmap of fluorescence distribution in the animal.

In order to correct for any background fluorescence, videos of the irradiated animals were taken before nanoparticle injection and analyzed using a custom designed MATLAB script (VideoMax.m). The VideoMax.m algorithm reduces the captured video file into individual frames then analyzes each frame recording pixels with the highest intensity values at a given position. The final image is a merge of the highest intensity pixels onto a single composite image. Using ImagePro, a low radius Gaussian blur filter is then applied to the composite image to eliminate noise. Any background fluorescence is detected using a Sobel edge detection algorithm. The average intensity of all contiguous regions of background fluorescence on the animal body is recorded. Regions are identified (head, ears, upper body, lower body, anus, tail) and averaged together yielding regional averages that can be used for background subtraction in that particular animal following nanoparticle injection.

Videos of the mice post nanoparticle injection were similarly collected and analyzed in MATLAB using the VideoMax.m script. MATLAB was then used to perform a background subtraction using the regional averages recorded previously. Using a contrast enhanced, backlit infrared image, rectangular regions were designated in MATLAB that envelop the head, ears, upper body, lower body, anus, and tail. The background algorithm then subtracts the regional averages from these regions. The final, background-corrected image is named VideoMax_adj. To create a heatmap, each grey level in the VideoMax_adj image was assigned an RGB value on a gradient. In Adobe Photoshop, the black pixels were removed and any remaining color pixels are overlayed on the contrast enhanced backlit infrared image to yield the final image.

For further enhancement of low intensity images, Photoshop was used to convert the VideoMax_adj image to a tritone image of black, red, and yellow inks, with each ink curve adjusted as to create a smooth black-red-orange-yellow gradient across low grey value intensities. The intensity values were then linearly mapped from 0-255 to 3-115, which was found empirically to give the best contrast and least noise. To create the final image, a low radius Gaussian blur was applied to remove noise, and the non-black pixels of the image are overlayed on the contrast enhanced back-lit infrared image.

3.2.6. Optical Signal Phantom and In vivo Studies

SWIR signal linearity was tested using 1% agarose phantoms containing no absorbing or scattering agents. RE(Er)s were sonicated in water and serially diluted in a 96-well plate at 250, 62.5, 31.3, 15.6, 7.8, 3.9 and 0 μg ml^{-1}. Approximately 200 μL of warm agarose was then added to 50 μL of diluted RE(Er)s. Wells were irradiated and the

signal was quantified from collected images using an InGaAs camera with appropriate filter sets. Measurements were repeated in a triplicate set of wells.

For in vivo studies, RE(Er)s were mixed with matrigel (BD Biosciences, San Jose, CA) 1:1 and injected subcutaneously into TGS mice. Approximately 50 µl of the mixture was injected into loose skin over the flank and neck of the animals. Animals were irradiated with 980 nm light and images were quantified as described previously. Three sets of mice were averaged for each injected concentration.

3.2.7. Proof-of-Concept In vivo Imaging

Real-time and vascular SWIR imaging was performed in nude and xenograft mice, respectively. Catheters consisting of polyethylene tubing (BD, Sparks, MD) were surgically implanted into the tail veins of mice and secured to tongue depressors. A bolus of approximately 200 µl of 2 mg RE(Er) nanoparticles per ml was slowly infused over 5 s while an operator continuously scanned the mouse with collimated 980 nm laser light. For real-time imaging observations, the recorded SWIR videos were segmented into 5 s clips before being subjected to post-processing.

Multiplex imaging of RE(Er) nanoparticles and RE(Ho) microparticles of comparable SWIR optical efficiencies was performed in xenograft mice after intratumoral injection of 100 µl (2 mg particles ml-1). Mice were scanned with collimated 980 nm laser light before and after injection. To distinguish the separate SWIR emissions from the Er- (em: 1525) and Ho- (em: 1185) doped formulations, a combination of a longpass filter and two bandpass filters were used for each signal. To resolve the RE(Er), a combination of one 1400 nm longpass (FEL1400, Thor Labs,

Newton, NJ) and two 1550 nm (FB1550-12, Thor Labs, Newton, NJ) bandpass filters was used, while an 1100 nm longpass (FEL1100, Thor Labs, Newton, NJ) and two 1152 nm bandpass filters (FL1152-10, Thor Labs, Newton, NJ) were used to distinguish the RE(Ho). Videos were subjected to post-processing.

3.3. Results

3.3.1. Physical and Optical Characterization of REs

REs consisting of a rare-earth doped core and undoped shell were synthesized around a $NaYF_4$ host (**Fig. 3.1a**). Particles displayed a uniform shape and size distribution which was confirmed by TEM imaging (**Fig. 3.1b**). The crystal structure of the $NaYF_4$ host was characterized to be primarily hexagonal by XRD measurements (**Fig. 3.1c**). The size of the $NaYF_4$ host was controlled by utilizing two synthesis procedures. Nanoscale formulations were made using the thermal decomposition of rare earth precursors in surfactants while micronscale formulations were synthesized using a hydrothermal process (**Supplementary Fig. S3.1**). By varying the dopant schemes of $NaYF_4$:Yb,Ln (Ln = Er, Ho, Tm, or Pr) particles (REs) (**Fig. 3.1d)**, the emission properties of REs can be tailored in both the SWIR (**Fig. 3.1e**) and visible (**Fig. 3.1f,g**) range. The optical efficiency, defined as the ratio of emitted to incident power, was used to measure the relative SWIR and visible emission intensity of variously doped REs (**Fig. 3.1h**).

3.3.2. Scattering and Absorption Properties of SWIR Emissions From REs

The scattering and transmission of SWIR compared to NIR was examined using an InGaAs camera which captured the SWIR emission of an irradiated pellet of RE(Er)s through increasing thicknesses of tissue phantoms. For comparison, an 808 nm excitation source was as an NIR source. Special classes of cameras that use indium gallium arsenide (InGaAs) semiconductor technology are necessary to detect SWIR emission. Images showed increased scattering and spreading of the NIR signal compared to the SWIR **(Fig.**

3.2a), while intensity measurements performed within the camera software confirmed the that while NIR emission is reduced by close to 50% through 1 mm of phantom tissue, SWIR emission penetrates approximately three times further **(Fig. 3.2b)**

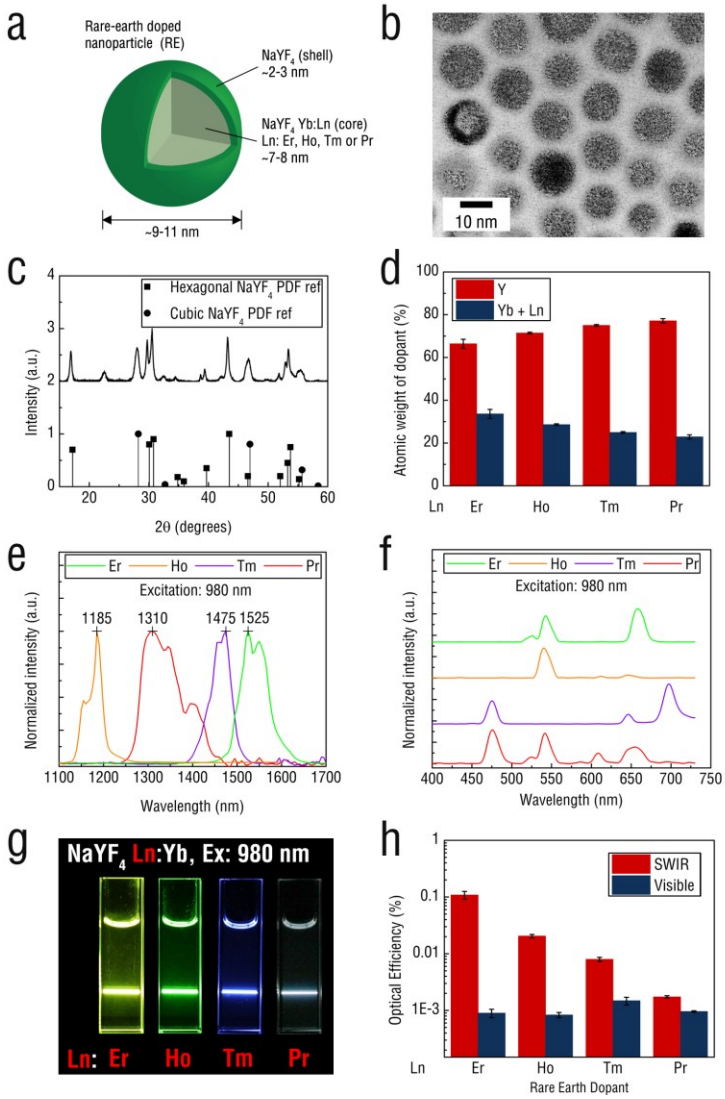

Figure 3.1 – Physical, Chemical and Optical Properties of REs. REs consist of a $NaYF_4$ Yb:Ln doped core (Ln: Er, Ho, Tm or Pr) surrounded by an undoped shell of $NaYF_4$ (a). TEM images of REs (b) show uniform 10 nm spherical particles. X-ray crystallography (XRD) plot of REs confirm a predominately hexangonal phase crystalline structure (c), which has been shown to produce efficient and intense SWIR emission. Elemental weight percentages of various REs as determined by EDS reveal consistency with doping schemes (d). SWIR emissions of REs can be tuned by changing the types of rare earth dopant used during synthesis (e). REs consisting of a NaYF4 host doped with ytterbium (Yb) and one or more elements selected from erbium (Er), holmium (Ho), thulium (Tm) and praseodymium (Pr) are favored for their low phonon energies that minimize non-radiative losses to enable intense emission spanning the SWIR region. In addition to traditional Stokes fluorescence, REs display upconversion fluorescence by exploiting low-energy NIR excitation to generate visible emissions. As with SWIR emission, the visible (f, g) emissions of REs can be tuned by changing the types of rare earth dopant used during synthesis. The optical efficiency of a specific dopant scheme was determined by integrating sphere measurements and reveals REs are more efficient at generating SWIR emissions than visible, with RE(Er)s producing the most efficient emissions in the SWIR (h). Mean values ± s.e.m.; n = 3.

The absorption properties of biological tissues obtained from a TGS mouse exhibiting pigmented tumor lesions were examined from 400 to 1700 nm. The majority of tissue samples exhibited markedly low absorbance between 1000-1350 nm as well as

between 1500-1650 nm (**Supplementary Fig. S3.2**). Strong tissue absorbers like melanin, in tumor samples, and hemoglobin, in blood samples, exhibited strong attenuation in the visible regime which was absent in the SWIR (**Fig. 3.2c**).

The tissue transmittance of SWIR and visible light emitted from the RE(Er)s was quantified using an integrating sphere operating in transmission mode. The results indicate that SWIR light at 1525 nm transmits 3- and 2-times more effectively in oxygenated blood and melanin-rich tumors, respectively, than 523/550 nm light (**Fig. 3.2d**). The differences in scattering between SWIR and visible light were observed after RE(Er)s were patterned and deposited underneath a mouse with resected intestines and irradiated with NIR excitation. While the visible emission from the RE(Er) mold was not discernible, the SWIR emission clearly resolved the "R" pattern (**Fig. 3.2e**). Increasing the incident power resulted in more visible scatter and autofluorescence, obscuring the features and boundaries of the shape.

3.3.3. Designing and Evaluating an In vivo SWIR Imaging System

Due to the lack of commercially available small animal SWIR imaging systems, we designed our own prototype consisting of low-powered (1.5 W, 0.14 W/cm^2), fiber-coupled, collimated NIR laser photodiode and a room temperature-cooled Indium Gallium Arsenide (InGaAs) SWIR camera to detect REs in vivo (**Fig. 3.3a**). Using this system, video-rate imaging could be captured at ~19-22 frames per second which translates to an exposure time of ~45-53 msec. A series of MATLAB codes were developed to generate a background-corrected heatmap of fluorescence distribution in the animals from acquired videos (**Supplementary Fig. S3.3**).

We first determined the in vitro detection threshold of the RE(Er)s using SWIR emission. REs were embedded in a 1% agarose phantom, containing no scattering or absorbing agents, and imaged over concentrations ranging from 250 to 3.9 μg ml^{-1} (**Fig. 3.3b**). SWIR signal was quantified from a region-of-interest analysis and found to correlate linearly with concentration (R^2 = 0.97) (**Fig. 3.3e**). The detection threshold of RE(Er)s was found to be at approximately 3.9 μg RE(Er)s ml^{-1} (**Fig. 3.3d**).

We next measured the SWIR detection of RE(Er)s in living mice. RE(Er)s were mixed with Matrigel at various concentrations and injected subcutaneously into nude mice. Imaging was then performed and the SWIR signal was evaluated as for the in vitro studies (**Fig. 3.3c**). Again, SWIR emissions were found to correlate linearly with concentration (R^2=0.98) (**Fig. 3.3f**).

3.3.4. Proof-of-Concept Biomedical Applications for SWIR Imaging

To demonstrate real-time SWIR imaging, RE(Er)s were intravenously injected into nude mice via catheterized tail veins. Following injection, SWIR emissions were identified in the tail vein followed by the heart and lungs before finally accumulating in the liver and spleen (**Fig. 3.4a,b**). In parallel, replicate animals were sacrificed and dissected as closely to each timepoint as possible. SWIR emissions from excised organs confirm the localized distribution of RE(Er)s in tissues at each timepoint. The accompanying RE(Er) upconversion visible signal was notably absent.

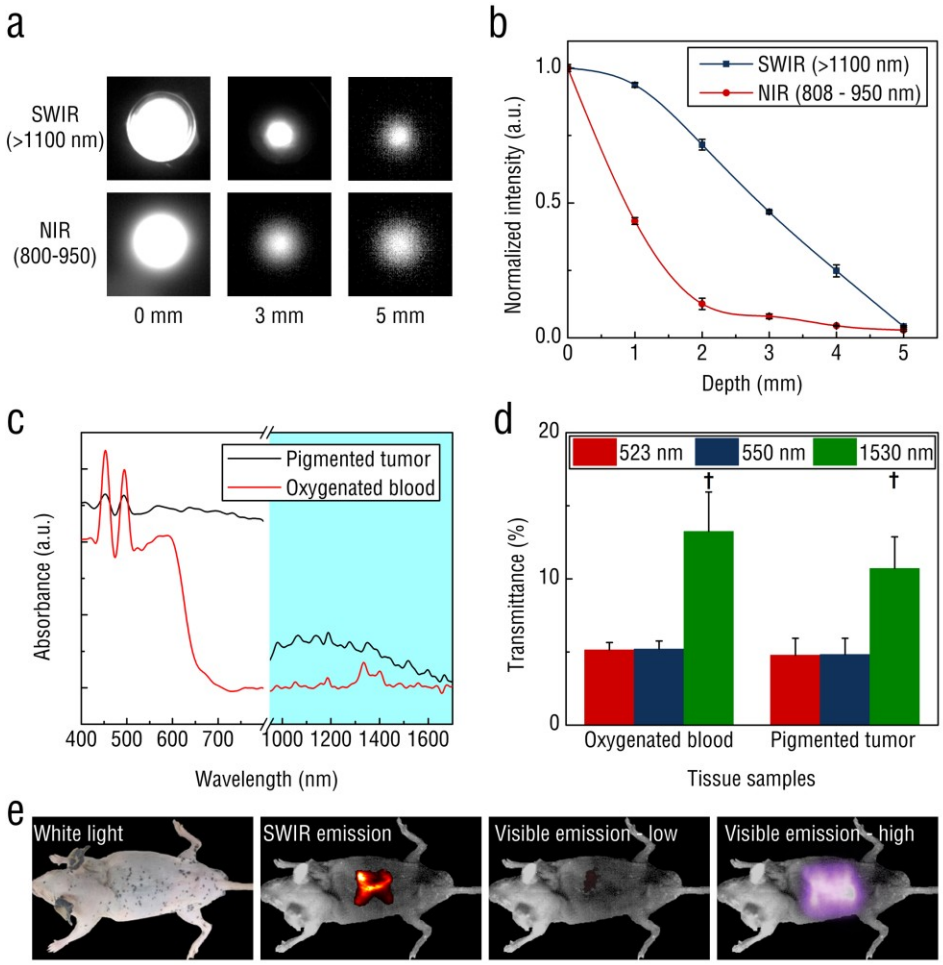

Figure 3.2 – Tissue Transmission of SWIR Compared to NIR and Visible Light. Tissue phantom studies reveal that NIR light (800-950) generated from an 808 nm excitation diode is more greatly scattered than SWIR light (>1100 nm) emitting from a pellet of RE(Er)s after 980 nm excitation as captured by an Indium Gallium Arsenide (InGaAs) infrared camera (a). Using the camera software, NIR transmission intensity is significantly attenuated through 2 mm of phantom tissue, whereas SWIR light is able to effectively transmit through 4 mm of tissue before similar attenuation is observed (b). Transmission spectra of two key absorbers, blood and melanin, were acquired through the visible and SWIR range (c). The absorbance of the melanin present in melanomas

exhibits a minimum beyond 900 nm in the SWIR (blue region), while blood shows an absorbance minimum beyond 700 nm. Note the break in the spectra from 800 to 900 nm is due to the spectrometer's detector change. SWIR transmission (1525 nm) through blood and tumor samples is approximately 3- and 2-folds greater, respectively, than compared to RE(Er) emissions in the visible (523 and 550 nm) (d). RE(Er)s were patterned into the shape of an "R," placed beneath a mouse with resected intestines and irradiated with 980 nm light (0.14 W cm^{-2}) (e) SWIR emission easily distinguished the "R" shape while RE(Er) visible emission was attenuated by the mouse (visible emission – low). Incident power was raised ~4 folds to ~0.5 W cm^{-2} (visible emission – high) and although emission was detected, the pronounced scattering of visible light significantly distorted the "R" shape. Mean values ± s.e.m.; n=3 (†$P < 0.01$) determined by Student's *t*-test.

To evaluate the disease tracking capabilities of SWIR, RE(Er)s were intravenously injected into nude mice with developed melanoma xenografts. During imaging, irregular branching patterns from SWIR emission were seen near tumors (**Fig. 3.4c**). Intraoperative images revealed the abnormal pattern of SWIR emission corresponding to the surrounding tumor vasculature stemming from a large feeder vessel lining the inner skin over the chest and abdomen.

To highlight the potential use of multispectral SWIR imaging, REs emitting at two independent wavelengths were injected into the tumor sites of nude mice with xenograft C8161 human melanomas. Er- and Ho-doped REs were detected in separate

tumors following NIR excitation at distinct SWIR emissions (1525 and 1185 nm, respectively) by adjusting the filters on the SWIR imaging system (**Fig. 3.4d**). Notably, the distinct SWIR emissions could be isolated with filters during full-body irradiation of the animal with a single NIR light source.

3.4. Discussion

The development of probes which permit deeper tissue imaging is critical for the translation of optical imaging for clinical applications. Fluorophores emitting in the SWIR have been reported to exhibit greatly enhanced signal-to-noise ratios compared to their counterparts in the NIR,[72] opening the possibility of a new, second window for biomedical imaging. However, a lack of multispectral SWIR probes has prevented the use of SWIR for in vivo imaging.[257] To address this challenge, we have formulated a library of rare-earth doped nanoparticles (REs) that have tunable and discrete emissions spanning the entire SWIR window. Furthermore, we have characterized and tested REs for in vivo applications.

REs consisting of a $NaYF_4$ rare-earth doped core and $NaYF_4$ undoped shell were synthesized and characterized physically, chemically and optically. These nanoparticles displayed uniform size and morphology distributions, shown by TEM (**Fig. 3.1b**). The crystalline structure of the $NaYF_4$ host, which has been shown to play an important role in determining fluorescence efficiency, was determined by XRD measurements to be predominately hexagonal (**Fig. 3.1c**). Hexagonal phase $NaYF_4$ hosts have been shown to exhibit up to an order of magnitude greater fluorescence efficiencies compared to cubic phase versions.[135] Fabricating highly efficient SWIR-emitting probes is critical for extension and applications in biomedical imaging.

By changing the lanthanide dopant used in the RE core, discrete spectral emissions were produced across the SWIR region using a single NIR (980 nm) excitation source. Altogether, four distinguishable spectral patterns were produced using erbium, holmium, thulium and praseodymium dopant schemes. SWNTs, which have gained

attention for emitting in the SWIR, exhibit much broader emissions spanning over 100 nm and exhibit optimal excitation near 650 nm outside the NIR transparent window.[243,244] The ability to tune the SWIR emissions of REs opens the possibility for multispectral imaging and, with appropriate targeting approaches, molecular imaging using excitation and emission wavelengths that are both in a tissue transparent spectral region.

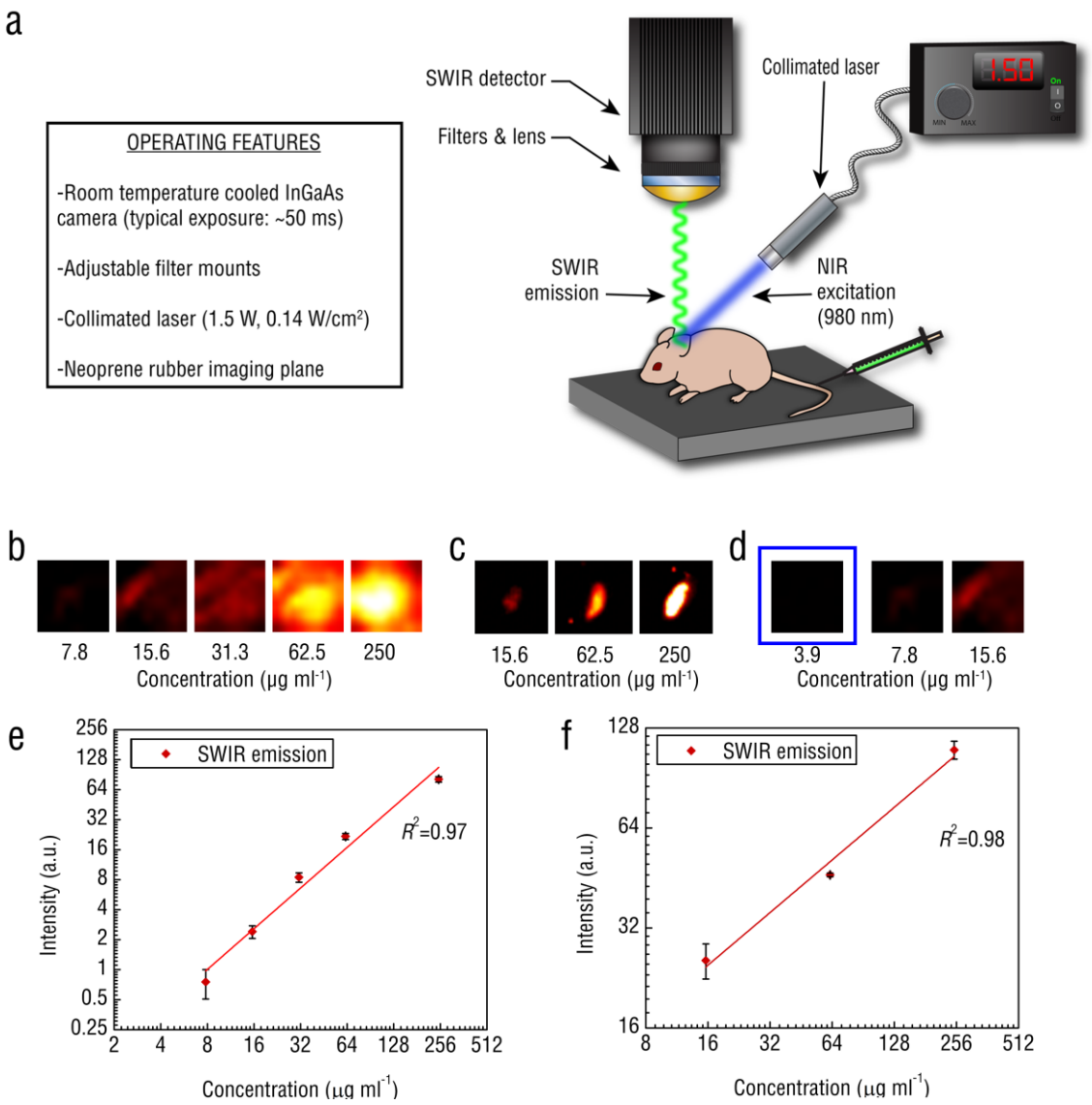

Figure 3.3 – Illustration of SWIR-Imaging Prototype and Detection Capabilities. Schematic of a portable SWIR-imaging prototype consisting of a fiber-coupled, collimated NIR laser photodiode operating at 0.14 W/cm^2 (1.5 W) and a room temperature-cooled Indium Gallium Arsenide (InGaAs) SWIR camera (a). During the imaging, the excitation fiber is held at an arbitrary distance above the animal and slowly scanned across the body, enabling real time capture of SWIR emission. The distance of the fiber above the animal is held within the limits where the incident beam remains collimated. REs were embedded in a 1% agarose phantom and imaged over several serial dilutions by a SWIR camera resulting in a linear (R^2=0.97) SWIR signal (b,e). REs were also mixed with Matrigel and injected subcutaneously into nude mice (c,f). Imaging likewise revealed a linear relationship (R^2=0.98) between SWIR signal and RE concentration. The detection threshold by the SWIR camera was determined at 3.9 μg ml^{-1} (blue box) in the agarose phantom (d). Mean values ± s.e.m.; n = 5.

Next, we compared the performance of SWIR emission from RE(Er)s to both visible and NIR light in phantom and animal-derived tissue samples. Using phantom tissue composed of agarose and Intralipid, a well-characterized scattering medium, we determined that SWIR at 1525 nm is scattered less and penetrates deeper than NIR at ~800 nm. Qualitatively, NIR light was observed to broaden further with increasing phantom depth, likely due to wavelength-dependent scattering caused by the Intralipid.[258] The scattering observed with NIR can lead to information loss during imaging,[239] resulting in poorer resolution and greater difficulty in distinguishing signal source

features. Indeed, this was made evident when RE(Er)s were patterned into a defined shape and placed underneath a mouse carcass (**Fig 3.2e**). While the visible upconversion fluorescence was either attenuated with low power excitation or highly scattered and blurred with high power excitation, SWIR emissions could penetrate through the animal while retaining accurate optical information regarding the structure and position of the shape. Furthermore, we observed enhanced SWIR transmission compared to visible light through tissue absorbers including blood and melanin. Taken together, these results highlight the promise of SWIR derived from REs for biomedical imaging purposes.

SWIR-based imaging requires a simple set-up that can be rapidly implemented in a preclinical or clinical environment. We designed a basic imaging platform consisting of an indium gallium arsenide (InGaAs) camera for video-rate SWIR detection, low power NIR photodiode for RE excitation and image post-processing software. Compared to another similarly functioning system that has been reported in the literature which uses a 5-8 W pulsed NIR source and liquid nitrogen cooled InGaAs camera with exposure times in the hundreds of milliseconds,[239,243,244] our prototype operates at significantly lower excitation power (~1.4 W) and detector sensitivity. Furthermore, our imaging set-up is inexpensive, removing one potential barrier to widespread preclinical and clinical implementation.

Finally, we explored the potential of REs as contrast agents for several important biomedical imaging applications: 1) real-time probe detection, 2) anatomical discrimination, and 3) multi-spectral signal resolution. Following injection via the tail vein, RE(Er)s were observed throughout the vasculature network and tracked through individual organs such as the lungs and heart before accumulating in the liver and spleen.

Transient SWIR emissions were observed in both the lungs and heart, confirming the circulation and whole-body distribution of the nanoparticles. Strikingly, video imaging clearly revealed pulsing SWIR emissions in the animal's chest, likely due to the movement of RE(Er)s through the beating heart and active lungs. Over the course of imaging, SWIR emission intensity progressively increased in both the liver and spleen, organs part of the reticuloendothelial system (RES) that mediate nanoparticle clearance. Although SWIR emission was briefly seen in the kidneys, this was likely due to first pass circulation and not renal clearance. The imaging study strongly suggests that the RE(Er)s are removed from circulation primarily through RES filtration. Importantly, both the real-time circulation and spatio-temporal distribution of RE(Er)s in individual organs could be distinguished. This provides a means for rapidly evaluating nanoparticle biodistribution in real-time within deep tissue using SWIR. Notably, in all locations where SWIR emission was observed in the mice, the upconversion fluorescence signal of the REs was absent, likely due to absorption and scattering losses caused by blood and tissue components.

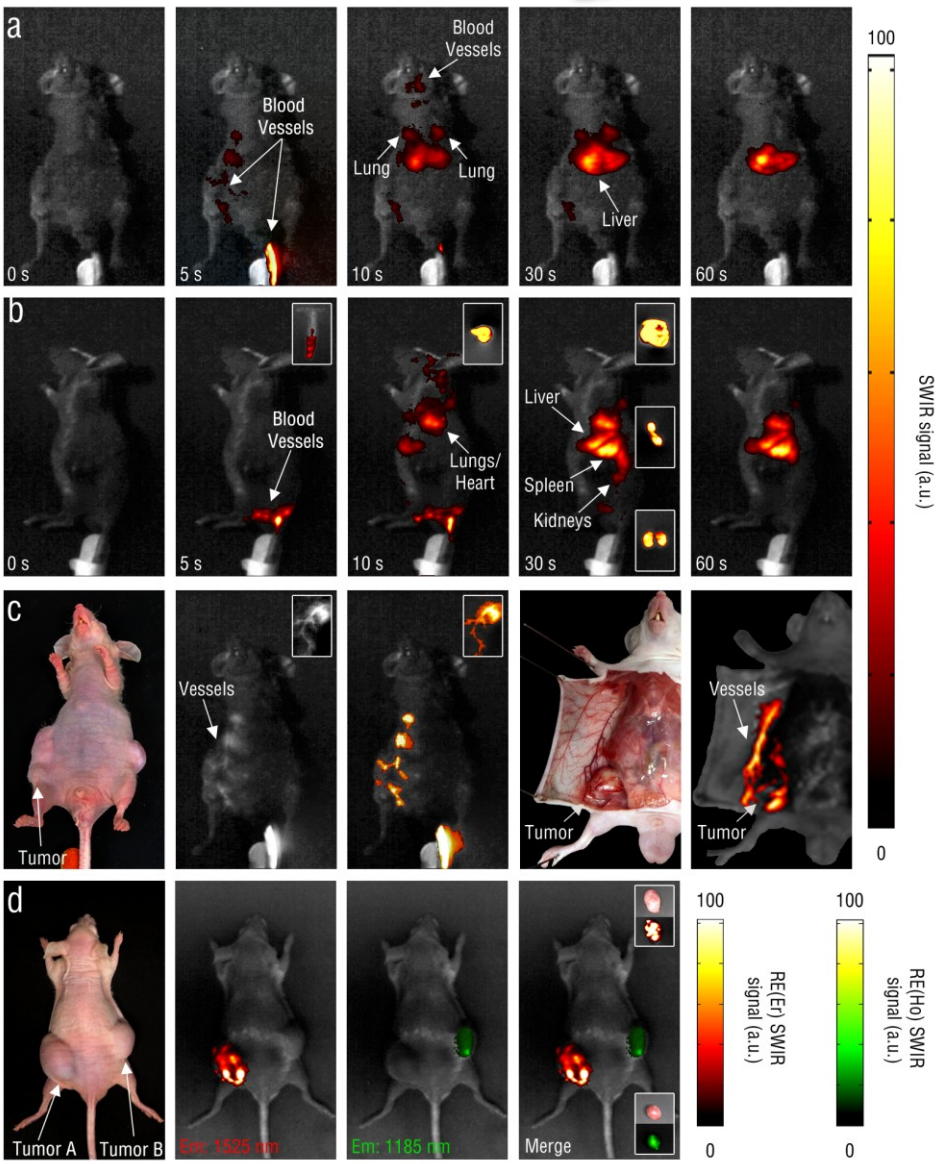

Figure 3.4 – Proof-of-Concept In vivo SWIR Imaging. Video-rate biodistribution of intravenously injected RE(Er) was captured in hairless mice using the imaging system prototype from both the ventral (a) and left lateral (b) views. SWIR emission was initially detected in the vasculature of the tail and branching through the abdomen (5 s) before progressing through the lungs (10 s), liver (30 s) and spleen (30 s) over the course of 60 seconds. RE(Er)s were transiently seen in the kidneys (c, 30 s). Insets (b) show excised

organs including sampled blood (5 s), lungs (10 s), liver (30 s, top) spleen (30 s, middle) and kidneys (30 s, bottom) taken from replicate mice sacrificed as closely as possible to each time point. The high-resolution capabilities of the imaging system and enhanced transmission of SWIR through blood was examined in nude mice bearing melanoma xenografts. Mice were injected with RE(Er) intravenously and imaged over time. Irregular, branching emission patterns were observed near tumor regions that were associated with surrounding vasculature upon dissection (c). Proof-of-concept multiplexed SWIR imaging was performed with the RE(Er) and RE(Ho) in nude mice with developed melanoma xenografts (d). Filter sets were adjusted to capture only the 1525 nm emission of the RE(Er) and subsequently changed to capture the 1185 nm emission of the RE(Ho). Tumors were excised and confirmed to show the localized SWIR signal. Representative images (n=3) are shown in all instances.

To highlight the enhanced blood transmission of SWIR, tumor-burdened mice were injected with RE(Er)s and imaged in real-time. Aberrant vascular patterns were observed near tumor xenografts during whole body imaging which corresponded to tumor vasculature during intraoperative imaging (**Fig. 3.4c**). The SWIR emissions from RE(Er)-rich blood appeared to distribute through the tumor, possibly indicating passive targeting of the REs. Both the feeder vessel and individual angiogenic blood vessels lining the tumor were easily resolved without any further modifications to the imaging system, unlike earlier reports of vascular imaging using SWNTs.[243] These results highlight the clinical potential of SWIR to identify and monitor pathological states such

as tumor angiogenesis or cardiovascular lesions, current challenges for many imaging modalities.[259,260]

Finally, our studies provide, to the best of our knowledge, the first successful demonstration of multispectral SWIR imaging in vivo. Using a single, low power excitation source in the NIR, separate SWIR signals could be identified from REs injected into different tumors. Our current system and probe library therefore has the potential to image up to four distinct SWIR signals in vivo simultaneously. Combined with molecular targeting approaches, multispectral REs have the potential to open a new field of molecular imaging with superior SWIR optical properties.

3.5. Conclusion

In this work, we have reported on the first evidence of multi-spectral, real-time SWIR in vivo imaging using rare earth nanoprobes and demonstrated the improvements that can be made with the current standards of optical imaging using SWIR light. Our work has determined that utilizing SWIR light for in vivo imaging affords both qualitative and quantitative benefits over conventional imaging approaches that rely on NIR or visible light. Furthermore, we have provided details regarding the design of a cost-effective SWIR imaging system that can be readily applied in both a pre-clinical and clinical setting. We envision use of this platform imaging technology in a wide variety of biomedical applications including deep tissue imaging, real-time nanoparticle tracking and multispectral molecular imaging.

3.6. Supplementary Figures

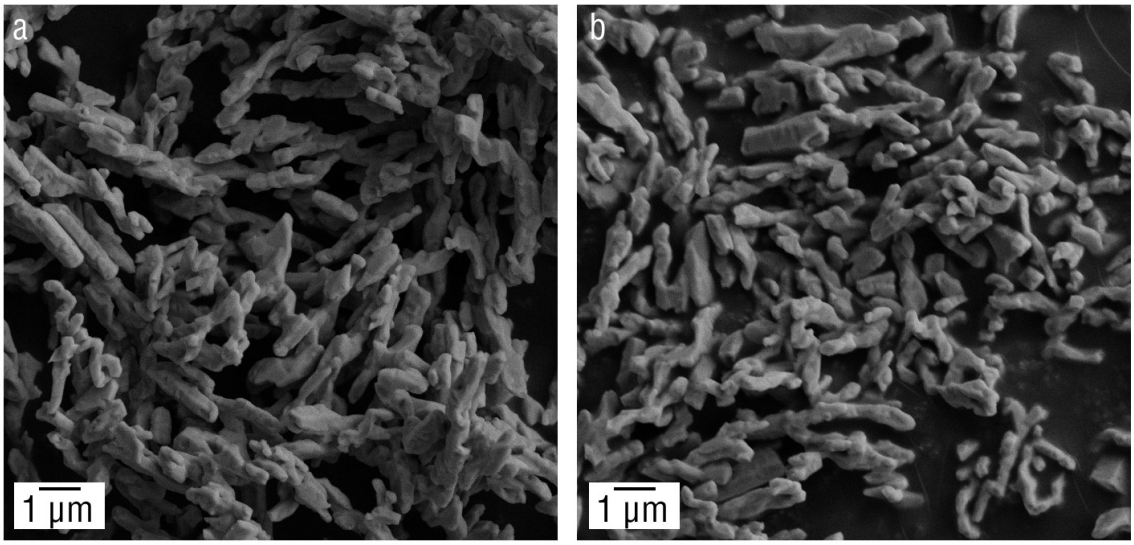

Supplementary Figure S3.1 – SEM Micrographs of Micron Sized REs. Micron-sized RE(Er) (a) and RE(Ho) (b) particles exhibit distinct rod-like morphology as seen under SEM.

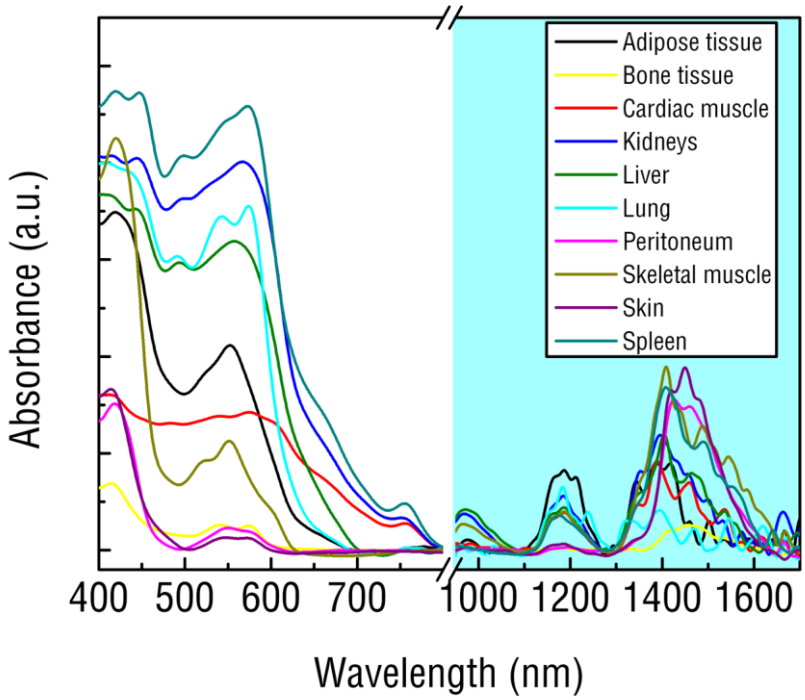

Supplementary Figure S3.2 – Absorbance SWIR Through Various Tissue Samples. Absorbance spectra of various tissue components spanning from 400 to 1700 nm reveals a distinct region between 900-1300 and 1500-1700 nm exhibiting very low tissue absorbance, confirming earlier reports of a second window of biological transparency (a). Note the break in the spectra from 800 to 900 nm is due to the spectroscope detector change.

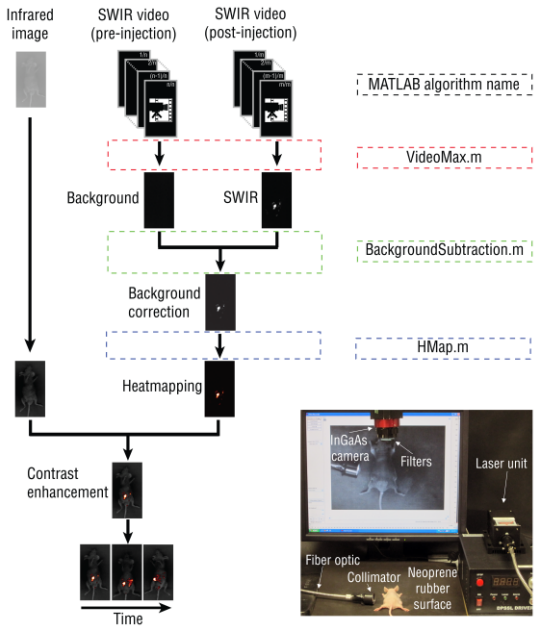

Supplementary Figure S3.3 – Image Processing Workflow. The SWIR video files obtained from our imaging system (bottom right corner) were processed using a series of MATLAB algorithms to generate a background-corrected heatmap of fluorescence distribution in the animal. Two sets of videos were captured for each animal: pre- and post-nanoparticle injection scans. These videos were processed using the VideoMax.m algorithm, which generates a single image composed of the highest intensity pixels of SWIR fluorescence. The BackgroundSubtraction.m algorithm is then applied to subtract any background SWIR fluorescence from the post-injection images. The HMap.m algorithm is used on the background-corrected images to apply a color heatmap of fluorescence. In parallel, single-frame SWIR images of the mice were captured under ambient light conditions. The contrast of these images was enhanced and merged with the appropriate heatmaps to generate the final images.

CHAPTER 4

INVESTIGATION OF BIOACTIVE FORMULATIONS OF RARE-EARTH DOPED NANOPARTICLES IN ENCAPSULATED ALBUMIN NANOCARRIERS FOR TUMOR IMAGING

Sections of this chapter are currently being prepared for publication elsewhere as part of an article entitled:

"Rare-earth doped nanoparticles as bioactive probes for shortwave infrared in vivo imaging"

D.J. Naczynski, M.C. Tan, M. Zevon, B. Wall, J. Kohl, A. Kulesa, S. Chen, C.M. Roth, R.E. Riman, P.V. Moghe

Abstract

The availability of exogenous optical contrast agents that can be resolved sensitively within deep tissues and targeted to specific disease states is critical for the effective and widespread clinical translation of optical imaging. Short wavelength infrared (SWIR) detectable agents were recently reported to offer significant advantages over traditional near infrared (NIR) probes for in vivo optical imaging. This chapter focuses on disease targeting SWIR imaging using inorganic-organic nanocomposite formulations of the rare earth contrast probes developed in the previous chapter. Human serum albumin was used to encapsulate rare earth doped nanoparticles (RE(Er)s), forming SWIR-emitting nanocomposites of tunable hydrodynamic diameters. The presence of albumin, as well as the thickness of encapsulation, strongly influenced the pharmacokinetic profile of RE(Er)s and prolonged the nanocomposite circulation in vivo. Importantly, albumin encapsulation increased the amount of RE(Er)s delivered by greater than 10-fold compared to uncoated RE(Er)s in metastatic tumors generated de novo in a murine transgenic melanoma model. Additionally, nanoparticles were readily imaged through dense, pigmented tumor using SWIR detection, and successfully resolved at specific organs in a spatio-temporal manner. Our results demonstrate the effect of a bioactive albumin coating on inorganic nanoparticles and its effect on biodistribution and disease targeting ability.

4.1. Introduction

Optical imaging offers a range of unique features that complement the biological information gained from current clinical imaging modalities such as computed tomography (CT), magnetic resonance imaging (MRI) and positron emission tomography (PET).[33,35,51,58,261] Optical imaging offers the safety of non-ionizing radiation with the convenience of simple, cost-effective imaging systems that can be readily implemented within a clinical setting.[262] Fundamentally, optical imaging is governed by the interaction of photons with biological tissues. The greatest challenge for implementing optical imaging for clinical applications is the limited depth of tissue through which light can penetrate.[72]

The total attenuation of photons through biological tissues is a sum of the losses sustained by both light absorption and scattering.[72] The discovery that light in the near infrared range (NIR 700-1000 nm) is absorbed by tissue components to a lesser extent than visible light has led to the development of numerous NIR imaging approaches in this first "tissue transparent window."[31] Light scattering is a complex phenomenon wherein a photon deviates from the parallel axis of its path.[72] In addition to reducing penetration depth, scattering can also lead to a reduction of structure resolution within a biological environment.[239] It has been reported that light in the short wavelength infrared range (SWIR 1000-2000 nm) exhibits significant reductions in scatter losses compared to NIR and has comparably low absorption characteristics.[72] The development of materials or contrast agents that can exploit the benefits of SWIR would therefore accelerate the development of a potentially disruptive clinical imaging platform.

Contrast agents provide a means of detecting changes in native surroundings during imaging. With proper design, contrast agents can target and visualize specific biological features or events, such as specific molecular receptors or disease progression.[74] While there are numerous contrast agents that can be visualized with low-absorbing NIR, few materials can effectively exploit the benefits of SWIR for biological imaging.[257] Currently available materials, such as single-walled carbon nanotubes and SWIR-emitting quantum dots QDs, lack the physical tunability for controlled in vivo pharmacokinetics or the safety for widespread clinical use.[257] Recently, a new class of nanoparticles, composed of $NaYF_4$ doped with ytterbium (Yb) and erbium (Er) (RE(Er)s), has been shown to efficiently generate intense SWIR emissions.[141] However, poor aqueous solubility, lack of functional groups and moderate cytotoxicity preclude the use of RE(Er)s as synthesized for biological applications.[128]

Our previous work has shown that the encapsulation of RE(Er)s in human serum albumin (HSA) yields a significant reduction of RE(Er) toxicity, an aqueous-dispersible encapsulate, and surface groups capable of chemical conjugation for the purpose of disease targeting.[128] HSA is known to exhibit distinct preferential affinity for tumor associated molecules when incorporated into a nanoparticle form, offering a unique opportunity for the delivery of contrast agents such as RE(Er)s. Current FDA-approved HSA nanoparticles, for example, have been shown to improve the circulation time of bound therapeutics[263] and are thought to interact with molecular targets resulting in improved drug delivery and lengthened particle retention at tumor sites.[264,265]

In the studies described within this chapter, RE(Er)s were encapsulated in HSA to form rare-earth albumin nanocomposites ((RE)ANCs) and evaluated for in vivo tumor

targeting. Through the size controlled HSA encapsulation of RE(Er)s, the importance of both nanoparticle size and surface properties for the enhanced delivery of RE(Er)s into tumor tissue was investigated. Our results show that the albumin-mediated bioactivity of (RE)ANCs strongly influences the pharmacokinetic profile of RE(Er)s, promoting increased circulation and more widespread, rapid biodistribution. Furthermore, we observed significantly greater accumulation of smaller (RE)ANCs in tumors exhibited by transgenic mice when compared to non-encapsulated RE(Er)s or larger (RE)ANCs. Taken together, our results indicate that significant improvements in both the pharmacokinetics and tumor targeting potential of RE(Er)s can be achieved by the controlled encapsulation by HSA.

4.2. Methods

4.2.1. Synthesis of REs

$NaYF_4$:Yb,Er nanoparticles (RE(Er)s) were prepared using solvothermal decomposition of rare earth trifluoroacetate precursors in oleylamine as described previously[128]. Briefly, a core precursor solution was prepared by dissolving stoichiometric amounts of 99.9% erbium trifluoroacetate, 99.9% yttrium trifluoroacetate, 99.9% ytterbium trifluoroacetate (GFS Chemicals, Columbus, OH) and 98% sodium trifluoroacetate (Sigma Aldrich, St. Louis, Missouri) in oleylamine. The shell solution was prepared by dissolving stoichiometric amounts of the sodium and yttrium trifluoroacetates in oleylamine. The core solution was then heated to 340°C under vigorous stirring in an inert argon atmosphere to allow the formation of the core particles. The shell precursor was then added and after cooling, the synthesized nanoparticles were washed three times in ethanol by centrifuging at 15,000×g (Beckman Coulter Inc., Avanti J-26 XP, Fullerton, CA) and freeze-dried at -40°C (SP Industries Inc., VirTis AdVantage Plus Warminster, PA).

4.2.2. Physical and Optical Characterization of RE(Er)s

RE(Er)s were both physically characterized using transmission electron microscopy (TEM) and optical spectroscopy.

Particles were visualized by using a TEM instrument (JEOL 2010F, Tokyo, Japan) operated at 200 kV. After synthesis, RE(Er)s were washed with an ethanol/methanol solution and resuspended in toluene, sonicated and deposited on a 400-mesh Formvar-backed carbon-coated copper grid (EMS, Hatfield, PA). Solutions were

dried in an oven at 60°C before imaging. To determine the average size of RE(Er)s, approximately 100 particles were measured from acquired TEM images.

The emission spectra of powdered RE(Er)s held in a 0.5 cm path length cell were recorded following excitation using a 2.5 W 975 nm photodiode (model BWF-OEM 975, BW Tek, Newark, NJ). The emission from the sample was collected using a FSP920 Edinburgh Instruments spectrometer (Edinburgh Instruments, Livingston, United Kingdom) that was equipped with a Hamamatsu G5852-23 thermoelectrically cooled shortwave infrared sensitive InGaAs photodiode.

4.2.3. (RE)ANC Synthesis and Characterization

(RE)ANCs were prepared through the modification of an established controlled coacervation technique as described previously.[128] Briefly, a 2% (w/v) solution of HSA in NaCl at pH 8.50 +/- 0.05 was prepared and adjusted with 0.1 M NaOH. The concentration of NaCl was varied between 2 mM and 12 mM to change the thickness of the albumin nanocomposite coating. Under continuous stirring at 700 rpm and room temperature, ethanol (2 mL) sonicated with RE(Er) nanoparticles (0.2 mg mL^{-1}) was added with a syringe pump (Harvard Apparatus PHD 2000, Holliston, MA) at 1.5 mL min^{-1} to the HSA solution (500 mL). Immediately following ethanol addition, glutaraldehyde solution (0.24 μL mg^{-1} HSA) was added to stabilize and crosslink the nanoparticle suspension. The particles were left to crosslink overnight under stirring at room temperature.

(RE)ANC were purified by three rounds of centrifugation at 8,000xg and 48,400xg for 2 mM NaCl formed nanoparticles for 8 min at 4°C (Beckman Coulter,

Avanti J-E Centrifuge) for (RE)ANCs formed under 12 mM and 2 mM NaCl conditions, respectively. Following centrifugation, nanoparticles were washed and redispersed with PBS. The last redispersion step concentrated the nanoparticles to x10 with PBS. Redispersion was performed in an ultrasonication bath (Fisher Scientific, FS60) for 15 min.

Hydrodynamic size distributions, polydispersity indices, and zeta potential calculations were determined for (RE)ANCs using a Malvern Zetasizer Nano (Zen 3690, Malvern, Worcestershire, UK). Samples were diluted 1:50 in deionized water for z-average size, or intensity mean, and polydispersity measurements and diluted 1:50 in PBS (pH 7.4) for zeta potential calculations. Z-average sizes and polydispersity indices of three sequential sample scans (3 runs $scan^{-1}$, 60 s $scan^{-1}$) were measured at a 90° scattering angle at 37°C. Z-average potential calculations were also performed over three sequential sample scans (20 runs $scan^{-1}$, 10 s $scan^{-1}$) using the Smoluchowski model. At least four separate batches of particles were measured and averaged in this manner for all tested parameters.

For determination of particle protein content, samples were diluted 1:5 in PBS and assayed by bicinchoninic acid (BCA; Pierce Chemical Co., Rockford, IL) using known quantities of bovine serum albumin as a standard.

(RE)ANCs were visualized using an SEM instrument (Carl Zeiss Σigma) operated at an accelerating voltage of 5.0 kV with working distance of 10 mm. After synthesis, (RE)ANCs were lyophilized and the resulting powder was deposited on an aluminum sample holder coated with double-sided carbon tape. A layer of Au was sputtered on top of the dried film with a Balzers SCD 004 Sputter Coating Unit (Balzers, Liechtenstein).

Images were captured using the secondary electron detector. For lyophilized size measurements, approximately 100 individual (RE)ANCs were measured and sizes averaged from SEM images.

4.2.4. Animal Models

Biodistribution and tumor accumulation studies were performed using transgenic mice that are predisposed to develop multiple melanomas (TG-3). The TG-3 mice were developed by Dr. Suzie Chen as described previously.[256] Pigmented tumors on distant organs are observed by 3-4 months after birth and tumor progression closely mimics the growth and metastasis patterns of clinical human melanoma.[256] Hairless versions of the TG-3 animal, TGS, were developed for ease of tumor visualization and were used in this study. Animals were inspected for tumor development twice weekly. Animals that had adequate tumor development were used for imaging and biodistribution studies.

All animal studies were approved by the Institutional Review Board for the Animal Care and Facilities Committee of Rutgers University and performed in accordance with institutional guidelines on animal handling.

4.2.5. Imaging Prototype and Post-Processing

A prototype of a small animal SWIR-imaging system was utilized to investigate the photonic behaviors of the nanocomposites using noninvasive fluorescence imaging. The in-house SWIR-imaging prototype consists of fiber-coupled NIR laser photodiode which operates at 980 nm and 1.4-1.5 W, and an InGaAs camera (Goodrich, Princeton, NJ) positioned approximately 12 in above the imaging surface. A collimator with a NA =

0.25 and f = 37 mm (Thor Labs, Newton, NJ) was attached to the excitation fiber to enable a uniform and constant excitation beam radius which is independent of the distance between source and animal subject. Based on the power output and collimation, the animal was irradiated with approximately 0.13-0.14 W cm^{-2} of 980 nm light. During the imaging, the excitation fiber was held at an arbitrary distance above the animal and slowly scanned across the animal's body. The distance of the fiber above the animal was held within 12 in of the animal, within the limits where the incident beam remains collimated. Any SWIR emissions were then simultaneously captured in real time by the SWIR camera that was positioned in a fixed height above the animal. Videos were captured at 19-22 frames per second (i.e. detection exposure time 45-53 msec). Optical filters were fitted, as described earlier, onto the SWIR camera to eliminate detection of the NIR excitation source to confidently determine that only the SWIR emissions were captured. An incandescent Xe flashlight (Mini Maglite AA-Cell Flashlight, Maglite, Ontario, CA) was also to provide backlight to partially resolve the location of the mouse. Finally, black Neoprene rubber or a latex-paint-coated cardboard was used as the background surface on which the mouse was placed to reduce the amount of ambient reflected light and produce a favorable signal-to-noise ratio. Acquired SWIR video files were processed using a series of MATLAB codes to generate a background-corrected heatmap of fluorescence distribution in the animal.

In order to quantify fluorescence, ImagePro was used to select areas of fluorescence and report the average intensity of all selected pixels. For each image, the average intensities of fluorescent regions of interest (ROI) was measured, and the average intensity of the non-fluorescent background was subtracted from each value.

4.2.6. Qualitative Imaging of Biodistribution

TGS mice were fully anesthetized with an intraperitoneal injection Avertin 240 mg/kg prior to imaging. Mice were scanned with the collimated 980 nm laser prior to nanocomposite injection in order to establish a baseline for autofluorescence (background image). Mice were then injected with 10 mg RE(Er) nanoparticles kg^{-1} of either 1) uncoated, 2) 2mM (RE)ANCs or 3) 12mM (RE)ANCs via intraperitoneal injection (IP). Approximately 15 minutes, 12, 24, 48 and 72 h post-injection, mice were irradiated with the collimated 980 nm laser in supine, prone and both left and right lateral positions under anesthesia.

4.2.7. Quantitative Biodistribution Analysis

Mice exhibiting vascularized melanoma tumors were injected with 100 μL of the 0.5 mg RE(Er) nanoparticles ml^{-1} in PBS. At 12, 24, 48 and 72 hours the mice were euthanized and their organs were collected. The organs were rinsed with PBS and weighed, then stored at -80°C until digestion. Tissue samples were digested in 16 M nitric acid (Fisher Scientific, Waltham, MA) and evaporated, then reconstituted in 10% nitric acid to account for differences in sample volume. In detail, excised organs were placed in Teflon vials and 5 mL of 16 M HNO_3 was added. The organs were heated to 200°F and allowed to digest. The vials were allowed to reflux with the lids on for 30 minutes. The acid was then evaporated down and brought back to a final volume of 5 ml in 10% HNO_3 diluted with ultrapure water. The yttrium content of the digested organs

was quantified using a Thermo X Series II ICP-MS (Thermo scientific) to determine the total amount of yttrium in the organ, and therefore the concentration of particles.

4.3. Results

4.3.1. Synthesis and Characterization of (RE)ANCs

RE(Er)s were surface modified with HSA, forming rare-earth albumin nanocomposites ((RE)ANCs) by solvent-induced controlled coacervation of albumin (**Fig. 4.1a**). By varying the amount of sodium chloride in the HSA solution prior to coacervation, the size of the final nanoparticles could be controlled. Two sets of (RE)ANC particle sizes were synthesized: 100 nm (small) and 280 nm (large) hydrodynamic diameters. (RE)ANCs of all sizes retained the unique SWIR (**Fig. 4.1b**) and upconversion emission (**Supplementary Fig. S4.1**) spectra of the coated REs after albumin encapsulation. SEM imaging revealed spherical, monodisperse nanoparticles with lyophilized diameters of ~50 nm for small (RE)ANCs (**Fig. 4.1c**) and ~100 nm for large (RE)ANCs (**Fig. 4.1d**). Both sets of particles had low polydispersity in aqueous solution and comparable amounts of RE(Er) and HSA content (**Fig. 4.1e**). In addition, both particles exhibit negative zeta potentials in PBS (**Fig. 4.1e**).

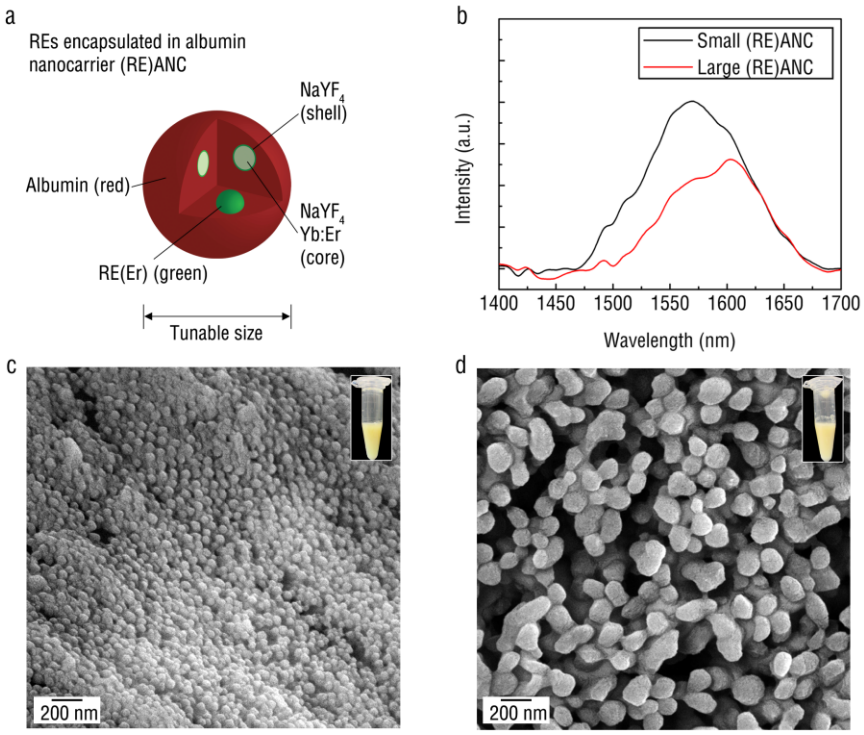

e

(RE)ANC Type	Lyophilized diameter (nm)	Hydrodynamic diameter (nm)	Polydispersity index	Zeta potential (mv)	RE content (μg ml^{-1})	Protein content (μg ml^{-1})
Small	46 ± 6	100 ± 5	0.12 ± 0.05	-13 ± 0.6	485 ± 65	3200 ± 50
Large	100 ± 15	280 ± 9	0.12 ± 0.03	-13 ± 1.0	510 ± 40	3590 ± 90

Figure 4.1 – Physical and Optical Properties of (RE)ANCs. RE(ANC)s consist of REs encapsulated by a coating of HSA, which can be tuned in size. (a). Both small and large (RE)ANCs retain the SWIR emission of the encapsulated REs, exhibiting peak emission between 1550-1600 nm following 980 nm excitation (b). SEM images of both small (c) and large (d) (RE)ANCs show uniform sub-100 nm spherical particles. From the SEM images, small and large lyophilized (RE)ANCs exhibit an average size of 46 nm and 100 nm which appears to swell when hydrated to 100 and 280 nm, respectively. DLS measurements confirm a low polydispersity and heterogeneity of size. Furthermore, both formulations show negative zeta potentials in PBS (pH 7.4), with the HSA content increasing for larger (RE)ANCs (d). Mean values ± s.d.; n=5.

4.3.2. In vivo Pharmacokinetics and Biodistribution of Nanoparticles

RE(Er)s, small (RE)ANCs and large (RE)ANCs ranging across three separate populations of sizes (**Fig. 4.2**) were injected intraperitoneally (i.p.) into TGS mice. Pharmacokinetic data indicate that (RE)ANCs enter into circulation after IP injection more rapidly than uncoated RE(Er)s (**Fig. 4.3a**). Small (RE)ANCs enter into circulation immediately after injection, followed by a secondary peak approximately 1 h after injection. Notably, a third peak in yttrium concentration is seen after 2 h and sustained for over 6 h following injection. Large (RE)ANCs exhibit more traditional biphasic circulation, peaking in concentration approximately 1 h after injection. In contrast, RE(Er)s have significantly delayed biphasic behavior, entering circulation at low concentrations approximately 2 h after injection and quickly removed from the blood. Metabolic studies conducted at 24 h reveal clearance of all 3 formulations predominately in the feces for TGS mice after i.p. injection (**Fig. 4.3b**).

Accumulation was observed predominantly in the two main organs of the reticuloendothelial system (RES), the spleen and liver, as well as in the peritoneum for all nanoparticles tested. Significantly less accumulation was seen in the kidneys, lymph nodes and lungs. Blood, brain and heart displayed negligible yttrium presence (<0.1% ID per gram tissue) at the tested timepoints (**Supplementary Fig. S4.2**).

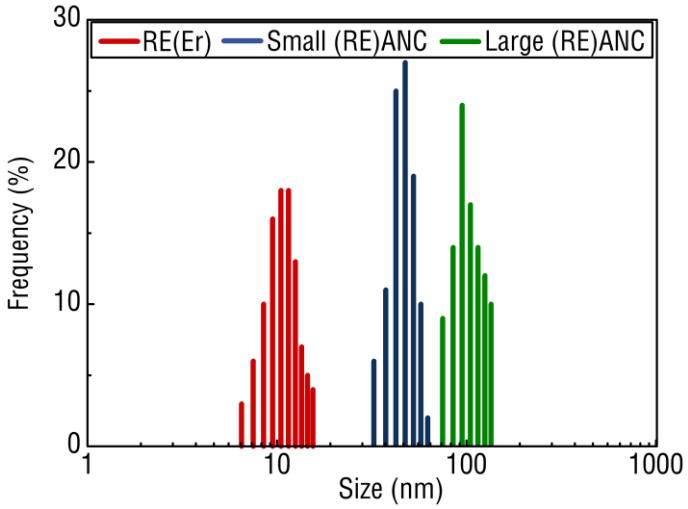

Figure 4.2 – Narrow Size Distribution of Tested Nanoparticle Formulations. Histogram of lyophilized size distributions for RE(Er), small (RE)ANCs and large (RE)ANCs show narrow and distinct populations.

4.3.3. Tumor Accumulation of Nanoparticles in Transgenic Melanoma Mice

Following IP injection of the RE(Er)s, SWIR fluorescence was localized to the abdominal cavity and site of injection of TGS mice even after 76 h (**Fig. 4.4a**). In contrast, the SWIR emission of small and large (RE)ANCs in the peritoneal cavity progressively diminished over time. Long-term studies have indicated that RE(Er)s stay localized in the abdominal cavity over 6 days (**Supplementary Fig. S4.2**). In contrast, SWIR imaging of both large and small (RE)ANCs show widespread fluorescence after injection.

The small (RE)ANCs distributed towards tumor sites located near the ears of the TGS mice beginning at 12 h, with peak accumulation at 24 h and clearance by 72 h (**Fig.**

4.4b). The accumulation and clearance of SWIR fluorescence was described by a polynomial fit for the small and large (RE)ANC formulations (R^2 =0.99 and 0.96, respectively) (**Fig. 4.4c**). ICP-MS was performed to confirm the presence of yttrium and quantify the amount of nanoparticles in the tumors (**Fig. 4.4d**). At 12 h, both small and large (RE)ANCs accumulated approximately 5-fold more than RE(Er), while at 24 h small (RE)ANCs accumulated at tumor sites over 10-fold more than RE(Er) or large (RE)ANCs.

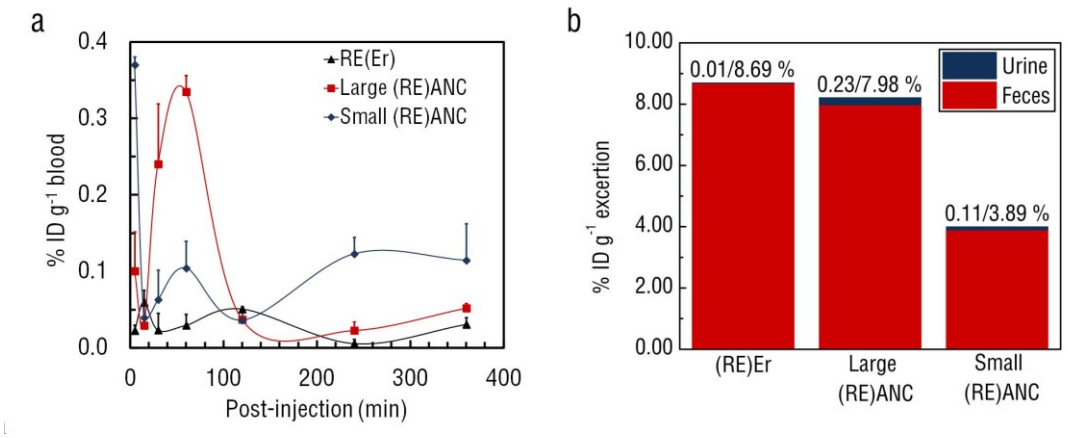

Figure 4.3 – Pharmacokinetics of Formulations. RE(Er)s, large and small (RE)ANCs were injected IP into TGS mice and blood analyzed at 5, 15, 30, 60, 120, 240, 360 minutes post injection. Both albumin formations resulted in spikes of yttrium observed in sampled blood over the first 5 m (for small (RE)ANCs) and ~60 m (for large (RE)ANCs), while RE(Er)s did not readily enter into circulation over the entire timecourse. These results suggest the size and surface characteristics of the small (RE)ANCs facilitate rapid, systemic distribution, while the RE(Er)s remain inert in the peritoneum cavity after injection. Metabolic studies conducted at 24 h reveal predominant clearance of all 3

formulations in the feces for TGS mice after IP injection. Mean values ± s.e.m.; n = 3, animals pooled for metabolic studies.

4.4. Discussion

The emergence of optical contrast agents that can sensitively highlight and selectively target diseased tissue will expand the utilization of optical imaging for clinical applications. SWIR-based imaging affords the benefits of low tissue autofluorescence combined with reduced scattering. It has been reported that imaging in the SWIR can improve signal-to-noise ratios by over 100-fold compared to imaging in the near infrared (NIR).[257] However, the development of non-toxic SWIR-emitting materials whose size can be controlled to modulate pharmacokinetics is currently lacking.[257] To address this unmet need, we have developed a novel class of nanocomposite probes ((RE)ANCs) consisting of SWIR-emitting RE(Er)s encapsulated within tumor-targeting albumin nanoparticles.

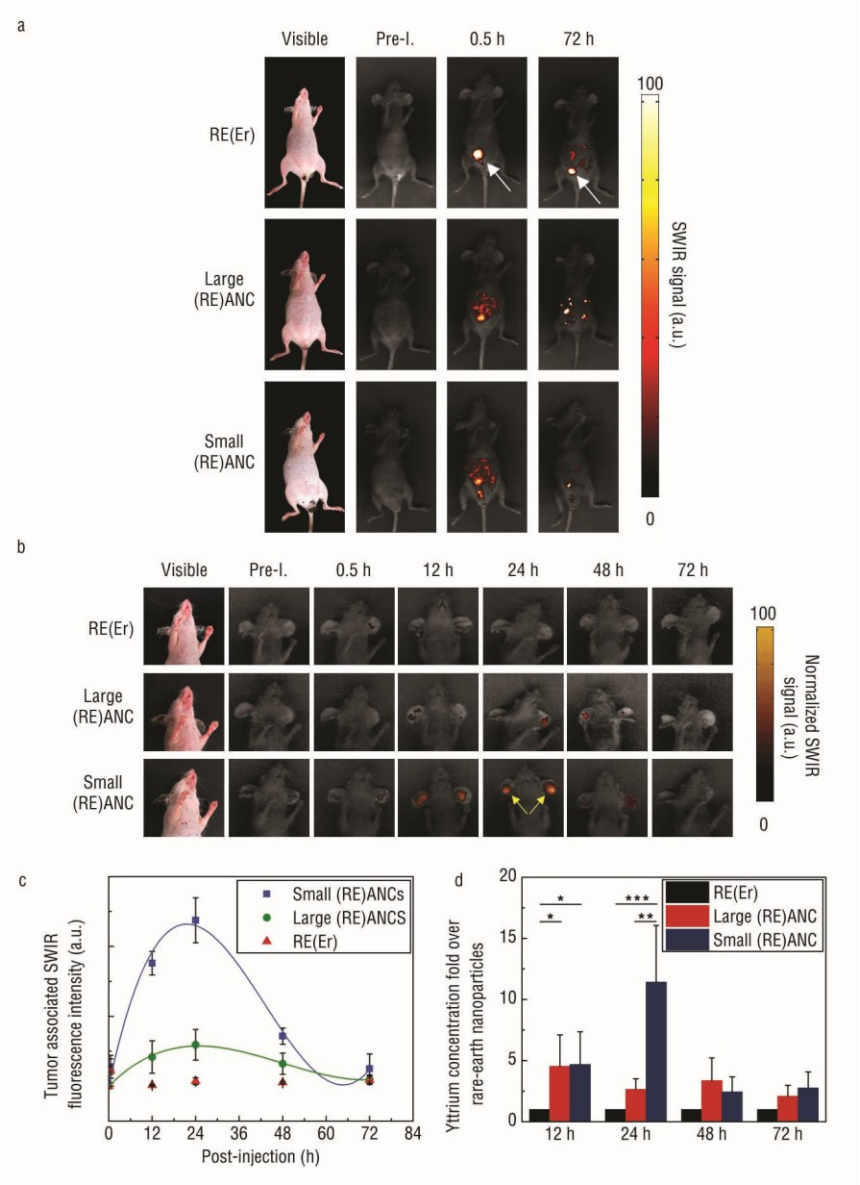

Figure 4.4 – SWIR Images of TG3 Mice IP Injected with RE(Er)s, Small and Large (RE)ANCs. Representative (n=3) images show that following IP injection of the RE(Er), SWIR fluorescence is localized to the abdominal cavity and site of injection of TGS mice even after 76 h (a, white arrows). In contrast, SWIR imaging of both large and small (RE)ANCs show widespread fluorescence after injection indicative of reduced aggregation. The small (RE)ANCs spread towards tumor sites located near the ears of

the TGS mice beginning at 12 h (b), with peak accumulation at 24 h and clearing by 72 h. The accumulation and clearance of SWIR fluorescence was described by a third-order polynomial fit for the small and large (RE)ANC formulations (R^2 =0.99 and 0.96, respectively) (c). Finally, ICP-MS was done to confirm the presence of yttrium and quantify the amount of nanoparticles in the tumors. At 12 h, both small and large (RE)ANCs accumulated approximately 5-fold higher than RE(Er) while at 24 h, small (RE)ANCs accumulated at tumor sites over 10-fold more than RE(Er) or large (RE)ANCs. Mean values ± s.e.m.; n=10 for 12 h and 24 h, n=5 for 48 h and 72 h (*P < 0.10; **P < 0.05; ***P < 0.02) determined by one-way ANOVA, Tukey post-hoc.

Based on our previous work, the surface modification of RE(Er)s with albumin affords the rare-earth phosphors unique biological properties, such as minimized aqueous aggregation, significantly reduced in vitro cytotoxicity, and molecular targeting potential.[128] In addition to being inherently biocompatible, albumin has been shown to exhibit preferential localization to tumors via multiple mechanisms including strong affinity toward secreted SPARC, a protein known to be upregulated in many different tumors such as breast, prostate, liver, brain and melanoma among others.[266] SPARC has been suggested to contribute towards the effectiveness observed with FDA-approved albumin-based nanoparticle drug delivery platforms.[264] In addition, albumin has been known to preferentially accumulate in various tumors, acting as a nutrient source for protein synthesis.[267] Furthermore, albumin is thought to assist in the endothelial transcytosis of albumin-bound plasma components into the extravascular space via

binding with the gp60 receptor (albondin).[265] As a consequence, albumin nanoparticles are able to take advantage of several native characteristics of tumor biology leading to enhanced tumor accumulation and prolonged nanoparticle retention in the tumor interstitial space.

Here, RE(Er)s were encapsulated in albumin to form nanocomposites ((RE)ANCs) of various diameters. Both sets of (RE)ANCs exhibited similar surface charges as well as albumin and RE(Er) loading. The hydrodynamic diameter was tunable with small (RE)ANCs approximately 100 nm in diameter and large (RE)ANCs 280 nm in diameter. The size of (RE)ANCs was regulated by adjusting the sodium chloride concentration in aqueous HSA, with lower sizes producing smaller particles by the reduction in electrostatic shielding leading to reduced protein aggeration.[175] The observed size of the nanoparticles in solution was much larger than when lyophilized and imaged under SEM, due to the reduction of bound water swelling the nanoparticles.

We first determined the pharmacokinetic and biodistribution profiles of the uncoated RE(Er)s and both sizes of (RE)ANCs in TGS mice in order to understand how both physical and surface properties affect nanoparticle behavior in vivo. Each set of (RE)ANCs was detected in the blood within 1 h of i.p. injection. In contrast to large (RE)ANCs, small (RE)ANCs showed sustained circulation beyond 2 h over the course of the study (8 h). These results indicate that both the size (100 nm) and surface properties (albumin) of small (RE)ANCs encourage the systemic distribution of the encapsulated RE(Er)s through the peritoneal barrier after i.p. administration.

All nanoparticle formulations cleared primarily through RES organs, such as the liver and spleen, which is expected of larger nanoparticles.[268,269] In addition, our

metabolic studies indicate a significantly greater degree of clearance through the feces than urine for all formulations. Combined with the biodistribution data, these measurements suggest that the nanoparticles are cleared primarily through hepatobiliary excretion. Extended studies are warranted to determine the total length of time required for complete clearance after administration.

Finally, to determine the feasibility of using SWIR to diagnose preclinical disease, we evaluated the ability of various RE formulations to identify tumor locations in TGS mice. As expected from the pharmacokinetic data, small (RE)ANCs accumulated to a greater degree in tumors located predominately around the ears of the mice. Notably, the SWIR emission signal was clearly observed even through dense, pigmented tumor tissue. For large (RE)ANCs, there was a significantly lower amount of tumor-associated SWIR signal delayed relative to small (RE)ANCs, indicating slower uptake kinetics for the large (RE)ANCs from the site of injection. The small hydrodynamic diameter and slightly negative zeta potential of the small (RE)ANCs may contribute to their enhanced tumor localization. It has been suggested that nanoparticles with slightly charged surfaces between 10-150 nm in diameter are more effective at penetrating and being retained in vascularized tumors.[270] The accumulation of the small (RE)ANCs at tumor sites may be due both to albumin-mediated transport into the tumor interstitium[265] and to the enhanced permeation and retention (EPR) effect mediated by endothelial cells lining blood vessels near tumors (**Fig. 4.5**). The EPR effect enables nanoparticles as large as 300 nm[271] to leak from blood plasma and accumulate in tumor tissue, explaining the reduced accumulation of large (RE)ANCs at lesion sites. Small (RE)ANCs may therefore

exploit a combination of physical and molecular properties which lead to their preferential uptake in tumors, amplifying SWIR emissions in the melanoma lesions.

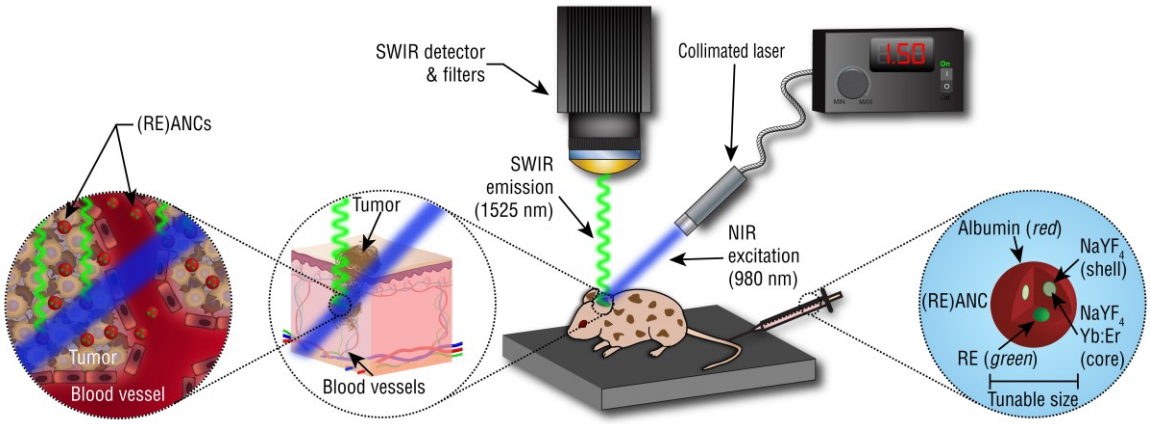

Figure 4.5 – Proposed Mechanism for (RE)ANC Tumor Accumulation in TGS Mice. Imaging of SWIR-emitting nanoparticles was performed before and after injection with our small animal SWIR imaging prototype (*main panel*). Driven by the demand for oxygen and nutrients, most growing solid tumors induce angiogenesis, including melanomas developed by TGS mice. During circulation, (RE)ANCs (*right panel*) avoid aggregation and are able to freely move through tumor vasculature (*middle panel*). Many tumor vessels tend to exhibit irregular branching patterns and abnormal architecture resulting in the enhanced permeability and retention (EPR) effect. Due to their sub-150 nm size and slightly negative surface charge[84], small (RE)ANCs are able to pass into the tumor interstitial space between these poorly-aligned endothelial cells lining the vasculature (*left panel*). In addition, the albumin coating may utilize commonly known albumin binding and transport pathways to facilitate the passage of the nanoparticles

across the tumor endothelium and retention within the tumor microenvironment[166,167,264,266,272].

4.5. Conclusion

Nanocomposites made of albumin and RE(Er)s exhibit strong SWIR optical emissions and can be synthesized at distinct nanoscale sizes. By encapsulating and tailoring the size of the albumin coating, the pharmacokinetic profile of the nanoparticles can be modulated and improved in a controllable fashion. In addition, albumin encapsulation results in a bioactive formulation which has been demonstrated to significantly increase RE(Er) accumulation and, consequently, enhanced SWIR signal intensity at tumor sites. These results offer a possible route for the clinical application of SWIR imaging as well as suggest a potential approach for altering the bioactivity of other inorganic particles such as QDs, magnetic and gold nanoparticles, using an FDA-approved biologic. Furthermore, the prolonged circulation of (RE)ANCs combined with albumin's strong drug binding properties could be exploited for SWIR-based imaging of drug delivery in deep or strongly light scattering tissues. We envision application of this platform imaging technology to a wide variety of biomedical applications including drug delivery tracking, deep tissue imaging and cancer lesion detection.

4.6. Supplementary Figures

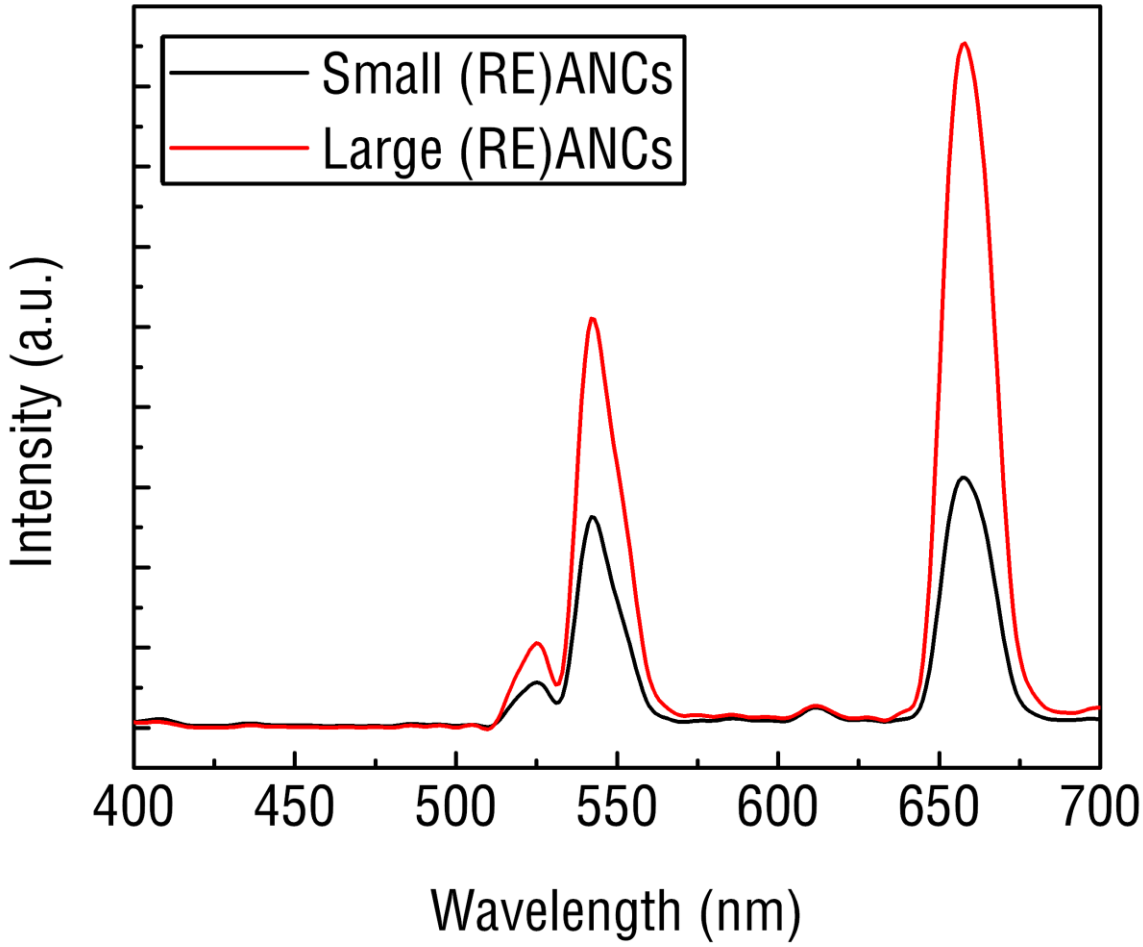

Supplementary Figure S4.1 – Visible Emission of (RE)ANCs. Both sizes of (RE)ANCs retain the upconversion fluorescence properties of RE(Er). Emission peaks occur around 550 and 650 nm, resulting in green-yellow emission.

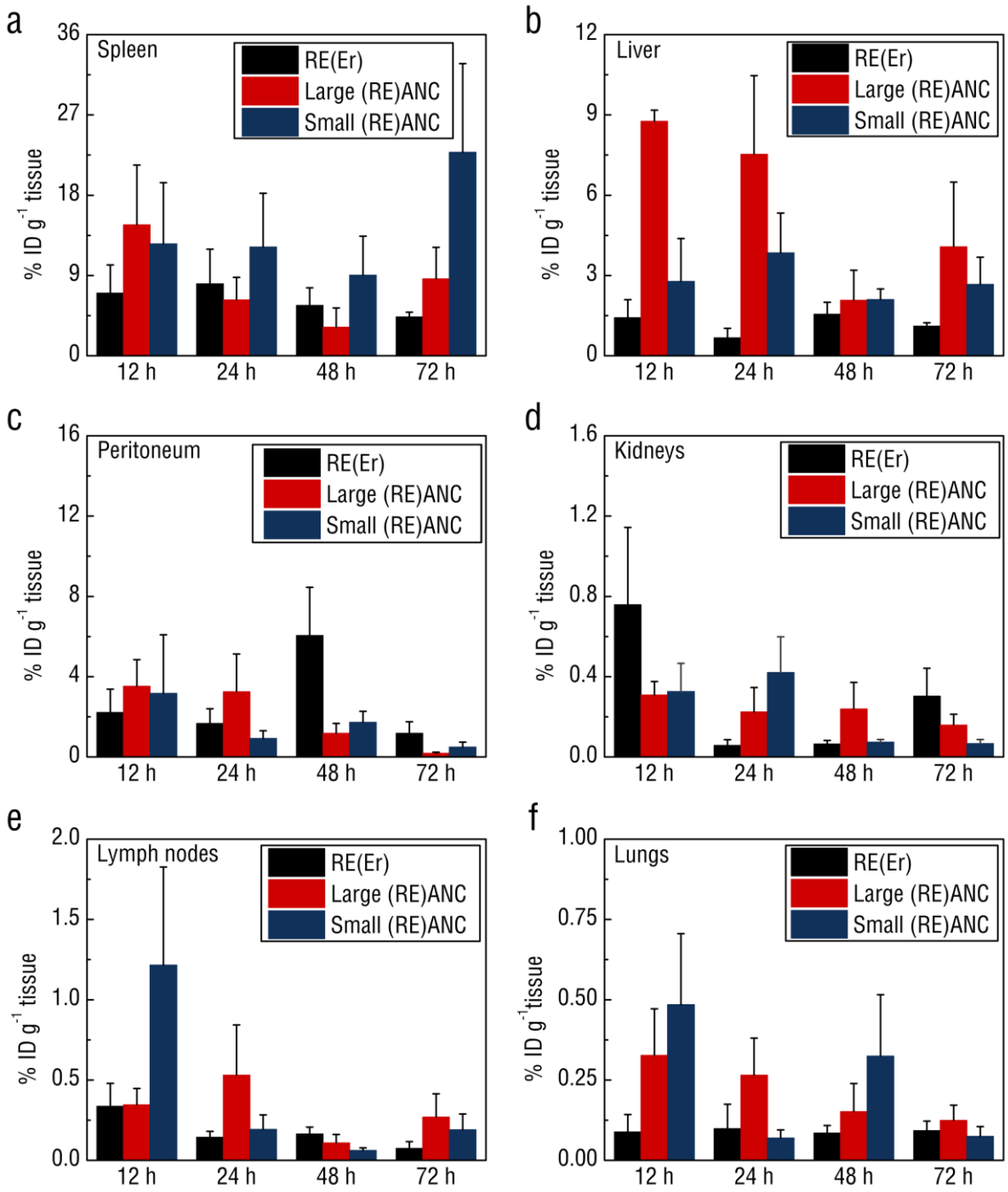
a
Spleen
RE(Er)
Large (RE)ANC
Small (RE)ANC
% ID g-1 tissue
36
27
18
9
0
12 h
24 h
48 h
72 h
b
Liver
12
9
6
3
0
c
Peritoneum
16
12
8
4
0
d
Kidneys
1.6
1.2
0.8
0.4
0.0
e
Lymph nodes
2.0
1.5
1.0
0.5
0.0
f
Lungs
1.00
0.75
0.50
0.25
0.00

Supplementary Figure S4.2 – Organ Biodistribution of Formulations. RE(Er)s, large and small (RE)ANCs were injected IP into TGS mice and organs analyzed at 12, 24, 48, and 72 hours post-injection (a-f). Blood, brain and heart displayed negligible yttrium presence (<0.1% ID g^{-1} tissue) at the tested timepoints. Mean values ± s.e.m.; n = 5.

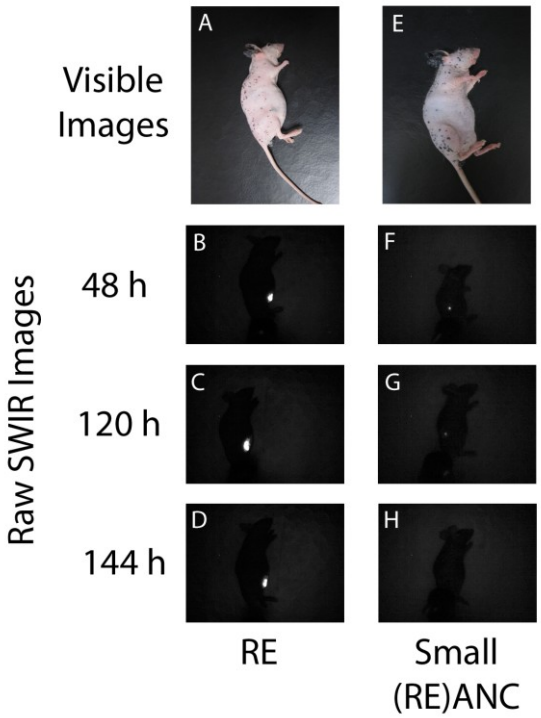

Supplementary Figure S4.3 – Long-Term Accumulation of Formulations after IP Injection. Mice exhibiting melanoma lesions injected with 100 µl of REs and (RE)ANS (2.0 mg RE ml^{-1}) via the peritoneum. Digital camera images of the mice prior to injection show the black, pigmented lesions are located throughout the mice bodies particularly on their ears, anus and back (*A, E*). After 48 h following IP injection, both mice injected with REs (*B*) and small (RE)ANCs (*F*) exhibit SWIR emission around the site of injection when the 980 nm excitation laser diode irradiates the region. Over time, however, the emission of the (RE)ANCs diminishes (*G-H*), indicated the nanoparticles are clearing the injection site, in contrast to the REs (*C-D*), which appear to remain at the site of injection.

CHAPTER 5

MULTIFUNCTIONAL ALBUMIN NANOPARTICLES FOR ENHANCED TUMOR PENETRATION AND DRUG DELIVERY

Note: This chapter consists of work that has been done in collaboration with two other collaborator students (Mingjie Cui and Margot Zevon). The author of this dissertation has contributed to the project conceptualization and feasibility analysis, research design, nanoparticle characterization and data analysis.

Sections of this chapter are currently being prepared for publication elsewhere as part of an article entitled:

"Collagenase modified albumin nanoparticles for enhanced tumor penetration and multi-drug delivery"

D.J. Naczynski, M. Zevon, M. Cui, C.M. Roth, P.V. Moghe

Abstract

Nanoparticles can be engineered to improve current cancer therapies by solubilizing poorly soluble drugs, facilitating uptake into cells and tumor masses, and enhancing site drug bioavailability. In this study, albumin nanoparticles (ANPs) were fabricated and modified as tumor penetrating dual drug delivery vehicles. ANPs were conjugated to two therapeutic agents and an ECM protease and their cytotoxicity was evaluated over 96 hours. Curcumin and riluzole were absorbed onto the surface of the ANPs without loss of drug efficacy against cultured human melanoma cells. There was no associated cytotoxic effect on healthy cultured human melanocytes indicating drug specificity. The drug loaded ANPs were conjugated to collagenase to allow for deeper tumor penetration and evaluated using a three-dimensional multicellular tumor spheroid model. The collagenase associated particles exhibited greater tumor penetration into the spheroid mass after 96 hours. The collagenase coated, drug loaded nanoparticles induced more cell death than the particles loaded with the two drugs alone. As controls, the collagenase coated ANPs with no drugs bound to the surface had no cytotoxic effect. This study illustrates the feasibility of designing multifunctional nanoparticles that can penetrate solid tumors, increasing the effect of one or more associated therapeutic agents.

5.1. Introduction

Despite remarkable advances in drug discovery, many chemotherapeutic compounds are poorly soluble,[273,274] have limited penetration through solid tumors[275,276] and are susceptible to drug resistance.[277-280] Currently, drug delivery in oncology relies on the use of solvent-based approaches,[281] which pose significant risk of toxicity,[282] result in uncontrollable systemic distribution[283,284] and limit the overall effectiveness of potent therapeutic compounds.[285] Advanced nanomaterial-based approaches have the potential to overcome the numerous challenges facing drug delivery into solid tumors. In particular, nanoparticles can be designed with uniquely advantageous properties through the control of size, surface characteristics and chemical composition.[84] Furthermore, nanoparticles offer a platform on which to engineer multiple functionalities which can act together toward improving drug delivery and therapeutic response.[286]

In addition to improving the solubility of hydrophobic drugs,[274] nanoparticles can sequester and deliver multiple agents simultaneously, bypassing cellular drug resistance mechanisms[287,288] and promoting synergistic therapeutic response.[289] Nanoparticles can be used to predictably control drug pharmacokinetics and tissue distribution,[163] limiting non-targeted side effects on healthy tissue.[290] Regulation of nanoparticle size is known to influence the passive targeting of tumor tissue through leaky vasculature,[291] while modifying nanoparticle surface properties with cancer targeting ligands can further lead to more active tumor targeting.[292] The encapsulation of contrast agents[253] for tracking drug distribution and incorporation of tumor penetrating peptides to facilitate more homogenous drug release in tumors[293,294] are other strategies that can be exploited to improve the effectiveness of nanoparticles as therapeutic delivery agents.

Nanoparticles carrying paclitaxel and composed of human serum albumin (*nab*-paclitaxel, Abraxane ®, Abraxis BioScience Inc.) have already been approved by the FDA for use in the treatment of metastatic breast cancer.[295,296] *Nab*-paclitaxel has been shown to sequester large amounts of therapeutic cargo,[164,297] improve the pharmacokinetics and circulation half life of antitumor agents,[163] reduce in vivo toxicity associated with solvent delivery systems[281] and possibly enhance tumor uptake of therapeutics through albumin binding interactions.[166,264,265] However, as a first-in-class nanoparticle system, *nab*-paclitaxel has great potential to be re-engineered for enhancing therapeutic delivery and improving tumor response following treatment.

Here, we report on the design of an albumin-based nanoparticle platform that has integrated several distinct functionalities including: (1) multi-drug delivery, (2) active tumor penetration and (3) optical detection. Albumin nanoparticles (ANPs) were synthesized for the simultaneous delivery of curcumin and riluzole, using the inherent multi-drug binding properties of albumin. To improve nanoparticle penetration into extracellular matrix (ECM)-dense solid tumors, ANPs were formulated using an ECM degrading protease and tested in a 3-D tumor spheroid model. ANPs as formulated are intrinsically fluorescent without conjugation of exogenous dye, which enabled the visualization of nanoparticle penetration through the tumor spheroids using conventional fluorescence techniques. Multifunctional ANPs can serve as a powerful nanomaterial platform that offers more effective therapeutic delivery into solid tumors.

5.2. Methods

5.2.1. Reagents

Molecular biology grade ethanol (99.5%), HPLC grade methanol (99.8%), HPLC grade water with 0.1% trifluoroacetic acid (TFA) and HPLC grade acetonitrile with 0.1% TFA (ACN) were purchased from Sigma-Aldrich and used without further purification. Collaganease from *Clostridium histolyticum* was also purchased from Sigma-Aldrich (St. Louis, MO, USA). Curcumin was purchased from Cayman Chemical Company (Ann Arbor, MI, USA). Riluzole hydrochloride was purchased from Tocris Bioscience (Ellisville, MO).

5.2.2. Cell Culture

Human melanoma cell lines C8161(+), C8161(-) and WM239 and human melanocyte cell line AR7119 were generously provided by Dr. Suzie Chen. RPMI-1640 media was purchased from American Type Culture Collection (ATCC, Manassas, VA). Fetal bovine serum (FBS), trypsin–EDTA, streptomycin, and penicillin were purchased from Invitrogen. Cells were routinely maintained in RPMI-1640 media, supplemented with 10% FBS, 100 μg/ml penicillin and 100 μg/ml streptomycin at 37 °C, in humidified atmosphere of 5% CO_2.

5.2.3. Albumin Nanoparticle Synthesis

Albumin from human serum (fraction V, purity 96–99%, 65 kDa) and glutaraldehyde (8% solution) were purchased from Sigma–Aldrich and used without further purification. 2% (w/v) solution of HSA was dissolved in 10 mM NaCl to prepare

200 nm ANPs, and 2 mM NaCl to prepare 100 nm ANPs. The pH of HAS solution was adjusted to 8.50 ± 0.05 with 0.1 M NaOH. Under continuous stirring at 700 rpm at room temperature, 2 mL ethanol was added at 1.5 mL min^{-1} to the HSA solution (500 μL) with a syringe pump (Harvard Apparatus PHD 2000, Holliston, MA). 2.34 μL glutaraldehyde was added to ANPs suspension as a cross-linker following ethanol addition. The particles were left for crosslinking overnight under stirring at 700 rpm at room temperature.

5.2.4. Albumin Nanoparticle Purification

ANPs were purified by three rounds of centrifugation for 8 min at 4 °C (Beckman Coulter, Avanti J-E Centrifuge). 16 100× *g* was set for 200 nm ANPs, while 48 400x g was set for 100 nm ANPs. Redispersion of the pellets to original volume with PBS was done following each round of centrifugation. Redispersion was performed in an ultrasonication bath (Fisher Scientific, FS60).

5.2.5. Albumin Nanoparticle Drug Loading

Curcumin was dissolved in ethanol to give a final concentration of 1 mg/mL and dissolved at room temperature for 30 min. Curcumin solution was added drop-wise into ANPs suspension to give final concentrations of 10 μM, 20 μM, 30 μM, 40 μM, 50 μM, 80 μM, 100 μM and 140 μM.

Riluzole was dissolved in ethanol to give a final concentration of 10 mM. Riluzole solution was then added into ANPs suspension to give final concentrations of 50 μM (0.135% w/v), 60 μM (0.162% w/v), 70 μM (0.189% w/v), 80 μM (0.216% w/v), 90 μM (0.243% w/v), and 100 μM (0.270% w/v).

For dual drug loading, the curcumin solution was added drop-wise into ANPs suspension to give final concentrations of 0.1% w/v, while the riluzole solution was added to give final concentrations of 50 μM (0.135% w/v), 60 μM (0.162% w/v), 70 μM (0.189% w/v), 80 μM (0.216% w/v), 90 μM (0.243% w/v), and 100 μM (0.270% w/v). In all instances, the drug mixtures were adsorbed onto the nanoparticles by agitation for 3 hours at room temperature.

Drug loaded ANPs were purified by one round of centrifugation for 8 minutes at 4 °C (16 100× *g* for 200 nm ANPs, while 48 400x g for 100 nm ANPs). To characterize the drug loaded ANPs, the pellets were redispersed to original volume with PBS following centrifugation. To test the drug loaded ANPs in physiological conditions, pellets were redispersed to 1/10 of original volume. Redispersion was performed as described before.

5.2.6. Physical Characterization of Albumin Nanoparticles

ANPs were studied using DLS and SEM. Particle size distributions and polydispersity indices were determined using zetasizer (Zen 3690, Malvern, Worcestershire, UK). Samples were diluted 40 times with deionized water for *z*-average size and polydispersity measurements. *Z*-average sizes and polydispersity indices of three sequential sample scans (3 runs $scan^{-1}$, 60 s $scan^{-1}$) were measured at a 90° scattering angle at 37°C. Three separate batches of particles were measured and averaged. ANP autofluorescence was measured using a spectrofluorometer (SpexFluoroMax-3, Horiba Jobin Yvon, Edison, NJ, USA).

5.2.7. Quantification of Drug Loading

The concentrations of drugs loaded on ANPs were determined by high-performance liquid chromatography (HPLC, Beckman Coulter Model 166) equipped with a Luna C18 column (3 μm, 100 x 4.6 mm i.d., Phenomenex, Torrance, CA). The drug loaded ANPs were frozen at -80°C overnight and lyophilized for 48 hours. The powders were resuspended in ethanol to original volume, followed by HPLC measurement. To determine curcumin and riluzole concentrations, a multistep chromatographic procedure was used. The flow rate was 0.9 ml/min over the entire separation. The mobile phase consisted of an isocratic elution of 30% ACN and 65% water containing 0.1% TFA for the first 7 min, followed by an isocratic elution of 75% ACN and 25% water containing 0.1% TFA for the next 9 min. Curcumin was detected at 420 nm, while riluzole was detected at 255 nm (Detector Module 168, Beckman Instruments, San Ramon, CA). Serial dilutions of curcumin and riluzole standards were used to construct a calibration curve, with the linear portion utilized for measurements.

5.2.8. Cell Viability Assay

The metabolic activity of viable cells was assessed by CellTiter 96 AQueous Non-Radioactive Cell Proliferation Assay (Promega, Madison, WI). Melanoma cell lines were cultured on 96-well polystyrene tissue culture plates at 5000 cells per well. After overnight incubation at 37°C, wells were treated with different drugs (single drugs or single drug loaded nanoparticles or dual free drug or dual drug loaded nanoparticles) of varying concentrations starting from 1 μM to 50 μM. At 0 h, 24 h and 96 h time points, MTS reagent (20 μL) was added to each well of the assay plate containing 10% v/v test

samples in culture medium (100 μL). The plates were incubated for 2 h at 37 °C in a 5% CO_2 atmosphere, after which the absorbance was measured at 490 nm using a plate reader. Background absorbance was corrected by preparing a set of control wells without cells containing the same volumes of culture medium, test sample, and MTS reagent. The measurements were carried out in triplicate. Cell viability was quantified by the relative number of live cells compared to a PBS negative control.

5.2.9. Drug Release

The release study was carried out using dialysis. The dialysis tubes (100 kDa, Spectrum Labs) were immersed in 15% ethanol for 30 min prior to use and then rinsed with phosphate buffered saline (PBS) solution. 1 mL of base ANPs, drug loaded ANPs and the native drug solution were dialyzed against 200 mL of PBS (pH 7.4) with 25% ethanol. At each time point, 0.25 mL of ANPs suspension was withdrawn from the inside of tubes, and the PBS was replaced with fresh solution. The samples withdrawn at each time points were lyophilized and re-suspended with ethanol. The levels of curcumin and riluzole in each sample were measured using HPLC as described above.

5.2.10. In vitro Cellular Uptake of Drug Loaded ANPs

C8161(+) cells were seeded into 24-well plates at a density of 10^5 cells/well, and incubated at 37°C for 24 h. To quantify the relative degree of drug loaded ANPs uptake, C8161(+) cells were treated with base ANPs and drug ANPs for 4 h. The cells were fixed, washed, and stained with Hoechst prior to imaging. Auto-fluorescence from

albumin, curcumin, and fluorescence of Hoechst were captured. Images were processed and quantified with ImageJ software.

5.2.11. Multicellular Spheroid Formation

Melanoma cells (C8161+) and human foreskin-derived fibroblast cells (HFFs) were grown in monolayer cultures prior to spheroid formation. To produce spheroids, both types of cells were trypsinized, centrifuged and mixed in 200 ml complete media (RPMI media with 10% FBS and antibiotics). 20 μL of cell suspensions were aspirated and applied on a plate cover to form small droplets. Cell droplets were kept in an incubator at 37°C for 4 days. Spheroids that expanded to a diameter of 400-500 μm, were transferred to a 24-well agar plate and allowed to incubate for 2 additional days before processing.

5.2.12. Preparation of Collagenase-Coated Nanoparticles

2% (w/v) solution of HSA and 0.1% w/v collagenase were dissolved in 10 mM NaCl to prepare 200 nm ANPs, and 2 mM NaCl to prepare 100 nm ANPs. Similar with the methods for preparing ANPs, the pH of HSA collagenase solution was adjusted to 8.50 ± 0.05 with 0.1 M NaOH. Under continuous stirring at 700 rpm at room temperature, 2mL ethanol were added at 1.5 mL min^{-1} to 500 μL HSA solution with a syringe. 2.34 μL glutaraldehyde was added and the particles were left to cross link overnight under stirring at 700 rpm and room temperature. Using the same methods with ANPs, collagenase–coated nanoparticles were purified and characterized. Following centrifugation, ANPs

pellets were redispersed to 1/10 of original volume with PBS for introduction to the tumor spheroid model.

5.2.13. Nanoparticle Penetration in Spheroids

Spheroids were handpicked with a pipette and transferred to a new 24-well agar plate. The medium was removed by aspiration, and spheroids were washed with PBS (pH 7.4) before further processing. The spheroids were treated with base ANPs, dual drug loaded ANPs, base collagenase-coated nanoparticles and dual drug loaded collagenase-coated nanoparticles with varying concentrations of 0% v/v, 5% v/v, 10% v/v and 25% v/v in culture medium for 72 h and 96h.

For the analysis of spheroids penetration by nanoparticles, spheroids were fixed, Hoechst stained and then processed in two ways: 1) cross sectioning, 2) confocal imaging directly. Spheroids were transferred to a cryomold, covered in optimal cutting temperature compound (O.C.T, Tissue-Tek, Torrance, CA), flash frozen, and processed by cutting 25 μm sections using a cryostat (Shandon Cryotome E, Thermo Scientific, Waltham, MA). Fluorescent images of spheroid sections were obtained with a confocal laser microscope (Leica Microsystems Inc., Bannockburn, IL).

Confocal microscopy images of the treated spheroids were analyzed by a series of Matlab algorithms. Two fluorescence modes were imaged, the green autofluorescence of the albumin shells and the blue nuclear Hoechst stain. The two channels were converted into binary masks, and any holes in the images were filled. The number of pixels per mask was then calculated and used to create a ratio of albumin fluorescence to cellular fluorescence. This was used as a measure of ANP penetration, as the greater the area of

the albumin fluorescence is associated with a greater percentage of nanoparticles within the spheroid (**Supplementary Fig. S5.1)**.

5.4. Results

5.4.1. In vitro Cytotoxicity of Curcumin, Riluzole and Combination Treatments

The therapeutic effects of curcumin and riluzole were evaluated using C8161+ human melanoma cells and AR7119 immortalized human melanocytes. Both cell lines were exposed to curcumin (**Fig. 5.1A,B**), riluzole (**Fig. 5.1C,D**) or cocktails of both compounds for 96 h (**Fig. 5.1E,F**). C8161+ cells were more sensitive towards curcumin at concentrations above 10 μM than AR7119 cells. At very high concentrations (80 μM), however, curcumin induced significant cytotoxicity in both cell lines. Riluzole treatment showed greater dose-dependent cytotoxicity in the C8161+ cells than AR7119 cells. Cell viability assays revealed that while 40 μM riluzole inhibited the proliferation of melanoma cells, cytotoxicity was also induced in healthy melanocytes (~30% reduction of proliferation). To test the effect of combining the two therapeutics, the concentration of riluzole was fixed at 10 μM and curcumin concentration was varied. From these studies the optimal combination of both drugs in solution was determined to be 10 μM riluzole and 40 μM curcumin. This combination of riluzole and curcumin in solution yielded the greatest combined cytotoxic effect against the C8161+ melanoma cells with minimal adverse effect on the viability of the AR7119 melanocytes.

5.4.2. Characterization of Nanoparticles

Once we established the therapeutic benefits of free riluzole and curcumin, we formulated albumin nanoparticles (ANPs) to sequester both compounds for delivery. ANPs were formed through the solvent-induced controlled coacervation of albumin. By varying the amount of sodium chloride in the HSA solution prior to coacervation, the size

of the final nanoparticles could be controlled. Two sets of ANPs were generated with hydrodynamic diameter ~100 nm (small) and ~200 nm (large), as confirmed using dynamic light scattering (DLS). Both sets of ANPs exhibited low polydispersity and negative zeta potentials in phosphate-buffered saline (PBS, pH 7.4) (**Supplementary Table S5.1**). Approximately 65% and 50% of the starting human serum albumin (HSA) were incorporated into the small and large ANPs, respectively. Scanning electron microscopy (SEM) of the ANPs revealed spherical, monodispersed populations of discrete nanoparticles (**Fig. 5.2A,B**), corroborating the results seen with DLS.

5.4.3. ANP Drug Loading and Release Kinetics

Curcumin and riluzole were first adsorbed separately at various concentrations onto the surface of fully formed ANPs of both sizes. The particles were then characterized with DLS to determine the effect of drug loading on particle size and polydispersity (**Supplementary Fig. S5.2**). Above 80 μM, curcumin led to a marked increase in both the size and polydispersity of the small ANPs and larger polydispersity in the large ANPs. Adsorbing both agents increased the hydrodynamic diameter of the particles by 10 nm in the large particle case and approximately 15 nm for the smaller formulation compared to unloaded ANPs.

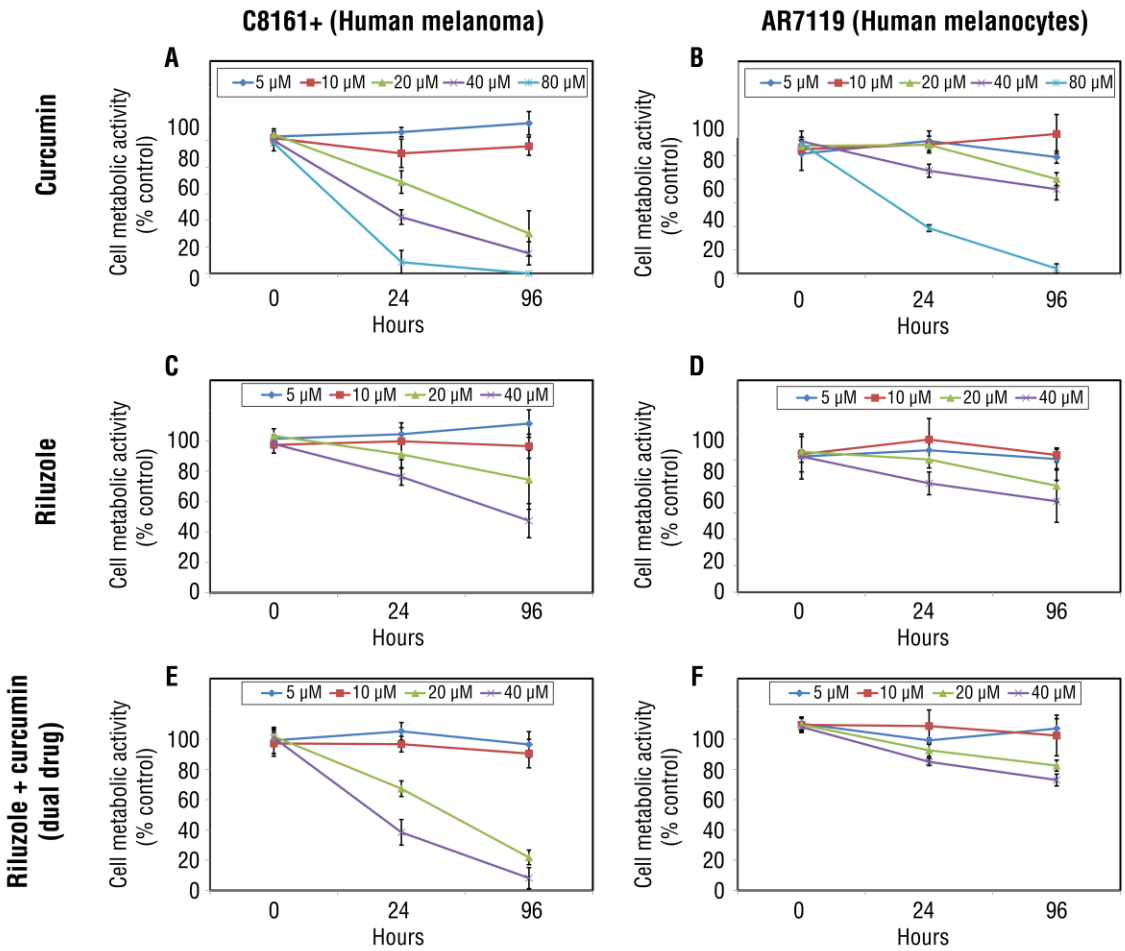

Figure 5.1 – In vitro Cytotoxicity of Curcumin, Riluzole and Dual Drugs. Therapeutic effect of curcumin (A-B), riluzole (C-D), and 10 µM riluzole + curcumin (E-F) on C8161+ melanoma cells (A,C,E) and healthy AR7119 melanocytes (B,D,F). Error bars represent standard deviation for n=3.

Both drugs were then loaded together onto the ANP formulation. Dual drug loading had a negligible effect on the size and polydispersity of the large ANPs, but increased both the size and polydispersity of the small ANPs (**Fig. 5.2C,D**). The drug

loading efficiency was determined by HPLC. For both small and large ANPs, the concentration of curcumin added to the formulations was fixed at 80 μM and the amount of riluzole varied. Across the concentrations tested, there was no change in the binding efficiency of riluzole or curcumin (**Supplementary Fig. S5.3**). Riluzole and curcumin bound with efficiencies of ~75% and ~60%, respectively, for both the large and small ANPs. The dual drug binding efficiencies compared to those observed with single drug loadings (**Supplementary Table S5.3**).

To analyze the release profiles of curcumin and riluzole from the ANPs, larger ANPs loaded with 10 μM riluzole and 40 μM curcumin were dialyzed against a 25% ethanol and PBS solution under agitation. Both riluzole and curcumin displayed slower release kinetics from the dialysis cassette than the free drugs (**Fig. 5.3**), with 50% of riluzole and curcumin release by 1 h and 3 h, respectively. In contrast, 50% of ANP-bound riluzole and curcumin were released by 3 h and 12 h, respectively.

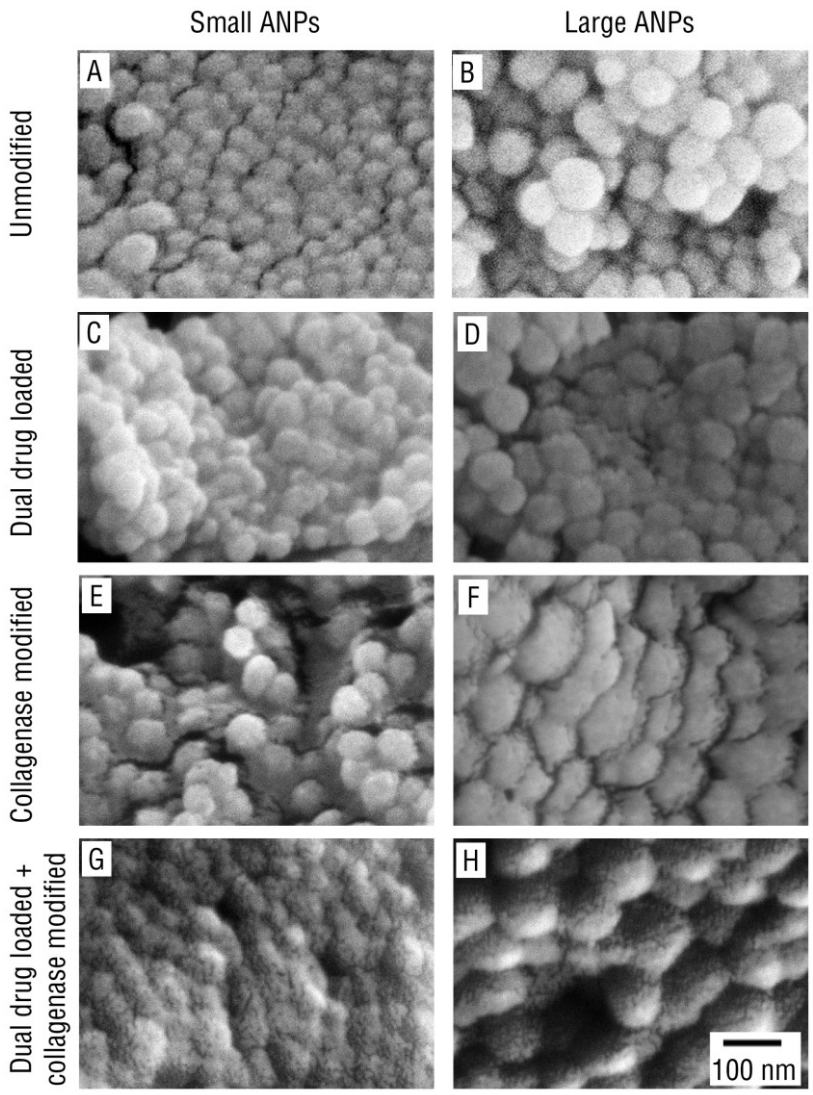

Figure 5.2 – SEM Imaging of Variously Sized and Formulated ANPs. Scanning electron microscopy (SEM) images of small (A) and large (B) ANPs reveal monodisperse, spherical nanoparticles. Both curcumin and riluzole were loaded on the small (C) and large (D) nanoparticles. Collagenase modification altered the morphology of the small (E) and large (F) ANPs. This change in morphology was more evident after both drugs were loaded on the small (G) and large (H) collagenase ANPs.

5.4.4. Efficacy of Dual Drug Loaded ANPs In vitro

To determine the effect of nanoparticle association on the efficacy of the therapeutic agents, both riluzole and curcumin were incorporated into ANPs. The efficacy of the loaded nanoparticles was compared against the free drugs in solution against a 2-D monolayer of cells. For equivalent levels of dual drug loading concentrations (10 μM riluzole and 40 μM curcumin), both large and small nanoparticles exhibited similar effectiveness by 96 hours against C8161+ melanoma cells (**Fig. 5.4A**). Comparative trends were similar for AR7119 melanocytes between free and ANP-bound formulations, though the melanocytes were overall less significantly affected by the drug treatment (**Fig. 5.4B**).

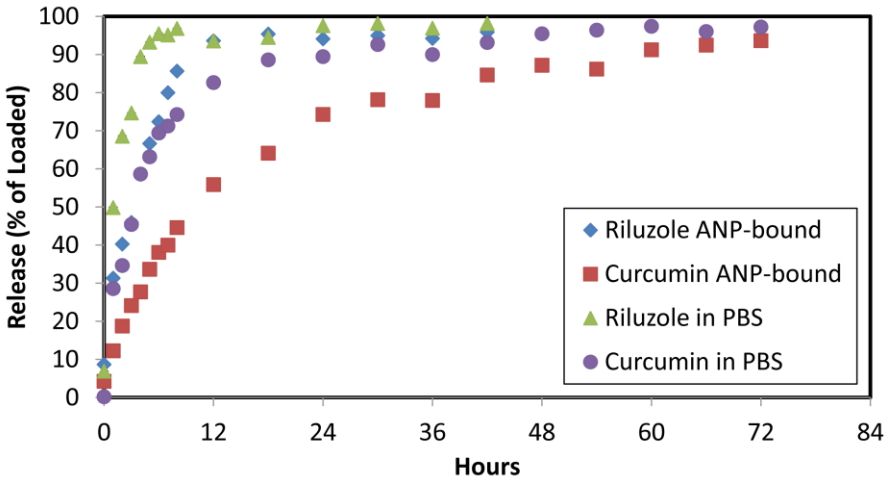

Figure 5.3 – In vitro Release of Various Drug Formulations. Time dependent release of curcumin and riluzole from large ANPs and PBS solutions (10 μM riluzole or 40 μM curcumin). Solutions were dialyzed against 25% ethanol/PBS releasing medium at 37°C. Free drugs in PBS were released twice as fast as those sequestered by ANPs.

5.4.5. Collagenase Modification of ANPs and Dual Drug Loading

Tumor penetrating ANPs were formulated by decorating the surface of the particles with collagenase. The collagenase-albumin nanoparticles (cANPs) were physically characterized through DLS and SEM imaging as before. Small cANPs were approximately 10 nm larger in size than unmodified small ANPs and exhibited slightly larger polydispersity (**Supplementary Table S5.2**). Large cANPs were similar in both size and polydispersity to unmodified large ANPs. SEM images revealed somewhat rougher and uneven surfaces on both sets of cANP (**Fig. 5.1E,F**).

Small and large cANPs were subsequently loaded with both curcumin and riluzole as before. Loading of the drugs led to increase in size and polydispersity for both small and large cANPs (**Supplementary Table S5.2)**. The surfaces of both sets of drug-loaded cANPs were significantly more uneven when compared to drug-loaded ANPs (**Fig. 5.1G,H**).

5.4.6. Efficacy of Dual Drug Loaded cANPs in a 2-D Cell Culture Model

Drug-loaded cANPs were first evaluated in a 2-D cell culture model to determine whether the incorporation of collagenase altered the therapeutic efficacy of the riluzole and curcumin combination. Unloaded cANPs had little effect on cell proliferation for either the C8161+ (**Fig. 5.4A**) or AR7119 cells (**Fig. 5.4B**). Drug-loaded cANPs induced a similar degree of cytotoxicity when compared to both free drug and drug-loaded ANPs in C8161+ cells. This was also seen in AR7119 cells though cytotoxicity was significantly less than with the C8161+ cells.

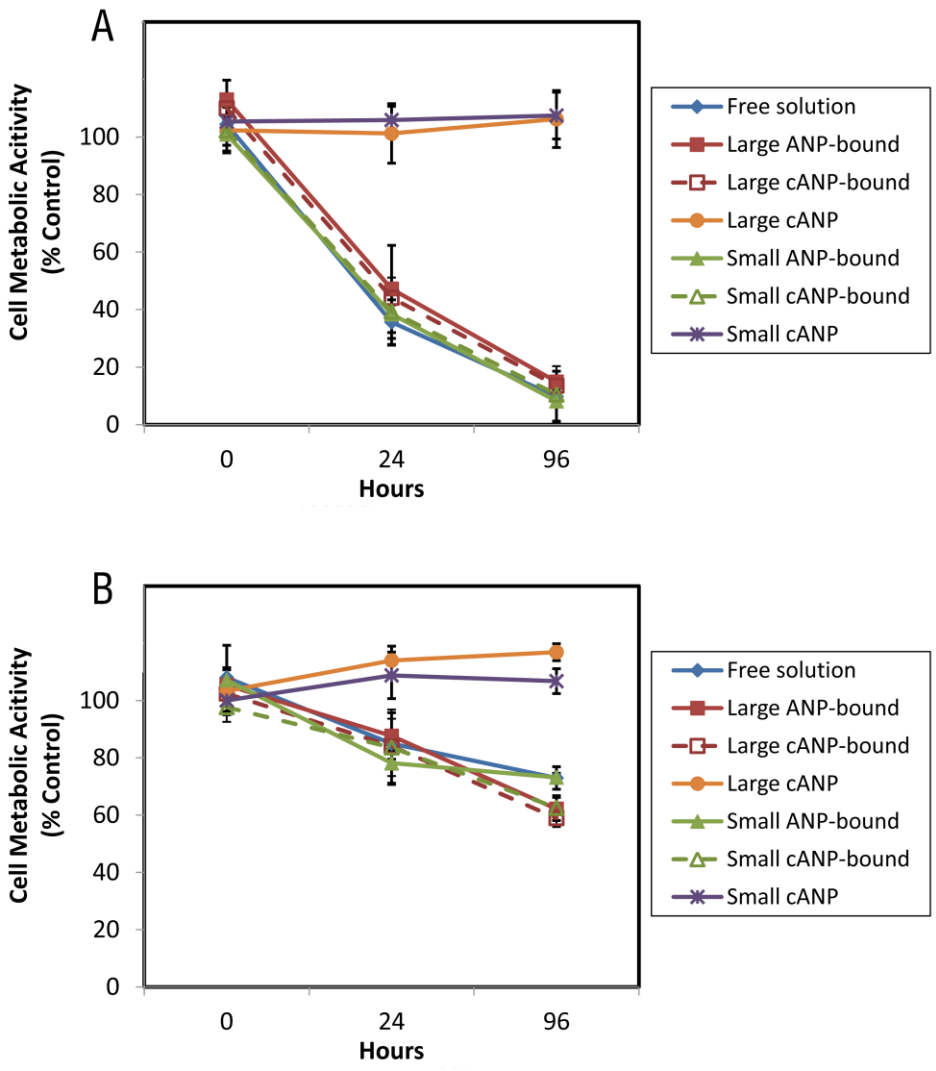

Figure 5.4 – In vitro Cytotoxicity of Free and Nanoparticle-Bound Drugs in 2-D Cell Culture. In vitro cytotoxicity of 10 μM riluzole and 40 μM curcumin formulations on 2D monolayer cultures of C8161+ human melanoma cells (A) and AR7119 healthy human melanocytes (B). All tested drug conditions showed significantly more cytotoxicity against the cancerous cell line. Curcumin and riluzole showed no loss of activity after binding to the ANPs or collagenase ANPs (cANPs). The cANPs showed no inherent cytotoxicity in either cell line. Error bars represent standard deviation for n=3.

5.4.7. Penetration of Dual Drug Loaded cANPs in a 3-D Multicellular Spheroid Model

Drug-loaded cANPs were further evaluated in a 3-D cell multicellular spheroid model consisting of C8161+ melanoma cells co-cultured with human foreskin-derived fibroblasts in order to assess the activity of collagenase for tumor penetration. The penetration of cANPs into the spheroids could be visualized using their inherent autofluorescence (**Supplementary Fig. S5.4**).

Spheroids were exposed to small and large ANPs with and without collagenase for 96 hours. The imaging studies revealed that even without the collagenase coat, the size of the nanoparticles influenced their penetration significantly. After 96 hours, the small undecorated particles showed much more effective penetration than the large undecorated ANPs with fluorescence seen in the center of the spheroid (**Fig. 5.5A,C**). For the large undecorated ANPs, the majority of the particles remaining on the periphery of the tumor (**Fig. 5.5C**).

Collagenase decoration improved tumor penetration for both the small and large particles (**Fig. 5.5B,D**). The small cANPs showed greater accumulation around the periphery of the spheroid (**Fig. 5.5B**), while green fluorescence was observed in the center of the spheroid indicated improved penetration for the large cANPs (**Fig. 5.5D**).

Images of cANP penetration were quantified and compared to ANPs (**Fig. 5.5E**). Based on total area of the spheroid imaged, small cANPs penetrated approximately 6% of the spheroid compared to 0.6% for small ANPs 96 h. Large cANPs penetrated 27% of the spheroid compared to 0.1% for large ANPs in 96 h.

5.4.8. Efficacy of Dual Drug Loaded cANPs in a 3-D Multicellular Spheroid Model

Finally, we evaluated the therapeutic efficacy of cANPs loaded with both curcumin and riluzole in the spheroid model. Spheroids were exposed to drug loaded ANPs with and without collagenase modification. After 24 h, drug-loaded small cANPs induced a significantly greater degree of cytotoxicity in the spheroids than unmodified drug-loaded ANPs (**Fig. 5.5F**). By 96 hours, both the large and small drug-loaded cANPs had induced greater cytotoxicity in the spheroids as compared to ANPs unmodified with collagenase.

5.5. Discussion

Cancer drug resistance is a major cause in the failure of chemotherapy and a significant challenge in cancer treatment.[298,299] Drug resistance often arises from the inefficient delivery of therapeutic agents into a tumor.[108,299] Poor therapeutic delivery can lead to concentration gradients of drugs with a tumor, which may facilitate the development of drug resistance in cancer cells that are exposed to low or negligible concentrations of therapeutics.[275,300] Effective delivery vehicles must be able to penetrate tumor tissue effectively and treat every cancer cell with drugs at concentrations sufficient to elicit a therapeutic response.[108] Although numerous physical characteristics influence drug penetration through tumors,[108] the tumor ECM (composed of collagens, proteoglycans, and various glycoproteins)[301] is a significant barrier limiting drug transport and penetration. Furthermore, it is well known that drug resistance occurs almost universally when tumors are treated with single therapeutic agents.[302] This has led to the development of combination therapies in order to combat the onset of resistance.

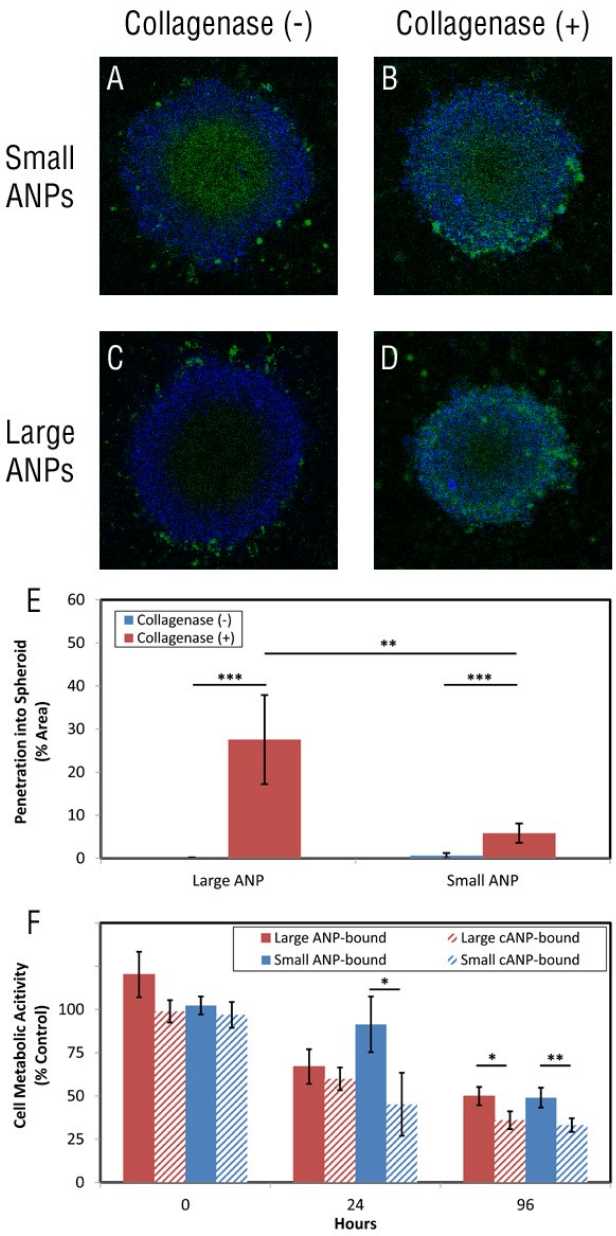

Figure 5.5 – 3-D Culture Treatment with Collagenase ANPs. Confocal microscopy images of multicellular spheroids stained with Hoechst (blue) treated with various dual loaded ANP formulations (green) up to 96 hours (A-D): smaller dual drug loaded ANPs (A), smaller dual drug loaded cANPs (B), larger dual drug loaded ANPs (C), and larger

dual drug loaded cANPs (D). Images were quantified to show that there is significantly better penetration of both cANPs compared to ANPs, and that the large cANPs penetrate better into the spheroids than the small cANPs by 96 h. The small cANPs show a time dependent therapeutic effect beginning at 24 h on 3D multicellular spheroids, while cytotoxicity is observed with the large cANPs by 96 h (F). Error bars represent standard deviation (SD) for n=5 (for image quantification) and n=3 (for cytotoxicity), * $p<0.05$; ** $p<0.02$; *** $p<0.005$ (*t* test).

The goal of this work was to investigate a new approach for engineering albumin nanoparticles (ANPs) to more effectively deliver therapeutic compounds and treat tumors progression. As drug delivery vehicles, ANPs have been shown to exhibit low immunogenicity in vivo, enhanced accumulation in tumors and strong but reversible drug-binding properties.[164] In addition, albumin can bind multiple, structurally dissimilar compounds simultaneously in binding pockets distributed across its surface.[165,297] We have exploited this feature of albumin for the purpose of co-delivering curcumin and riluzole to cancer cells using ANPs. We further modified the drug-loaded ANPs with collagenase, an ECM-protease shown to improve drug penetration into tumors and movement through the ECM.[294,303] Our final nanoformulation, which includes albumin nanoparticles, curcumin, riluzole, and collagenase, is entirely composed of FDA-approved compounds.

Curcumin is an herbal derivative of the spice turmeric and is known to have anti-cancer and anti-inflammatory properties.[304-306] Furthermore, curcumin can act as a potent

chemosensitizer, improving tumor cell sensitizer towards chemotherapy through downregulation of NF-κB and NF-κB-regulated gene products.[304,307] However, its numerous therapeutic benefits are offset by poor water solubility and bioavailability.[308] Riluzole is a noncompetitive glutamate release inhibitor that is currently in use for patients with amyotrophic lateral sclerosis (ALS or commonly Lou Gehrig's disease). Recently, ectopic expression of the neuron metabotropic glutamate receptor 1 (GRM1) in melanocytes has been shown to be highly oncogenic both in vitro and in vivo.[309] Disruption of GRM1 signaling in melanomas using glutamate antagonists like riluzole has been shown to suppress melanoma cell growth and trigger apoptosis in vitro and lead to apoptosis and decreased tumorigenesis in vivo.[310]

While albumin nanoparticles are well-established as drug carriers, there are a number of variables to be addressed in re-engineering them for novel applications such as dual drug delivery. Drug loading, release rates and pharmacodynamics are all issues to be addressed in a dual drug nanoformulation. As we have developed the ability to vary the size of ANPs controllably, we first adsorbed both curcumin and riluzole onto two sizes of ANPs in order to determine whether nanoparticle size can influence the degree of drug binding.

For both small and large ANPs, dual drug loading did not significantly alter size or surface morphology which indicates that binding does not change the stability of the nanoparticles. Riluzole appeared to bind in a non-saturable manner to the ANPs over the concentrations tested (**Supplementary Fig. S5.2**). Furthermore, the binding of riluzole did not change the binding efficiency of curcumin, suggesting a non-interacting or non-overlapping nature of binding sites of the two compounds to ANPs. Drug release from

the ANPs was slower than the free drug in solution from the dialysis cassette. The slower release of curcumin compared to riluzole from the ANPs may be due to its greater hydrophobicity.[308,311] Despite the variations in release rate, both riluzole and curcumin maintained therapeutic efficacy against melanoma cells when formulated with ANPs. This indicates that the drugs associate with the nanoparticles in a manner that does not adversely affect their therapeutic action.

Previous research has shown that drug delivery to solid tumor masses is frequently challenging for nanoparticle based systems, greatly limiting successful treatment.[276] Several techniques have been described to overcome this barrier to treatment. Collagenase treated nanoparticles have shown increased penetration into the spheroid core with little corresponding size increase and improved tumor accumulation in spheroid masses vs. unfunctionalized particles.[294] Here, we tested the collagenase coated ANPs (cANPs) in a multicellular spheroid model of co-cultured human melanoma and fibroblast cells. The multicellular spheroids used in this study were grown via the hanging drop method, which yields consistent and reproducible spheroids and a high degree of control over the size of the cellular mass.[312] Multicellular spheroids exhibit many characteristics of tumors, such as extracellular matrix generation and oxygen and nutrient gradients.[313]

We first evaluated the morphology of cANPs using SEM and found that collagenase decoration results in a textured nanoparticle surface. This may be due to the different forms of collagenase with wide-ranging molecular masses and structures that are present in commercially prepared *Clostridium histolyticum* collagenase.[314,315] After loading cANPs of various sizes with both therapeutic compounds, drug delivery was

compared to ANPs on monolayers of healthy and melanoma cells. The cANPs retained the cytotoxic effects of curcumin and riluzole on the cancerous cells; their effect on the C8161+ melanoma cells was nearly identical to that of the ANPs loaded with drugs alone. This shows that the addition of collagenase to the nanoparticles did not likely alter the binding or release of the therapeutic payload, and did not inhibit the action of either drug. The drug loaded cANPs had minimal effect on the metabolic activity of the healthy melanocytes vs. the drug loaded ANPs alone. From this we can infer that the collagenase coating alone has little or no cytotoxic effect and does not induce cell death after 96 hours when bound to the albumin nanoparticles.

As expected, confocal imaging of ANP penetration into multicellular spheroids revealed strong size dependence with smaller ANPs penetrating more effectively.[294] While collagenase incorporation improved the penetration of both small and large ANPs, indicating that crosslinking into the albumin nanoparticles did not deactivate collagenase, large cANPs penetrated approximately 5-fold more than small cANPs (27% to 6% of total spheroid area imaged). Currently, we can only speculate on the causes behind this difference. The amount of collagenase may be greater on the large than small cANPs. Alternatively, the presentation of collagenase on the surface of the large cANPs may be more favorable for its enzymatic activity. Studies have shown that the enzymatic activity of protease adsorbed on the surface of nanoparticles can be significantly alter by nanoparticle size.[316] These results, however, show that protease adsorption onto larger nanoparticles results in greater loss of secondary structure. In our system, the protease is incorporated within the nanoparticle which may restrict the perturbations in secondary structure caused by adsorption.

Furthermore, the cytotoxicity data on the spheroids reveals that after 24 h, drug loaded small cANPs induce significantly greater cellular toxicity than the small ANPs and large cANPs. However, after 96, both the small and large cANPs elicit approximately the same degree of cytotoxicity in the spheroids. This may be due to better diffusion of the small than large cANPs into the spheroid at earlier timepoints. After this initial penetration, however small cANPs appear to penetrate less into the spheroid than large cANPs. It is possible that the small cANPs, within the size limits of endocytosis,[317] are internalized by tumor cells after initially penetrating into the tumor. Large cANPs, meanwhile, are able to slowly erode the spheroid collagen and penetrate further into the tumor over time.

5.6. Conclusion

In summary, we have engineered a tumor penetrating albumin nanoparticle capable of adsorbing two therapeutic agents and evaluated its effects on a 3D melanoma tumor spheroid model. Curcumin and riluzole were effectively adsorbed onto the surface of the particles and were as efficacious against human melanoma cells as the drugs in solution. Collagenase, an ECM protease, was conjugated to the drug-loaded particles without compromising the pharmacodynamics of the therapeutics. The presence of collagenase decorating the nanoparticles improved both the ANPs penetration into a multicellular spheroid model and therapeutic benefit. The synthesized nanoparticles could be a useful tool for further investigation of mechanisms of dual drug delivery into the core of a dense tumor mass, improving the efficacy of the associated therapeutic payload.

5.7. Supplementary Figures and Tables

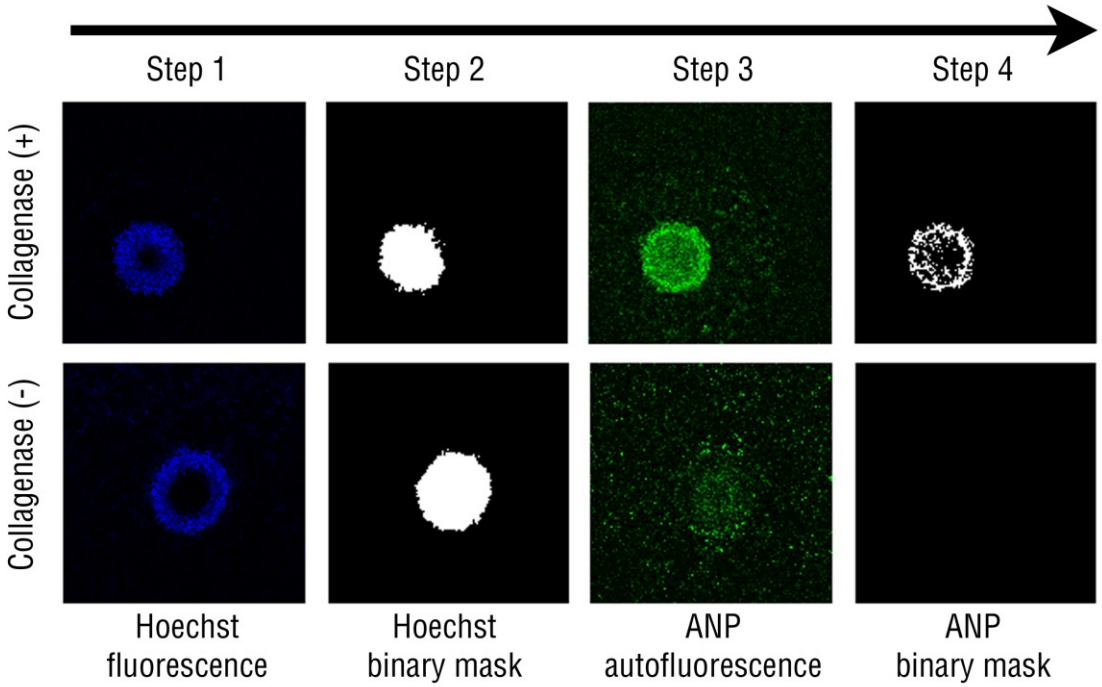

Supplementary Figure S5.1 – Quantification of Nanoparticle Penetration into Spheroids. Flow chart of the processing methodology used to quantify the degree of nanoparticle penetration into spheroids. First, binary masks are created of the spheroid area using Hoechst nuclear stain images (Step 1 to Step 2) and the number of pixels in the mask is determined. Next, background tissue autofluorescence and noise are removed from ANP fluorescence images (Step 3) and the background-corrected ANP images are binarized (Step 4). The number of pixels per area is calculated and the ratio of the two masks is used to quantify nanoparticle association within the spheroid.

ANP formulation	[NaCl] (mM)	Hydrodynamic diameter (nm)	Polydispersity index	Zeta potential (mV)	HSA content (mg ml^{-1})	HSA content (%)
Small	2	96 ± 1	0.03 ± 0.01	-20 ± 1	3.2 ± 0.2	64 ± 3
Large	12	192 ± 2	0.08 ± 0.02	-19 ± 2	2.4 ± 0.2	48 ± 4

Supplementary Table S5.1 – Characterization of ANP Formulations. ANPs were synthesized and characterized at two different sizes by modifying the concentration of NaCl used during synthesis. Both sizes exhibit narrow size distributions and negative zeta potentials in PBS. ± values: standard deviation (n=3)

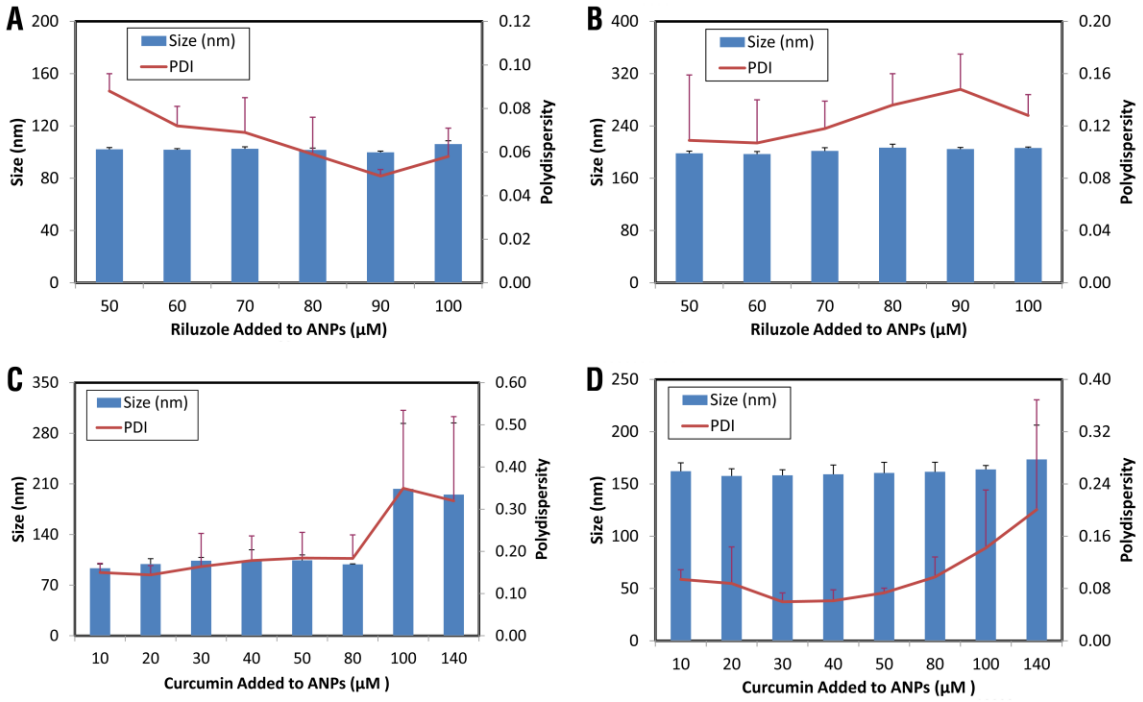

Supplementary Figure S5.2 – Physical Characterization of Single Drug-Loaded ANPs. Size and polydispersity of ANP formulations based on amounts of drug loaded: riluzole loaded small ANPs (A), riluzole loaded large ANPs (B), curcumin loaded small ANPs (C), and curcumin loaded large ANPs (D). Nanoparticle size distribution remains uniform until loading with 120 µM of curcumin. Error bars represent standard deviation for n=3.

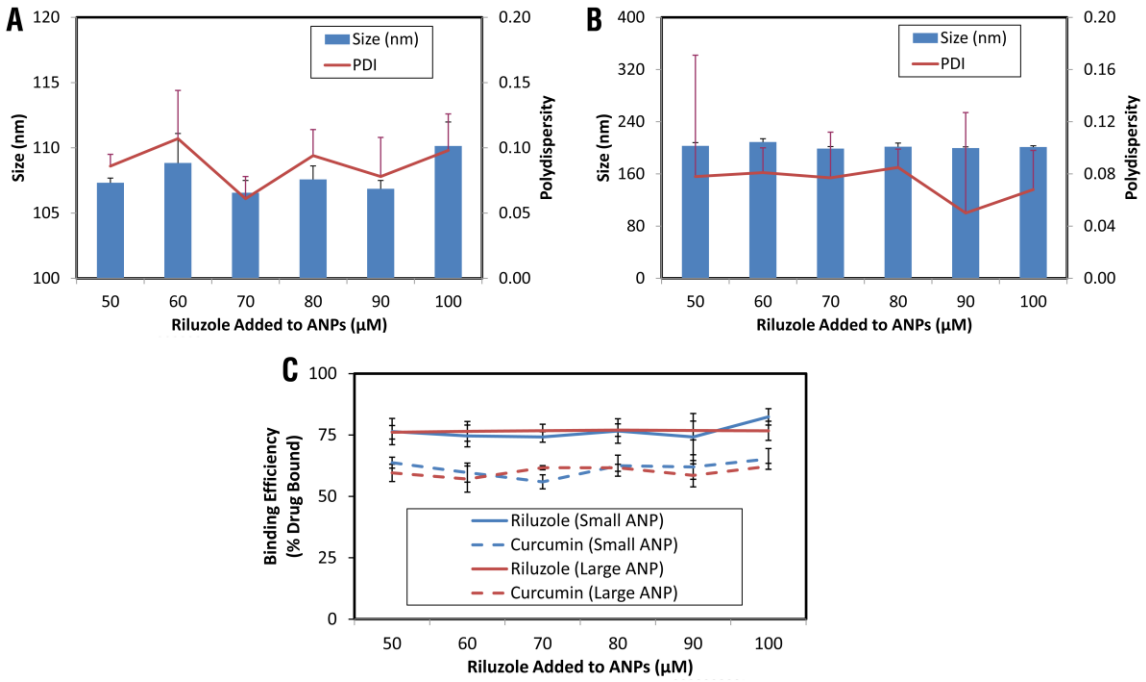

Supplementary Figure S5.3 – Physical Characterization and Binding Efficiency of Dual Drug-Loaded ANPs. Size and polydispersity of dual drug loaded ANPs (80 µM curcumin) as a function of riluzole concentration for small ANPs (A) and large ANPs (B). Binding efficiency for riluzole and curcumin for small and large ANP formulations (C). Error bars represent standard deviation for n=3.

ANP formulation	Collagenase Presence	Riluzole loaded (μM)	Curcumin loaded (μM)	Hydrodynamic diameter (nm)	Polydispersity	Riluzole loading efficiency (%)	Curcumin loading efficiency (%)
Small	+	---	---	107 ± 1	0.06 ± 0.02	---	---
Small	+	20	80	113 ± 3	0.14 ± 0.03	75 ± 5	48 ± 4
Small	+	40	80	113 ± 1	0.11 ± 0.07	74 ± 2	51 ± 6
Small	-	40	80	106 ± 3	0.06 ± 0.01	77 ± 10	55 ± 6
Large	+	---	---	190 ± 1	0.09 ± 0.03	---	---
Large	+	20	80	207 ± 2	0.16 ± 0.08	76 ± 4	52 ± 5
Large	+	40	80	212 ± 2	0.18 ± 0.01	77 ± 3	53 ± 3
Large	-	40	80	196 ± 4	0.13 ± 0.02	77 ± 4	48 ± 4

Supplementary Table S5.2 – Characterization of ANP Formulations. Hydrodynamic diameter, polydispersity and loading efficiency of ANP formulations with and without collagenase incorporation. ± values: standard deviation (n=3)

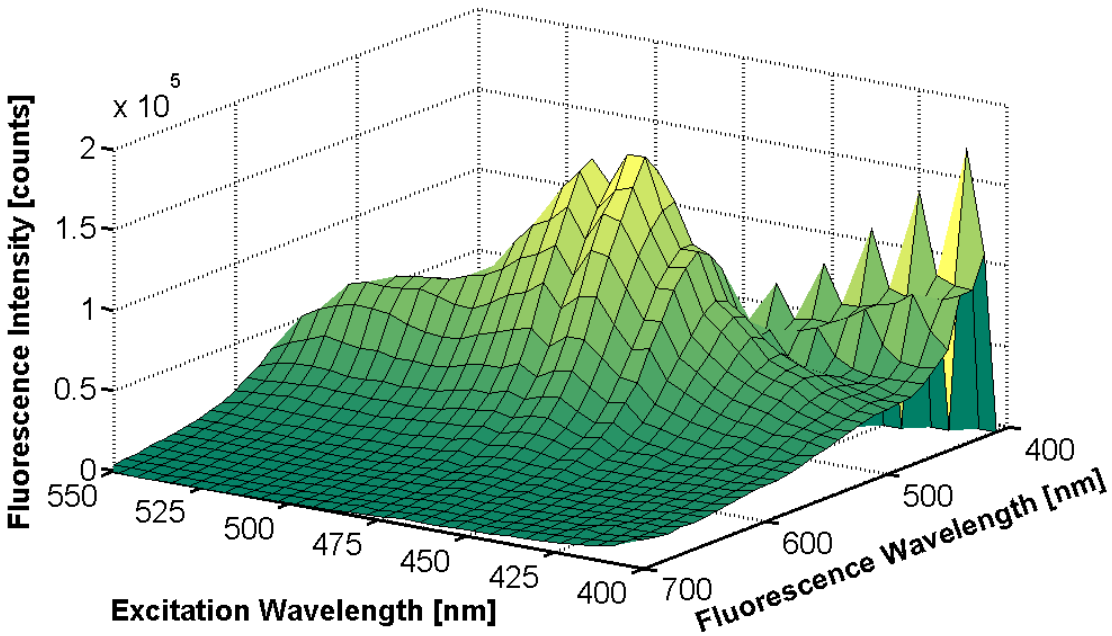

Supplementary Figure S5.4 – ANP Autofluorescence Spectrum. Autofluorescence of ANPs due to glutaraldehyde crosslinks as a function of fluorescence intensity. Maximum excitation at λ=480, broad emission ranging up to λ=550.

CHAPTER 6

RESEARCH SUMMARY AND FUTURE DIRECTIONS

6.1. Dissertation Summary and Conclusions

This dissertation has been focused on the conception and development of innovative nanomaterials for imaging and therapeutic applications. The purpose of this work was to create a multifunctional nanomaterial platform which could have applications toward resolving the progression of disease and improving the effectiveness of therapeutic regimens. Using an engineered design approach, we have formulated a new class of nanoprobes consisting of rare-earth doped nanoparticles (REs) encapsulated in human serum albumin nanocarriers ((RE)ANCs). REs are excited with NIR light and generate both visible and SWIR emissions through upconversion and downconversion fluorescence, respectively. Poor aqueous solubility, lack of functional groups and moderate cytotoxicity challenge the use of REs as synthesized for biological applications. This dissertation has shown that the encapsulation of REs in albumin nanocarriers yields a significant reduction of RE toxicity, an aqueous-dispersible encapsulate and surface groups capable of chemical conjugation for the purpose of disease targeting.

Recently, it has been reported that the limited translation of SWIR-based optical imaging approaches is primarily due to a lack of biocompatible fluorescent probes as well as evidence of SWIR's benefits over conventional NIR probes.[257] We have reported on the first evidence of multi-spectral, real-time short wavelength infrared (SWIR) in vivo imaging using REs and demonstrated their applicability toward disease-targeted imaging.

Our work addresses these challenges and demonstrates the first clinically translatable application of SWIR imaging for identifying tumor growth in vivo using a novel library of REs which have tunable and discrete emissions spanning the entire SWIR window. The novelty of this work is reflected by the previous lack of multispectral

and biomedically-translatable SWIR probes, which can be resolved quickly and safely. For example, our REs can be tailored to emit at specific SWIR wavelengths permitting multispectral imaging of multiple in vivo targets, in contrast to other reported SWIR-emitting biological probes that have very broad and non-specific emissions in the SWIR.[239] Composed of elements with very low toxicity,[250] REs can be visualized using excitation power densities comparable to other SWIR emitting materials but resolved at several fold lower exposure times.[243,244] Furthermore, we have confirmed that RE emissions produce less scattering and better penetration through tissue phantoms than NIR emissions, providing a clear benefit over conventional methods for using SWIR in vivo. These advantages underscore the excellent potential of these nanomaterials for biomedical imaging over other SWIR-emitting compounds.

Crucially, we also present the first demonstration within a pre-clinical model of the potential of SWIR-emitting REs to identify cancerous tissues, while investigating the importance of size and surface properties for effective nanoparticle delivery. The use of SWIR for imaging has been hindered by a lack of commercially available in vivo imaging systems. To address this barrier, we have developed a first-in-class, low-cost, portable SWIR imaging platform concurrently with the fabrication of REs. We have shown that through the simple surface modification of REs with albumin, we can alter the biodistribution, improve the pharmacokinetics and magnify the tumor tissue accumulation of the REs in a transgenic mouse model. Based on these results, we have concluded that our protein modification can alter the bioactivity of the REs, improving their detection sensitivity and SWIR signal amplification at disease sites. In addition, by modulating the thickness of the protein coating, we have explored the importance of

nanoscale diameter and surface chemistry on particle biodistribution. Thus our work offers a possible route for the clinical application of SWIR imaging as well as suggests a potential approach for altering the bioactivity of other inorganic particles, such as quantum dots, magnetic and gold nanoparticles, using FDA-approved albumin.

Finally, we have explored the benefits of modifying albumin nanocarriers with collagenase for improving nanoparticle penetration through ECM-dense tumor tissue. By incorporating an ECM protease into the structure of the protein carriers, we have developed a nanoparticle drug delivery vector which has the reversible-drug binding properties of albumin coupled to the tumor penetrating abilities of collagenase. By using the numerous drug-binding sites available on albumin,[297,318] we were able to sequester and co-deliver multiple therapeutic compounds. Together, the enhancement in protease-mediated tumor penetration and simultaneous delivery of multiple therapeutic compounds results in more effective tumor treatment using albumin nanocarriers. Our results offer a new strategy for engineering advanced drug delivery systems.

We have begun using the nanoprobes as tools to monitor the likelihood of metastatic progression in a transgenic murine melanoma model closely mimicking human melanoma metastasis. By utilizing a spectrum of unique SWIR emissions, we can investigate the critical molecular cues that trigger the occurrence of metastasis and further disease progression. The use of highly sensitive imaging tools that can target and quantify tumor biomarker changes in situ will have broad implications for both patients undergoing new treatment strategies as well as for therapeutic manufacturers during the drug discovery process. The confluence of the biophotonic potential of SWIR-emitting rare earth probes coupled with advances in bionanotechnology can help realize the

promise of such materials as biomedical imaging, diagnostic and theranostic agents.

6.2. Future Directions

6.2.1. Short-Term - Molecular Imaging of Prognostic Cancer Markers Using SWIR

In the short term, the (RE)ANC system developed in Chapter 2 should be extended toward molecular targeting in vivo. Combined with the proof-of-concept multispectral SWIR-imaging presented in Chapter 3, a family of novel nanoprobes with tunable SWIR emission can be developed to investigate the roles that specific cellular markers play in cancer progression and staging. Specifically, we are currently investigating the molecular changes that occur in melanoma using (RE)ANCs with SWIR emissions. This is briefly summarized as follows:

Separate pools of (RE)ANCs will be conjugated with antibodies against each of these four key markers: Grm1 (for metastatic potential), insulin-like growth factor-1 receptor (IGF-1R) (for downstream activation of PI3K-AKT and MAPK pathways and tumor cell survival and proliferation),[319] vascular growth factor receptor (VEGF-R), and chemokine receptor CXCR4. Grm1 has been shown to be aberrantly overexpressed in many of human melanoma cell lines and biopsies.[309] Studies by our collaborator Chen have shown consistently high levels of IGF-R and VEGF-R at sites of metastatic melanoma (Teh and Chen, in preparation). High expression of CXCR4 correlates with high metastasis and poor prognosis of melanoma in terms of survival.[320,321]

To investigate whether the nanoprobes can detect changes in the molecular phenotype of the tumors, the TGS murine model will be imaged following drug treatment and stabilization of tumors. Chen and colleagues have shown that treatment of metabotropic glutamate receptor 1 (Grm1) positive human melanoma xenografts in vitro

and in vivo with an FDA approved glutamate release inhibitor[322] known as Riluzole led to a 50% decrease in tumor growth compared to controls as well as increased apoptosis in tumor biopsies.[323] Previous studies suggest that the disruption of GRM1 signaling in human melanomas may be utilized as a novel therapeutic strategy for the treatment of metastatic melanoma.[323,324] The use of nanoprobes may elucidate the in situ progression of tumor GRM1 expression correlated with other growth and invasiveness markers.

Future studies could endeavor to demonstrate the feasibility of biologically targetable, optical nanoprobes that can be imaged in vivo with (a) deeper penetration than that possible using conventional organic or quantum dot probes and with (b) SWIR emission in a range with lower tissue absorption. Success with the multiplexing of such nanoprobes will further advance the possibility of using such nanoprobes for real-time tracking of disease states and their responsiveness to therapeutic interventions. For example, previous studies suggest that the disruption of GRM1 signaling in human melanomas may be utilized as a novel therapeutic strategy for the treatment of metastatic melanoma.[323,324] The use of nanoprobes may elucidate the in situ progression of tumor GRM1 expression correlated with other growth and invasiveness markers. Similar approaches can be used as a powerful complementary strategy to enable researchers to make decisions on whether to change or refine a treatment, as well as understand the cellular and molecular response to a treatment strategy in real-time.

A few suggested experiments that could yield valuable insights into targeting the nanoprobes involve growing two or more tumor xenografts on a single animal derived from two or more cancer cell lines expressing unique surface receptors. For example, C8161+ human melanoma cells, which express Grm1, can be grown on one flank of the

animal and targeted with Er-doped (RE)ANCs functionalized with anti-Grm1 antibodies. On the other flank, C81-61 Grm1 negative human melanoma cells can be grown. Ho-doped (RE)ANCs functionalized with cRGD could be injected simultaneously to image the $a_v b_3$ integrin which should be expressed on the vasculature of both xenografts. Co-localization of the SWIR signals should be present on the C8161+ xenograft, while the other tumor should only exhibit the Ho-generated SWIR signal.

Another potential approach could be to correlate the spatial position or distribution of the particles with TEM imaging of tumor sections. (RE)ANCs have been shown to provide adequate TEM contrast due to the electron-dense REs. Using this, we have the capability to resolve (RE)ANC location very accurately within a tumor. Although not directly specified in the proposal, the work done in this dissertation with the collagenase-modified albumin nanoparticles could be validated within a tumor model using TEM techniques. Collagenase and unmodified (RE)ANCs could be introduced into a tumor-bearing mouse, imaged and then identified ex vivo through histological examination using TEM. This could be used to determine whether the collagenase improved the penetration of the nanoparticles from the surrounding vasculature and into the dense tumor mass.

6.2.2. Medium-Term - Improving the SWIR Emission Intensity of REs

A critical need that should be addressed for both the above proposal and extension of this dissertation is the limitations posed by the SWIR signal intensity of the RE probes. Ultimately, a combination of parameters, including camera sensitivity and degree of probe accumulation, will determine how easily SWIR signal can be resolved from

multiple SWIR-emitting probes in vivo. Nonetheless, RE formulations in our current library have drastically different optical efficiencies, which can vary by several orders of magnitude from one another (from most to least efficient: Er-, Ho-, Tm-, Pr-dopant schemes). REs doped with Er, for example, can have up to 10-fold better optical efficiencies than Ho-doped particles of a similar size.

Increasing the size of REs has been shown to improve their optical efficiency in a non-linear fashion (personal communications with Dr. Mei Chee Tan). Optimizing the size of newer REs above the 10 nm versions used in this dissertation should be considered for future work. However, as size is a critical parameter in nanoparticle interactions within a biological environment, the impact that changing RE size has on both (RE)ANC formulation and in vivo behavior should be carefully considered.

Alternative strategies could involve changing the host material, changing dopant concentrations, or deposition of other metals to improve optical efficiency.[142,325] Ideally, from an imaging system design standpoint, having probes with comparable emissions would make the simultaneous detection of multiple SWIR wavelengths significantly less challenging.

6.2.3. Medium-Term - Improving SWIR Imaging System and Post-Processing Software

Currently, both the imaging system used to capture SWIR video and the software used to process the raw video are difficult to use when handling a large animal sample size. This limits the amount of data that can be collected in a period of time and significantly delays data analysis.

For the imaging system, upgrading the InGaAs camera to a liquid nitrogen cooled system would potentially improve sensitivity and may help detect lower quantities of nanoprobes in vivo. The InGaAs camera considered should be designed for easy and quick filter installation to detect various SWIR emissions. In addition, we now use a 980 nm collimated laser diode for excitation which can only irradiate a spot ~3 cm in diameter at a time. A laser array source, which can irradiate a whole animal instantaneously and shorten imaging time should be considered instead. Further modifications should consider extending this system for total body scanning and 3-D image reconstruction. A system for inducing anesthesia through inhalation while keeping the animal at a constant temperature should also be considered for long term or repeated imaging studies. Finally, raw video is currently processed using several MATLAB scripts that must each be run and analyzed sequentially. Integrating the scripts into a single software bundle should be implemented to shorten post-processing time.

6.2.4. Medium-term - Comprehensive Investigations of SWIR-Tissue Interactions

Comprehensive studies are needed to determine the actual imaging improvements that can be gained using the SWIR wavelengths generated by the REs. In particular, rigorous experiments should be undertaken to determine the exact penetration depth as well as the reduced scattering and absorbance of SWIR compared to NIR through tissue samples. It may be possible that SWIR has significant benefits in certain tissues compared to NIR. Phantom tissue studies as well as integrating sphere measurements using live samples have already been presented in Chapter 4, but these studies should be expanded upon and pursued further. Understanding the benefits of SWIR and how to

fully exploit these advantages for infrared imaging will aid in the design of future experiments. Furthermore, these types of studies will highlight the importance of SWIR-based imaging approaches and validate our current work.

The optical properties of tissues can be described by the scattering coefficient (μ_s), absorption coefficient (μ_a) and the scattering anisotropy factor (*g*). Calculation of these three parameters can be made by taking reflectance and transmission measurements using an integrating sphere. These calculations can be performed using methods such as the inverse-doubling method,[326] which appears to be the most straightforward, or Monte Carlo simulations.[327] The inverse adding-double method can be used with 1 or more integrating spheres and is very well described by Prahl *et al*.[328]

6.2.5. Medium-Term - Comparison of REs to NIR- and Other SWIR-Emitting Probes

As previous stated,[257] SWIR probes must be compared to traditional NIR probes to aid in their widespread translation. The benefits of SWIR emissions from REs must be directly compared to the NIR emissions of commonly used probes, such as NIR-emitting quantum dots and ICG. In addition, the SWIR emissions from REs should be compared to other SWIR-emitting compounds such as quantum dots and single-walled carbon nanotubes. Directly comparing the optical efficiencies will help determine whether REs are indeed more efficient than other materials at generating SWIR. For both tasks, integrating sphere measurements could potentially be carried out to generate quantifiable and comparable data.

6.2.6. Long-Term - Extension of (RE)ANCs for Multimodal Imaging

The benefits of multimodal imaging have been discussed within Chapter 1. Whole body optical imaging may prove to be very difficult for the immediate future. However, integrating an anatomical imaging component within the (RE)ANCs, such as an MRI contrast agent, could create a nanoparticle that can be resolved at both anatomical and molecular scales. Work has been done triple doping REs with Yb, Er and gadolinium (Gd) III ions to achieve both optical emissions and magnetic resonance properties.[329,330] In addition, monomeric albumin conjugated diethylenetriamine pentaacetic acid (DTPA) to chelate Gd (III) has been extensively studied and may present another avenue of generating MRI contrast.[331] DTPA is a bifunctional chelating agent which contains two amine-reactive anhydride groups that can react with N-terminal and ε-amine groups on albumin.[120] The creation of any Gd(III)-doped nanoparticles would require the necessary testing to confirm that both the MRI contrast as well as SWIR emissions are still generated after modification.

In addition, a potentially exciting opportunity could be to take advantage of the 980 nm NIR absorbance of the (RE)ANCs to generate 3-D images in vivo. Photoacoustic imaging is a hybrid modality that uses an optical pulse to generate an acoustic signal which can be registered by ultrasound devices. This technique combines both the sensitivity of optical imaging with the high spatial resolution provided by acoustic techniques such as ultrasound. Furthermore, 3-D mapping and localization of the particles within a tumor could be accomplished with photoacoustic imaging as well. Photoacoustic imaging relies on the excitation of a contrast agent with a pulse of laser light. Once excited, the contrast agents produce very low amounts of heat which in turn

generate a thermoelastic expansion resulting in a measureable ultrasound wave.[332] The benefit in this approach is that no further modifications are needed to image the current nanoparticle formulation with photoacoustic techniques. This technique could be used to create maps of vasculature or determine the spatial position of the (RE)ANCs within a tumor.

6.2.7. Long-Term - Intraoperative Use of Multimodal (RE)ANCs for Deep Tissue Tumor Resection

A potential application of (RE)ANCs with MRI contrast could be for intraoperative use. Studies have been published using other targeted multimodal nanoparticles for determining the anatomical position of tumors using MRI approaches, followed by optical imaging to guide surgical intervention.[35] With molecular targeting, SWIR imaging could then be used to delineate tumor margins in order to ensure successful surgical resection of the tumor.[33]

The current in vivo melanoma model used in this dissertation focused on superficial disease states. Future models should be considered looking at deeper cancers such as prostate, colon or breast. Alternatively, a separate project could be undertaken for imaging atherosclerotic lesions given the resources available in the Moghe lab.

6.2.8. Long-Term - Stimuli-Sensitive Therapeutic Drug Delivery

Exploiting the emissions of the REs for more than imaging is another potential approach for developing the (RE)ANCs into advanced drug delivery agents. Photosensitive linkers, such as 5-(3-iodopropoxy)-2-nitrobenzyl alcohol (IDNA),[333]could

be used to conjugate therapeutics, such as curcumin, to the nanoparticles. The upconverted visible emissions of the REs could then be used to release the drug from the bound particle at a site of interest, such as a tumor. IDNA, for example, cleaves when exposed to 570 nm light which is near the visible emissions of the Er-, Ho- and Pr-doped REs.

In addition, photodynamic therapy (PDT) could also be attempted in a similar manner. PDT relies on the excitation of small molecules, known as photosensitizers, to generate reactive oxygen species (ROS). ROS can cause significant cellular damage when in proximity to tissue. Photosensitizers, such as methylene blue, could be attached to REs then delivered via (RE)ANCs to tumor sites. Once there, excitation of the REs with NIR will generate visible light, which could be used to trigger the generation of ROS from the photosensitizer resulting in a therapeutic effect.

CHAPTER 7

REFERENCES

1. Merlo, L.M.F., Pepper, J.W., Reid, B.J. & Maley, C.C. Cancer as an evolutionary and ecological process. *Nature Reviews Cancer* **6**, 924-935 (2006).
2. Sotiriou, C. & Piccart, M.J. Opinion - Taking gene-expression profiling to the clinic: when will molecular signatures become relevant to patient care? *Nature Reviews Cancer* **7**, 545-553 (2007).
3. Looking back on the millennium in medicine. *N. Engl. J. Med.* **342**, 42-49 (2000).
4. Weissleder, R. & Pittet, M.J. Imaging in the era of molecular oncology. *Nature* **452**, 580-589 (2008).
5. Brindle, K. New approaches for imaging tumour responses to treatment. *Nat. Rev. Cancer* **8**, 94-107 (2008).
6. Willmann, J.K., van Bruggen, N., Dinkelborg, L.M. & Gambhir, S.S. Molecular imaging in drug development. *Nature Reviews Drug Discovery* **7**, 591-607 (2008).
7. Weissleder, R. Molecular imaging in cancer. *Science* **312**, 1168-1171 (2006).
8. Yang, Y. & Czernin, J. Contribution of Imaging to Cancer Care Costs. *J. Nucl. Med.* **52**, 86s-92s (2011).
9. Dinan, M.A.*, et al.* Changes in the Use and Costs of Diagnostic Imaging Among Medicare Beneficiaries With Cancer, 1999-2006. *Jama-J Am Med Assoc* **303**, 1625-1631 (2010).
10. Kelloff, G.J., Choyke, P., Coffey, D.S. & Grp, P.C.I.W. Challenges in Clinical Prostate Cancer: Role of Imaging. *Am. J. Roentgenol.* **192**, 1455-1470 (2009).
11. Frangioni, J.V. New technologies for human cancer imaging. *J. Clin. Oncol.* **26**, 4012-4021 (2008).
12. Frangioni, J.V. Translating in vivo diagnostics into clinical reality. *Nat. Biotechnol.* **24**, 909-913 (2006).
13. Mitchell, J.M. & LaGalia, R.R. Controlling the Escalating Use of Advanced Imaging The Role of Radiology Benefit Management Programs. *Med. Care Res. Rev.* **66**, 339-351 (2009).
14. Mueller, P.R., Biswal, S., Halpern, E.F., Kaufman, J.A. & Lee, M.J. Interventional radiologic procedures: Patient anxiety, perception of pain, understanding of procedure, and satisfaction with medication - A prospective study. *Radiology* **215**, 684-688 (2000).
15. Verboom, P.*, et al.* Cost-effectiveness of FDG-PET in staging non-small cell lung cancer: the PLUS study. *Eur. J. Nucl. Med. Mol. Imaging* **30**, 1444-1449 (2003).
16. Fischer, B.*, et al.* Preoperative Staging of Lung Cancer with Combined PET-CT. *N. Engl. J. Med.* **361**, 32-39 (2009).
17. Sogaard, R., Fischer, B.M.B., Mortensen, J., Hojgaard, L. & Lassen, U. Preoperative staging of lung cancer with PET/CT: cost-effectiveness evaluation alongside a randomized controlled trial. *Eur. J. Nucl. Med. Mol. Imaging* **38**, 802-809 (2011).
18. van Tinteren, H.*, et al.* Effectiveness of positron emission tomography in the preoperative assessment of patients with suspected non-small-cell lung cancer: the PLUS multicentre randomised trial. *Lancet* **359**, 1388-1392 (2002).

19. Jelinek, J.S., *et al.* Diagnosis of primary bone tumors with image-guided percutaneous biopsy: Experience with 110 tumors. *Radiology* **223**, 731-737 (2002).
20. Schreyogg, J., *et al.* Cost-Effectiveness of Hybrid PET/CT for Staging of Non-Small Cell Lung Cancer. *J. Nucl. Med.* **51**, 1668-1675 (2010).
21. Wang, X., Yang, L., Chen, Z.G. & Shin, D.M. Application of nanotechnology in cancer therapy and imaging. *CA Cancer J Clin* **58**, 97-110 (2008).
22. Etzioni, R., *et al.* The case for early detection. *Nat Rev Cancer* **3**, 243-252 (2003).
23. Weissleder, R. & Pittet, M.J. Imaging in the era of molecular oncology. *Nature* **452**, 580-589 (2008).
24. Rudin, M. & Weissleder, R. Molecular imaging in drug discovery and development. *Nature Reviews Drug Discovery* **2**, 123-131 (2003).
25. Ferrara, K., Pollard, R. & Borden, M. Ultrasound microbubble contrast agents: Fundamentals and application to gene and drug delivery. *Annu. Rev. Biomed. Eng.* **9**, 415-447 (2007).
26. Zaremba, L.A. Guidance for industry and FDA staff: Criteria for significant risk investigations of magnetic resonance diagnostic devices. *US Department of Health and Human Services, Food and Drug Administration* **14**(2003).
27. Formica, D. & Silvestri, S. Biological effects of exposure to magnetic resonance imaging: an overview. *BioMedical Engineering OnLine* **3**, 11 (2004).
28. Wink, M.H., Wijkstra, H., De la Rosette, J.J.M.C.H. & Grimbergen, C.A. Ultrasound imaging and contrast agents: A safe alternative to MRI? *Minimally Invasive Therapy & Allied Technologies* **15**, 93-100 (2006).
29. Massoud, T.F. & Gambhir, S.S. Molecular imaging in living subjects: seeing fundamental biological processes in a new light. *Genes Dev.* **17**, 545-580 (2003).
30. Sosnovik, D.E. & Weissleder, R. Emerging concepts in molecular MRI. *Curr. Opin. Biotechnol.* **18**, 4-10 (2007).
31. Bremer, C., Ntziachristos, V. & Weissleder, R. Optical-based molecular imaging: contrast agents and potential medical applications. *Eur. Radiol.* **13**, 231-243 (2003).
32. Kaijzel, E.L., van der Pluijm, G. & Lowik, C.W.G.M. Whole-body optical Imaging in animal models to assess cancer development and progression. *Clin. Cancer Res.* **13**, 3490-3497 (2007).
33. Kircher, M.F., *et al.* A brain tumor molecular imaging strategy using a new triple-modality MRI-photoacoustic-Raman nanoparticle. *Nature Medicine* **18**, 829-U235 (2012).
34. Kim, J., Piao, Y. & Hyeon, T. Multifunctional nanostructured materials for multimodal imaging, and simultaneous imaging and therapy. *Chem. Soc. Rev.* **38**, 372-390 (2009).
35. Kircher, M.F., Mahmood, U., King, R.S., Weissleder, R. & Josephson, L. A multimodal nanoparticle for preoperative magnetic resonance imaging and intraoperative optical brain tumor delineation. *Cancer Res.* **63**, 8122-8125 (2003).
36. Nahrendorf, M., *et al.* Hybrid PET-optical imaging using targeted probes. *Proc. Natl. Acad. Sci. U. S. A.* **107**, 7910-7915 (2010).

37. Czernin, J., Allen-Auerbach, M. & Schelbert, H.R. Improvements in cancer staging with PET/CT: Literature-based evidence as of September 2006. *J. Nucl. Med.* **48**, 78s-88s (2007).
38. Antoch, G.*, et al.* Whole-body dual-modality PET/CT and whole-body MRI for tumor staging in oncology. *Jama-J Am Med Assoc* **290**, 3199-3206 (2003).
39. Gerth, H.U.*, et al.* Significant benefit of multimodal imaging: PET/CT compared with PET alone in staging and follow-up of patients with Ewing tumors. *J. Nucl. Med.* **48**, 1932-1939 (2007).
40. Scarfone, C.*, et al.* Prospective feasibility trial of radiotherapy target definition for head and neck cancer using 3-dimensional PET and CT imaging. *Journal of Nuclear Medicine* **45**, 543-552 (2004).
41. Gregoire, V., Haustermans, K., Geets, X., Roels, S. & Lonneux, M. PET-based treatment planning in radiotherapy: A new standard? *Journal of Nuclear Medicine* **48**, 68s-77s (2007).
42. Ahn, P.H.*, et al.* PET-CT in treatment planning position for head and neck radiation with IMRT and trend toward improved regional control. *International Journal of Radiation Oncology Biology Physics* **72**, S416-S416 (2008).
43. Weber, W.A. & Figlin, R. Monitoring cancer treatment with PET/CT: Does it make a difference? *Journal of Nuclear Medicine* **48**, 36s-44s (2007).
44. Ell, P.J. The contribution of PET/CT to improved patient management. *Br. J. Radiol.* **79**, 32-36 (2006).
45. Yankeelov, T.E. & Gore, J.C. Has Quantitative Multimodal Imaging of Treatment Response Arrived? *Clin. Cancer Res.* **15**, 6473-6475 (2009).
46. O'Connor, J.P.B.*, et al.* Quantifying Antivascular Effects of Monoclonal Antibodies to Vascular Endothelial Growth Factor: Insights from Imaging. *Clin. Cancer Res.* **15**, 6674-6682 (2009).
47. Neves, A.A. & Brindle, K.M. Assessing responses to cancer therapy using molecular imaging. *Biochimica Et Biophysica Acta-Reviews on Cancer* **1766**, 242-261 (2006).
48. Azar, F.S. & Intes, X. *Translational Multimodality Optical Imaging*, (Artech House, 2008).
49. Weissleder, R. A clearer vision for in vivo imaging. *Nat. Biotechnol.* **19**, 316-317 (2001).
50. Frangioni, J.V. In vivo near-infrared fluorescence imaging. *Curr. Opin. Chem. Biol.* **7**, 626-634 (2003).
51. Ntziachristos, V., Ripoll, J., Wang, L.H.V. & Weissleder, R. Looking and listening to light: the evolution of whole-body photonic imaging. *Nature Biotechnology* **23**, 313-320 (2005).
52. Welch, A.J. The Thermal Response of Laser Irradiated Tissue. *IEEE J. Quantum Electron.* **20**, 1471-1481 (1984).
53. Anderson, R.R. & Ross, E.V. Laser-tissue interactions. *Cutaneous Laser Surgery. Mosby: Philadelphia, PA* **9**(1994).
54. Graves, E.E., Weissleder, R. & Ntziachristos, V. Fluorescence molecular imaging of small animal tumor models. *Curr. Mol. Med.* **4**, 419-430 (2004).

55. Culver, J., Akers, W. & Achilefu, S. Multimodality molecular imaging with combined optical and SPECT/PET modalities. *Journal of Nuclear Medicine* **49**, 169-172 (2008).
56. Kiesslich, R.*, et al.* Confocal laser endoscopy for diagnosing intraepithelial neoplasias and colorectal cancer in vivo. *Gastroenterology* **127**, 706-713 (2004).
57. Kiesslich, R.*, et al.* In vivo histology of Barrett's esophagus and associated neoplasia by confocal laser endomicroscopy. *Clin. Gastroenterol. Hepatol.* **4**, 979-987 (2006).
58. Ntziachristos, V., Bremer, C., Graves, E.E., Ripoll, J. & Weissleder, R. In vivo tomographic imaging of near-infrared fluorescent probes. *Molecular imaging* **1**, 82-88 (2002).
59. Prasad, P.N. Introduction. in *Introduction to Biophotonics* 1-10 (John Wiley & Sons, Inc., 2004).
60. Lakowicz, J.R. *Principles of Fluorescence Spectroscopy*, (Springer, 2006).
61. Hale, G.M. & Querry, M.R. Optical Constants of Water in the 200-nm to 200-µm Wavelength Region. *Appl. Opt.* **12**, 555-563 (1973).
62. Cope, M. The application of near infrared spectroscopy to non invasive monitoring of cerebral oxygenation in the newborn infant. *Department of Medical Physics and Bioengineering, University College London*, 214-219 (1991).
63. Conway, J.M., Norris, K.H. & Bodwell, C.E. A New Approach for the Estimation of Body-Composition - Infrared Interactance. *Am. J. Clin. Nutr.* **40**, 1123-1130 (1984).
64. Huang, Z.W.*, et al.* Cutaneous melanin exhibiting fluorescence emission under near-infrared light excitation. *J. Biomed. Opt.* **11**(2006).
65. Billinton, N. & Knight, A.W. Seeing the wood through the trees: A review of techniques for distinguishing green fluorescent protein from endogenous autofluorescence. *Anal. Biochem.* **291**, 175-197 (2001).
66. Troy, T., Jekic-McMullen, D., Sambucetti, L. & Rice, B. Quantitative Comparison of the Sensitivity of Detection of Fluorescent and Bioluminescent Reporters in Animal Models. *Molecular imaging* **3**, 9-23 (2004).
67. Frangioni, J.V. In vivo near-infrared fluorescence imaging. *Curr Opin Chem Biol* **7**, 626-634 (2003).
68. Beuthan, J., Minet, O., Helfmann, J., Herrig, M. & Muller, G. The spatial variation of the refractive index in biological cells. *Phys. Med. Biol.* **41**, 369-382 (1996).
69. Backman, V.*, et al.* Polarized light scattering spectroscopy for quantitative measurement of epithelial cellular structures in situ. *IEEE J. Sel. Top. Quantum Electron.* **5**, 1019-1026 (1999).
70. Keren, S.*, et al.* Noninvasive molecular imaging of small living subjects using Raman spectroscopy. *Proc. Natl. Acad. Sci. U. S. A.* **105**, 5844-5849 (2008).
71. Faulds, K., Barbagallo, R.P., Keer, J.T., Smith, W.E. & Graham, D. SERRS as a more sensitive technique for the detection of labelled oligonucleotides compared to fluorescence. *Analyst* **129**, 567-568 (2004).
72. Lim, Y.T.*, et al.* Selection of quantum dot wavelengths for biomedical assays and imaging. *Mol Imaging* **2**, 50-64 (2003).

73. Bicout, D., Brosseau, C., Martinez, A.S. & Schmitt, J.M. Depolarization of Multiply Scattered Waves by Spherical Diffusers - Influence of the Size Parameter. *Phys Rev E* **49**, 1767-1770 (1994).
74. Pierce, M.C., Javier, D.J. & Richards-Kortum, R. Optical contrast agents and imaging systems for detection and diagnosis of cancer. *International Journal of Cancer* **123**, 1979-1990 (2008).
75. Hopton, P., Walsh, T.S. & Lee, A. Measurement of cerebral blood volume using near-infrared spectroscopy and indocyanine green elimination. *J. Appl. Physiol.* **87**, 1981-1987 (1999).
76. Park, K.*, et al.* New Generation of Multifunctional Nanoparticles for Cancer Imaging and Therapy. *Adv. Funct. Mater.* **19**, 1553-1566 (2009).
77. Gradishar, W.J.*, et al.* Phase III trial of nanoparticle albumin-bound paclitaxel compared with polyethylated castor oil-based paclitaxel in women with breast cancer. *J. Clin. Oncol.* **23**, 7794-7803 (2005).
78. Bhatt, R.*, et al.* Synthesis and in vivo antitumor activity of poly(l-glutamic acid) conjugates of 20S-camptothecin. *J. Med. Chem.* **46**, 190-193 (2003).
79. Markman, M. Pegylated liposomal doxorubicin in the treatment of cancers of the breast and ovary. *Expert Opin. Pharmacother.* **7**, 1469-1474 (2006).
80. Flenniken, M.L.*, et al.* Melanoma and lymphocyte cell-specific targeting incorporated into a heat shock protein cage architecture. *Chem. Biol.* **13**, 161-170 (2006).
81. Pastorin, G.*, et al.* Double functionalization of carbon nanotubes for multimodal drug delivery. *Chem. Commun. (Camb.)*, 1182-1184 (2006).
82. Cho, Y.W.*, et al.* In vivo tumor targeting and radionuclide imaging with self-assembled nanoparticles: mechanisms, key factors, and their implications. *Biomaterials* **28**, 1236-1247 (2007).
83. Debbage, P. & Jaschke, W. Molecular imaging with nanoparticles: giant roles for dwarf actors. *Histochem. Cell Biol.* **130**, 845-875 (2008).
84. Davis, M.E., Chen, Z. & Shin, D.M. Nanoparticle therapeutics: an emerging treatment modality for cancer. *Nature Reviews Drug Discovery* **7**, 771-782 (2008).
85. Gratton, S.E.A.*, et al.* The effect of particle design on cellular internalization pathways. *Proceedings of the National Academy of Sciences of the United States of America* **105**, 11613-11618 (2008).
86. Chithrani, B.D., Ghazani, A.A. & Chan, W.C.W. Determining the size and shape dependence of gold nanoparticle uptake into mammalian cells. *Nano Letters* **6**, 662-668 (2006).
87. Verma, A. & Stellacci, F. Effect of Surface Properties on Nanoparticle-Cell Interactions. *Small* **6**, 12-21 (2010).
88. Iyer, A.K., Khaled, G., Fang, J. & Maeda, H. Exploiting the enhanced permeability and retention effect for tumor targeting. *Drug Discov. Today* **11**, 812-818 (2006).
89. Yuan, F.*, et al.* Vascular-Permeability in a Human Tumor Xenograft - Molecular-Size Dependence and Cutoff Size. *Cancer Res.* **55**, 3752-3756 (1995).

90. Couvreur, P. & Vauthier, C. Nanotechnology: Intelligent design to treat complex disease. *Pharm. Res.* **23**, 1417-1450 (2006).
91. Hobbs, S.K.*, et al.* Regulation of transport pathways in tumor vessels: role of tumor type and microenvironment. *Proc. Natl. Acad. Sci. U. S. A.* **95**, 4607-4612 (1998).
92. Torchilin, V.P. Recent advances with liposomes as pharmaceutical carriers. *Nat. Rev. Drug Discov.* **4**, 145-160 (2005).
93. Nomura, T., Koreeda, N., Yamashita, F., Takakura, Y. & Hashida, M. Effect of particle size and charge on the disposition of lipid carriers after intratumoral injection into tissue-isolated tumors. *Pharm. Res.* **15**, 128-132 (1998).
94. Hu-Lieskovan, S., Heidel, J.D., Bartlett, D.W., Davis, M.E. & Triche, T.J. Sequence-specific knockdown of EWS-FLI1 by targeted, nonviral delivery of small interfering RNA inhibits tumor growth in a murine model of metastatic Ewing's sarcoma. *Cancer Res.* **65**, 8984-8992 (2005).
95. Sperling, R.A. & Parak, W.J. Surface modification, functionalization and bioconjugation of colloidal inorganic nanoparticles. *Philosophical Transactions of the Royal Society a-Mathematical Physical and Engineering Sciences* **368**, 1333-1383 (2010).
96. Moghimi, S.M., Hunter, A.C. & Murray, J.C. Long-circulating and target-specific nanoparticles: Theory to practice. *Pharmacol. Rev.* **53**, 283-318 (2001).
97. Choi, H.S.*, et al.* Design considerations for tumour-targeted nanoparticles. *Nat. Nanotechnol.* **5**, 42-47 (2010).
98. Montet, X., Funovics, M., Montet-Abou, K., Weissleder, R. & Josephson, L. Multivalent effects of RGD peptides obtained by nanoparticle display. *J. Med. Chem.* **49**, 6087-6093 (2006).
99. Davis, M.E.*, et al.* Evidence of RNAi in humans from systemically administered siRNA via targeted nanoparticles. *Nature* **464**, 1067-U1140 (2010).
100. Boswell, C.A. & Brechbiel, M.W. Development of radioimmunotherapeutic and diagnostic antibodies: an inside-out view. *Nucl. Med. Biol.* **34**, 757-778 (2007).
101. Tolmachev, V.*, et al.* Affibody molecules: potential for in vivo imaging of molecular targets for cancer therapy. *Expert Opin. Biol. Ther.* **7**, 555-568 (2007).
102. Hong, S.*, et al.* The binding avidity of a nanoparticle-based multivalent targeted drug delivery platform. *Chem. Biol.* **14**, 107-115 (2007).
103. Mammen, M., Choi, S.K. & Whitesides, G.M. Polyvalent interactions in biological systems: Implications for design and use of multivalent ligands and inhibitors. *Angewandte Chemie-International Edition* **37**, 2755-2794 (1998).
104. Peer, D.*, et al.* Nanocarriers as an emerging platform for cancer therapy. *Nat. Nanotechnol.* **2**, 751-760 (2007).
105. Ruoslahti, E., Bhatia, S.N. & Sailor, M.J. Targeting of drugs and nanoparticles to tumors. *J. Cell Biol.* **188**, 759-768 (2010).
106. Li, M.H.*, et al.* Dendrimer-based multivalent methotrexates as dual acting nanoconjugates for cancer cell targeting. *Eur. J. Med. Chem.* **47**, 560-572 (2012).
107. Wolfenden, M.L. & Cloninger, M.J. Mannose/glucose-functionalized dendrimers to investigate the predictable tunability of multivalent interactions. *J. Am. Chem. Soc.* **127**, 12168-12169 (2005).

108. Minchinton, A.I. & Tannock, I.F. Drug penetration in solid tumours. *Nature Reviews Cancer* **6**, 583-592 (2006).
109. Waite, C.L. & Roth, C.M. PAMAM-RGD Conjugates Enhance siRNA Delivery Through a Multicellular Spheroid Model of Malignant Glioma. *Bioconjugate Chemistry* **20**, 1908-1916 (2009).
110. Kranenborg, M.H.G.C.*, et al.* Two-step radio-immunotargeting of renal-cell carcinoma xenografts in nude mice with anti-renal-cell-carcinoma X anti-DTPA bispecific monoclonal antibodies. *Int. J. Cancer* **75**, 74-80 (1998).
111. Juweid, M.*, et al.* Micropharmacology of Monoclonal-Antibodies in Solid Tumors - Direct Experimental-Evidence for a Binding-Site Barrier. *Cancer Res.* **52**, 5144-5153 (1992).
112. Adams, G.P.*, et al.* High affinity restricts the localization and tumor penetration of single-chain Fv antibody molecules. *Cancer Res.* **61**, 4750-4755 (2001).
113. Perrault, S.D. & Chan, W.C.W. In vivo assembly of nanoparticle components to improve targeted cancer imaging. *Proc. Natl. Acad. Sci. U. S. A.* **107**, 11194-11199 (2010).
114. Simberg, D.*, et al.* Biomimetic amplification of nanoparticle homing to tumors. *Proc. Natl. Acad. Sci. U. S. A.* **104**, 932-936 (2007).
115. von Maltzahn, G.*, et al.* Nanoparticles that communicate in vivo to amplify tumour targeting. *Nat. Mater.* **10**, 545-552 (2011).
116. Sugahara, K.N.*, et al.* Tissue-Penetrating Delivery of Compounds and Nanoparticles into Tumors. *Cancer Cell* **16**, 510-520 (2009).
117. Wang, L.J.*, et al.* Improving Tumor-Targeting Capability and Pharmacokinetics of Tc-99m-Labeled Cyclic RGD Dimers with PEG(4) Linkers. *Mol. Pharm.* **6**, 231-245 (2009).
118. Garanger, E., Boturyn, D., Coll, J.L., Favrot, M.C. & Dumy, P. Multivalent RGD synthetic peptides as potent alpha(V)beta(3) integrin ligands. *Org. Biomol. Chem.* **4**, 1958-1965 (2006).
119. Singh, N., Agrawal, A., Leung, A.K.L., Sharp, P.A. & Bhatia, S.N. Effect of Nanoparticle Conjugation on Gene Silencing by RNA Interference. *J. Am. Chem. Soc.* **132**, 8241-+ (2010).
120. Hermanson, G.T. *Bioconjugate Techniques*, (Academic Press, 2008).
121. Schuette, C.G.*, et al.* Determinants of liposome fusion mediated by synaptic SNARE proteins. *Proceedings of the National Academy of Sciences of the United States of America* **101**, 2858-2863 (2004).
122. Kukowska-Latallo, J.F.*, et al.* Nanoparticle targeting of anticancer drug improves therapeutic response in animal model of human epithelial cancer. *Cancer Res.* **65**, 5317-5324 (2005).
123. Geng, Y.*, et al.* Shape effects of filaments versus spherical particles in flow and drug delivery. *Nature Nanotechnology* **2**, 249-255 (2007).
124. Huang, X.H., El-Sayed, I.H., Qian, W. & El-Sayed, M.A. Cancer cell imaging and photothermal therapy in the near-infrared region by using gold nanorods. *Journal of the American Chemical Society* **128**, 2115-2120 (2006).

125. Liu, Z., *et al.* Multiplexed Five-Color Molecular Imaging of Cancer Cells and Tumor Tissues with Carbon Nanotube Raman Tags in the Near-Infrared. *Nano Research* **3**, 222-233 (2010).
126. Cherukuri, P., Bachilo, S.M., Litovsky, S.H. & Weisman, R.B. Near-infrared fluorescence microscopy of single-walled carbon nanotubes in phagocytic cells. *Journal of the American Chemical Society* **126**, 15638-15639 (2004).
127. Gao, X.H., Cui, Y.Y., Levenson, R.M., Chung, L.W.K. & Nie, S.M. In vivo cancer targeting and imaging with semiconductor quantum dots. *Nature Biotechnology* **22**, 969-976 (2004).
128. Naczynski, D.J., *et al.* Albumin nanoshell encapsulation of near-infrared-excitable rare-earth nanoparticles enhances biocompatibility and enables targeted cell imaging. *Small* **6**, 1631-1640 (2010).
129. van de Rijke, F., *et al.* Up-converting phosphor reporters for nucleic acid microarrays. *Nat. Biotechnol.* **19**, 273-276 (2001).
130. Zako, T., *et al.* Development of Near Infrared-Fluorescent Nanophosphors and Applications for Cancer Diagnosis and Therapy. *Journal of Nanomaterials* (2010).
131. Yi, G.S., *et al.* Synthesis, characterization, and biological application of size-controlled nanocrystalline NaYF4 : Yb,Er infrared-to-visible up-conversion phosphors. *Nano Lett.* **4**, 2191-2196 (2004).
132. Boyer, J.C., Vetrone, F., Cuccia, L.A. & Capobianco, J.A. Synthesis of colloidal upconverting NaYF4 nanocrystals doped with Er3+, Yb3+ and Tm3+, Yb3+ via thermal decomposition of lanthanide trifluoroacetate precursors. *J. Am. Chem. Soc.* **128**, 7444-7445 (2006).
133. Yi, G.S., *et al.* Synthesis and characterization of high-efficiency nanocrystal up-conversion phosphors: Ytterbium and erbium codoped lanthanum molybdate. *Chem. Mater.* **14**, 2910-2914 (2002).
134. Zeng, J.H., Su, J., Li, Z.H., Yan, R.X. & Li, Y.D. Synthesis and upconversion luminescence of hexagonal-phase NaYF4 : Yb, Er3+, phosphors of controlled size and morphology. *Advanced Materials* **17**, 2119-+ (2005).
135. Heer, S., Kompe, K., Gudel, H.U. & Haase, M. Highly efficient multicolour upconversion emission in transparent colloids of lanthanide-doped NaYF4 nanocrystals. *Advanced Materials* **16**, 2102-+ (2004).
136. Mai, H.X., Zhang, Y.W., Sun, L.D. & Yan, C.R. Size- and phase-controlled synthesis of monodisperse NaYF4 : Yb,Er nanocrystals from a unique delayed nucleation pathway monitored with upconversion spectroscopy. *J. Phys. Chem. C* **111**, 13730-13739 (2007).
137. Zhang, F., *et al.* Uniform nanostructured arrays of sodium rare-earth fluorides for highly efficient multicolor upconversion luminescence. *Angewandte Chemie-International Edition* **46**, 7976-7979 (2007).
138. Li, C., *et al.* Different Microstructures of β-NaYF4 Fabricated by Hydrothermal Process: Effects of pH Values and Fluoride Sources. *ChemInform* **38**, no-no (2007).

139. Fan, X.P., Pi, D.B., Wang, F., Qiu, J.R. & Wang, M.Q. Hydrothermal synthesis and luminescence behavior of lanthanide-doped GdF3 nanoparticles. *Ieee Transactions on Nanotechnology* **5**, 123-128 (2006).
140. Chen, J. & Zhao, J.X. Upconversion Nanomaterials: Synthesis, Mechanism, and Applications in Sensing. *Sensors* **12**, 2414-2435 (2012).
141. Auzel, F. Upconversion and anti-stokes processes with f and d ions in solids. *Chem. Rev.* **104**, 139-173 (2004).
142. Wang, F. & Liu, X.G. Recent advances in the chemistry of lanthanide-doped upconversion nanocrystals. *Chem. Soc. Rev.* **38**, 976-989 (2009).
143. Blasse, G. & Grabmaier, B.C. *Luminescent materials : with 31 tables*, (Springer, Berlin; Heidelberg [u.a.], 1994).
144. Yi, G.S. & Chow, G.M. Water-soluble NaYF4 : Yb,Er(Tm)/NaYF4/polymer core/shell/shell nanoparticles with significant enhancement of upconversion fluorescence. *Chem. Mater.* **19**, 341-343 (2007).
145. Prasad, P.N. Plasmonics. in *Nanophotonics* 129-151 (John Wiley & Sons, Inc., 2004).
146. Nyk, M., Kumar, R., Ohulchanskyy, T.Y., Bergey, E.J. & Prasad, P.N. High Contrast in Vitro and in Vivo Photoluminescence Bioimaging Using Near Infrared to Near Infrared Up-Conversion in TM3+ and Yb3+ Doped Fluoride Nanophosphors. *Nano Lett.* **8**, 3834-3838 (2008).
147. Kumar, G.A., Chen, C.W., Ballato, J. & Riman, R.E. Optical characterization of infrared emitting rare-earth-doped fluoride nanocrystals and their transparent nanocomposites. *Chem. Mater.* **19**, 1523-1528 (2007).
148. Ballato, O., Riman, R.E. & Snitzer, E. Sol-gel synthesis of rare-earth-doped lanthanum halides for highly efficient 1.3-mu m optical amplification. *Opt. Lett.* **22**, 691-693 (1997).
149. Singh, V.*, et al.* Infrared emissions, visible up-conversion, thermoluminescence and defect centres in Er3Al5O12 phosphor obtained by solution combustion reaction. *Applied Physics B-Lasers and Optics* **101**, 631-638 (2010).
150. Powell, R.C. *Physics of Solid-State Laser Materials*, (AIP Press/Springer, 1998).
151. Sudo, S. *Optical Fiber Amplifiers: Materials, Devices, and Applications*, (Artech House, 1997).
152. Manseau, M.P. Lanthanides-based upconverting biolabels in the near-infrared. *Department of Chemistry, University of Victoria* (2009).
153. Kreuter, J. Nanoparticles--a historical perspective. *Int. J. Pharm.* **331**, 1-10 (2007).
154. Green, M.R.*, et al.* Abraxane, a novel Cremophor-free, albumin-bound particle form of paclitaxel for the treatment of advanced non-small-cell lung cancer. *Ann. Oncol.* **17**, 1263-1268 (2006).
155. Choy, H. Taxanes in combined-modality therapy for solid tumors. *Oncology (Williston Park)* **13**, 23-38 (1999).
156. Hainsworth, J.D. Practical aspects of weekly docetaxel administration schedules. *Oncologist* **9**, 538-545 (2004).
157. Rowinsky, E.K., Cazenave, L.A. & Donehower, R.C. Taxol: a novel investigational antimicrotubule agent. *J. Natl. Cancer Inst.* **82**, 1247-1259 (1990).

158. Schiff, P.B. & Horwitz, S.B. Taxol stabilizes microtubules in mouse fibroblast cells. *Proc. Natl. Acad. Sci. U. S. A.* **77**, 1561-1565 (1980).
159. Authier, N., Gillet, J.P., Fialip, J., Eschalier, A. & Coudore, F. Assessment of neurotoxicity following repeated cremophor/ethanol injections in rats. *Neurotox Res* **3**, 301-306 (2001).
160. Authier, N., Gillet, J.P., Fialip, J., Eschalier, A. & Coudore, F. Description of a short-term Taxol (R)-induced nociceptive neuropathy in rats. *Brain Research* **887**, 239-249 (2000).
161. ten Tije, A.J., Verweij, J., Loos, W.J. & Sparreboom, A. Pharmacological effects of formulation vehicles - Implications for cancer chemotherapy. *Clinical Pharmacokinetics* **42**, 665-685 (2003).
162. van Zuylen, L., Verweij, J. & Sparreboom, A. Role of formulation vehicles in taxane pharmacology. *Investigational New Drugs* **19**, 125-141 (2001).
163. Ibrahim, N.K.*, et al.* Phase I and pharmacokinetic study of ABI-007, a Cremophor-free, protein-stabilized, nanoparticle formulation of paclitaxel. *Clin. Cancer Res.* **8**, 1038-1044 (2002).
164. Kratz, F. Albumin as a drug carrier: Design of prodrugs, drug conjugates and nanoparticles. *J. Controlled Release* **132**, 171-183 (2008).
165. Ghuman, J.*, et al.* Structural basis of the drug-binding specificity of human serum albumin. *J. Mol. Biol.* **353**, 38-52 (2005).
166. Desai, N. Nanoparticle albumin bound (nab) technology: targeting tumors through the endothelial gp60 receptor and SPARC. *Nanomedicine-Nanotechnology Biology and Medicine* **3**, 339-339 (2007).
167. Schnitzer, J.E. & Oh, P. Antibodies to Sparc Inhibit Albumin Binding to Sparc, Gp60, and Microvascular Endothelium. *American Journal of Physiology* **263**, H1872-H1879 (1992).
168. Vogel, S.M., Minshall, R.D., Pilipovic, M., Tiruppathi, C. & Malik, A.B. Albumin uptake and transcytosis in endothelial cells in vivo induced by albumin-binding protein. *Am. J. Physiol. Lung Cell. Mol. Physiol.* **281**, L1512-1522 (2001).
169. Desai, N., Trieu, V., Damascelli, B. & Soon-Shiong, P. SPARC Expression Correlates with Tumor Response to Albumin-Bound Paclitaxel in Head and Neck Cancer Patients. *Transl. Oncol.* **2**, 59-64 (2009).
170. Podhajcer, O.L.*, et al.* The role of the matricellular protein SPARC in the dynamic interaction between the tumor and the host. *Cancer Metastasis Rev.* **27**, 691-705 (2008).
171. Hawkins, M.J., Soon-Shiong, P. & Desai, N. Protein nanoparticles as drug carriers in clinical medicine. *Adv Drug Deliv Rev* **60**, 876-885 (2008).
172. Elzoghby, A.O., Samy, W.M. & Elgindy, N.A. Albumin-based nanoparticles as potential controlled release drug delivery systems. *J. Controlled Release* **157**, 168-182 (2012).
173. Bohidar, H.B. & Mohanty, B. Anomalous self-assembly of gelatin in ethanol-water marginal solvent. *Phys Rev E* **69**, - (2004).

174. Irache, J.M.a.E., Socorro. Biological and Pharmaceutical Nanomaterials. in *Nanotechnologies for the Life Sciences*, Vol. 2 (ed. Kumar, C.S.S.R.) (Wiley-VCH, 2006).
175. Mohanty, B. & Bohidar, H.B. Systematic of alcohol-induced simple coacervation in aqueous gelatin solutions. *Biomacromolecules* **4**, 1080-1086 (2003).
176. Weber, C., Coester, C., Kreuter, J. & Langer, K. Desolvation process and surface characterisation of protein nanoparticles. *Int. J. Pharm.* **194**, 91-102 (2000).
177. Merodio, M., Arnedo, A., Renedo, M.J. & Irache, J.M. Ganciclovir-loaded albumin nanoparticles: characterization and in vitro release properties. *Eur. J. Pharm. Sci.* **12**, 251-259 (2001).
178. Meziani, M.J. & Sun, Y.P. Protein-conjugated nanoparticles from rapid expansion of supercritical fluid solution into aqueous solution. *J. Am. Chem. Soc.* **125**, 8015-8018 (2003).
179. Langer, K.*, et al.* Optimization of the preparation process for human serum albumin (HSA) nanoparticles. *Int. J. Pharm.* **257**, 169-180 (2003).
180. Sharma, P., Brown, S., Walter, G., Santra, S. & Moudgil, B. Nanoparticles for Bioimaging. *Adv. Colloid Interface Sci.* **123-126**, 471-485 (2006).
181. Resch-Genger, U., Grabolle, M., Cavaliere-Jaricot, S., Nitschke, R. & Nann, T. Quantum dots versus organic dyes as fluorescent labels. *Nat. Methods* **5**, 763-775 (2008).
182. He, H., Xie, C. & Ren, J. Nonbleaching fluorescence of gold nanoparticles and its applications in cancer cell imaging. *Anal. Chem.* **80**, 5951-5957 (2008).
183. Kim, H.J., Lee, J., Kim, T.H., Lee, T.S. & Kim, J. Highly emissive self-assembled organic nanoparticles having dual color capacity for targeted immunofluorescence labeling. *Adv. Mater. (Weinheim, Ger.)* **20**, 1117-+ (2008).
184. Lim, S.F.*, et al.* In vivo and scanning electron microscopy imaging of upconverting nanophosphors in Caenorhabditis elegans. *Nano Lett.* **6**, 169-174 (2006).
185. Resch-Genger, U., Grabolle, M., Cavaliere-Jaricot, S., Nitschke, R. & Nann, T. Quantum dots versus organic dyes as fluorescent labels. *Nat. Methods* **5**, 763-775 (2008).
186. Derfus, A.M., Chan, W.C.W. & Bhatia, S.N. Probing the cytotoxicity of semiconductor quantum dots. *Nano Lett.* **4**, 11-18 (2004).
187. Hardman, R. A toxicologic review of quantum dots: Toxicity depends on physicochemical and environmental factors. *Environ. Health Perspect.* **114**, 165-172 (2006).
188. Wang, F.*, et al.* Synthesis of polyethylenimine/NaYF4 nanoparticles with upconversion fluorescence. *Nanotechnology* **17**, 5786-5791 (2006).
189. Luedtke, M.A., Papazoglou, E., Neidrauer, M. & Kollias, N. Wavelength effects on contrast observed with reflectance in vivo confocal laser scanning microscopy. *Skin Research and Technology* **15**, 482-488 (2009).
190. Meinhardt, M., Krebs, R., Anders, A., Heinrich, U. & Tronnier, H. Wavelength-dependent penetration depths of ultraviolet radiation in human skin. *Journal of Biomedical Optics* **13**, - (2008).

191. de Chermont, Q.L., *et al.* Nanoprobes with near-infrared persistent luminescence for in vivo imaging. *Proc. Natl. Acad. Sci. U. S. A.* **104**, 9266-9271 (2007).
192. Chatteriee, D.K., Rufalhah, A.J. & Zhang, Y. Upconversion fluorescence imaging of cells and small animals using lanthanide doped nanocrystals. *Biomaterials* **29**, 937-943 (2008).
193. Meiser, F., Cortez, C. & Caruso, F. Biofunctionalization of fluorescent rare-earth-doped lanthanum phosphate colloidal nanoparticles. *Angew. Chem. Int. Ed.* **43**, 5954-5957 (2004).
194. Kramer, K.W., *et al.* Hexagonal sodium yttrium fluoride based green and blue emitting upconversion phosphors. *Chem. Mater.* **16**, 1244-1251 (2004).
195. Suyver, J.F., *et al.* Upconversion spectroscopy and properties of NaYF4 doped with Er (3+), Tm3+ and/or Yb3+. *J. Lumin.* **117**, 1-12 (2006).
196. Li, Z.Q. & Zhang, Y. Monodisperse silica-coated polyvinylpyrrolidone/NaYF4 nanocrystals with multicolor upconversion fluorescence emission. *Angew. Chem. Int. Ed.* **45**, 7732-7735 (2006).
197. Larson, D.R., *et al.* Water-soluble quantum dots for multiphoton fluorescence imaging in vivo. *Science* **300**, 1434-1436 (2003).
198. Abdul Jalil, R. & Zhang, Y. Biocompatibility of silica coated NaYF(4) upconversion fluorescent nanocrystals. *Biomaterials* **29**, 4122-4128 (2008).
199. Idris, N.M., *et al.* Tracking transplanted cells in live animal using upconversion fluorescent nanoparticles. *Biomaterials* **30**, 5104-5113 (2009).
200. Kumar, R., Nyk, M., Ohulchanskyy, T.Y., Flask, C.A. & Prasad, P.N. Combined Optical and MR Bioimaging Using Rare Earth Ion Doped NaYF4 Nanocrystals. *Adv. Funct. Mater.* **19**, 853-859 (2009).
201. Schafer, H., Ptacek, P., Kompe, K. & Haase, M. Lanthanide-doped NaYF4 nanocrystals in aqueous solution displaying strong up-conversion emission. *Chem. Mater.* **19**, 1396-1400 (2007).
202. Godbey, W.T., Wu, K.K. & Mikos, A.G. Poly(ethylenimine) and its role in gene delivery. *Journal of Controlled Release* **60**, 149-160 (1999).
203. Irache, J.M., *et al.* Albumin nanoparticles for the intravitreal delivery of anticytomegaloviral drugs. *Mini Rev. Med. Chem.* **5**, 293-305 (2005).
204. Mo, Y., Barnett, M.E., Takemoto, D., Davidson, H. & Kompella, U.B. Human serum albumin nanoparticles for efficient delivery of Cu, Zn superoxide dismutase gene. *Mol. Vis.* **13**, 746-757 (2007).
205. Ogawara, K., *et al.* Pre-coating with serum albumin reduces receptor-mediated hepatic disposition of polystyrene nanosphere: implications for rational design of nanoparticles. *J. Controlled Release* **100**, 451-455 (2004).
206. Roser, M., Fischer, D. & Kissel, T. Surface-modified biodegradable albumin nano- and microspheres. II: effect of surface charges on in vitro phagocytosis and biodistribution in rats. *Eur. J. Pharm. Biopharm.* **46**, 255-263 (1998).
207. Anhorn, M.G., Wagner, S., Kreuter, J., Langer, K. & von Briesen, H. Specific targeting of HER2 overexpressing breast cancer cells with doxorubicin-loaded trastuzumab-modified human serum albumin nanoparticles. *Bioconjug. Chem.* **19**, 2321-2331 (2008).

208. Kreuter, J., *et al.* Covalent attachment of apolipoprotein A-I and apolipoprotein B-100 to albumin nanoparticles enables drug transport into the brain. *J. Control. Release* **118**, 54-58 (2007).
209. Michaelis, K., *et al.* Covalent linkage of apolipoprotein e to albumin nanoparticles strongly enhances drug transport into the brain. *J. Pharmacol. Exp. Ther.* **317**, 1246-1253 (2006).
210. Rhaese, S., von Briesen, H., Rubsamen-Waigmann, H., Kreuter, J. & Langer, K. Human serum albumin-polyethylenimine nanoparticles for gene delivery. *J. Control. Release* **92**, 199-208 (2003).
211. Spankuch, B., *et al.* Downregulation of Plk1 expression by receptor-mediated uptake of antisense oligonucleotide-loaded nanoparticles. *Neoplasia* **10**, 223-234 (2008).
212. Wartlick, H., Spankuch-Schmitt, B., Strebhardt, K., Kreuter, J. & Langer, K. Tumour cell delivery of antisense oligonuclceotides by human serum albumin nanoparticles. *J. Control. Release* **96**, 483-495 (2004).
213. Sedgewick, J. *Scientific Imaging with Photoshop: Methods, Measurement, and Output*, (New Riders, Berkeley, CA, 2008).
214. Majoros, A., *et al.* Analysis of risk factors for urinary incontinence after radical prostatectomy. *Urol. Int.* **78**, 202-207 (2007).
215. Fester, T., Berg, R.H. & Taylor, C.G. An easy method using glutaraldehyde-introduced fluorescence for the microscopic analysis of plant biotrophic interactions. *Journal of Microscopy-Oxford* **231**, 342-348 (2008).
216. Fukushima, Y., Ohnishi, T., Arita, N., Hayakawa, T. & Sekiguchi, K. Integrin alpha3beta1-mediated interaction with laminin-5 stimulates adhesion, migration and invasion of malignant glioma cells. *Int. J. Cancer* **76**, 63-72 (1998).
217. Allman, R., Cowburn, P. & Mason, M. In vitro and in vivo effects of a cyclic peptide with affinity for the alpha(nu)beta3 integrin in human melanoma cells. *Eur. J. Cancer* **36**, 410-422 (2000).
218. Wilson, O.C., Blair, E., Kennedy, S., Rivera, G. & Mehl, P. Surface modification of magnetic nanoparticles with oleylamine and gum Arabic. *Materials Science & Engineering C-Biomimetic and Supramolecular Systems* **28**, 438-442 (2008).
219. Hynes, R.O. Integrins: bidirectional, allosteric signaling machines. *Cell* **110**, 673-687 (2002).
220. Zhao, Y., *et al.* Tumor alphavbeta3 integrin is a therapeutic target for breast cancer bone metastases. *Cancer Res* **67**, 5821-5830 (2007).
221. McCabe, N.P., De, S., Vasanji, A., Brainard, J. & Byzova, T.V. Prostate cancer specific integrin alphavbeta3 modulates bone metastatic growth and tissue remodeling. *Oncogene* **26**, 6238-6243 (2007).
222. Avraamides, C.J., Garmy-Susini, B. & Varner, J.A. Integrins in angiogenesis and lymphangiogenesis. *Nat Rev Cancer* **8**, 604-617 (2008).
223. Brooks, P.C., *et al.* Integrin alpha v beta 3 antagonists promote tumor regression by inducing apoptosis of angiogenic blood vessels. *Cell* **79**, 1157-1164 (1994).
224. Kumar, C.C., *et al.* Inhibition of angiogenesis and tumor growth by SCH221153, a dual alpha(v)beta3 and alpha(v)beta5 integrin receptor antagonist. *Cancer Res* **61**, 2232-2238 (2001).

225. Abdollahi, A., *et al.* Inhibition of alpha(v)beta3 integrin survival signaling enhances antiangiogenic and antitumor effects of radiotherapy. *Clin. Cancer Res.* **11**, 6270-6279 (2005).
226. Ramos, O.H., *et al.* A novel alpha(v)beta (3)-blocking disintegrin containing the RGD motive, DisBa-01, inhibits bFGF-induced angiogenesis and melanoma metastasis. *Clin. Exp. Metastasis* **25**, 53-64 (2008).
227. Gladson, C.L., *et al.* Stage-specific expression of integrin alphaVbeta3 in neuroblastic tumors. *Am J Pathol* **148**, 1423-1434 (1996).
228. Veeravagu, A., *et al.* Integrin alphavbeta3-targeted radioimmunotherapy of glioblastoma multiforme. *Clin. Cancer Res.* **14**, 7330-7339 (2008).
229. Tucker, G.C. Integrins: molecular targets in cancer therapy. *Curr. Oncol. Rep.* **8**, 96-103 (2006).
230. Buerkle, M.A., *et al.* Inhibition of the alpha-nu integrins with a cyclic RGD peptide impairs angiogenesis, growth and metastasis of solid tumours in vivo. *Br J Cancer* **86**, 788-795 (2002).
231. Fu, Y., *et al.* Angiogenesis inhibition and choroidal neovascularization suppression by sustained delivery of an integrin antagonist, EMD478761. *Invest. Ophthalmol. Vis. Sci.* **48**, 5184-5190 (2007).
232. Ghosh, P. & Patra, A. Influence of Crystal Phase and Excitation Wavelength on Luminescence Properties of Eu3+-Doped Sodium Yttrium Fluoride Nanocrystals. *J. Phys. Chem. C* **112**, 19283-19292 (2008).
233. Zhang, Q. & Zhang, Q.M. Synthesis and photoluminescent properties of alpha-NaYF4:Nd/alpha-NaYF4 core/shell nanostructure with enhanced near infrared (NIR) emission. *Mater. Lett.* **63**, 376-378 (2009).
234. Zensi, A., *et al.* Albumin nanoparticles targeted with Apo E enter the CNS by transcytosis and are delivered to neurones. *J. Control. Release* **137**, 78-86 (2009).
235. Bashkatov, A.N., Genina, E.A., Kochubey, V.I. & Tuchin, V.V. Optical properties of the subcutaneous adipose tissue in the spectral range 400-2500 nm. *Optics and Spectroscopy* **99**, 836-842 (2005).
236. Zonios, G., Bykowski, J. & Kollias, N. Skin melanin, hemoglobin, and light scattering properties can be quantitatively assessed in vivo using diffuse reflectance spectroscopy. *Journal of Investigative Dermatology* **117**, 1452-1457 (2001).
237. Hilderbrand, S.A. & Weissleder, R. Near-infrared fluorescence: application to in vivo molecular imaging. *Current Opinion in Chemical Biology* **14**, 71-79 (2010).
238. Weissleder, R. & Ntziachristos, V. Shedding light onto live molecular targets. *Nat Med* **9**, 123-128 (2003).
239. Welsher, K., Sherlock, S.P. & Dai, H. Deep-tissue anatomical imaging of mice using carbon nanotube fluorophores in the second near-infrared window. *Proc Natl Acad Sci U S A* **108**, 8943-8948 (2011).
240. Smith, A.M., Mancini, M.C. & Nie, S.M. BIOIMAGING Second window for in vivo imaging. *Nat. Nanotechnol.* **4**, 710-711 (2009).
241. Rogach, A.L., Eychmuller, A., Hickey, S.G. & Kershaw, S.V. Infrared-emitting colloidal nanocrystals: synthesis, assembly, spectroscopy, and applications. *Small* **3**, 536-557 (2007).

242. Hardman, R. A toxicologic review of quantum dots: toxicity depends on physicochemical and environmental factors. *Environ Health Perspect* **114**, 165-172 (2006).
243. Welsher, K.*, et al.* A route to brightly fluorescent carbon nanotubes for near-infrared imaging in mice. *Nat Nanotechnol* **4**, 773-780 (2009).
244. Dai, H.J.*, et al.* High performance in vivo near-IR (> 1 μm) imaging and photothermal cancer therapy with carbon nanotubes. *Nano Research* **3**, 779-793 (2010).
245. Schrock, E.*, et al.* Multicolor spectral karyotyping of human chromosomes. *Science* **273**, 494-497 (1996).
246. Medintz, I.L., Uyeda, H.T., Goldman, E.R. & Mattoussi, H. Quantum dot bioconjugates for imaging, labelling and sensing. *Nat. Mater.* **4**, 435-446 (2005).
247. Levenson, R.M., Lynch, D.T., Kobayashi, H., Backer, J.M. & Backer, M.V. Multiplexing with multispectral imaging: From mice to microscopy. *ILAR J.* **49**, 78-88 (2008).
248. Zavaleta, C.L.*, et al.* Multiplexed imaging of surface enhanced Raman scattering nanotags in living mice using noninvasive Raman spectroscopy. *Proc. Natl. Acad. Sci. U. S. A.* **106**, 13511-13516 (2009).
249. Ito, Y., Kennan, R.P., Watanabe, E. & Koizumi, H. Assessment of heating effects in skin during continuous wave near infrared spectroscopy. *J. Biomed. Opt.* **5**, 383-390 (2000).
250. Hirano, S. & Suzuki, K.T. Exposure, metabolism, and toxicity of rare earths and related compounds. *Environmental Health Perspectives* **104**, 85-95 (1996).
251. Jalil, R.A. & Zhang, Y. Biocompatibility of silica coated NaYF4 upconversion fluorescent nanocrystals. *Biomaterials* **29**, 4122-4128 (2008).
252. Zhou, J.C.*, et al.* Bioimaging and toxicity assessments of near-infrared upconversion luminescent NaYF4:Yb,Tm nanocrystals. *Biomaterials* **32**, 9059-9067 (2011).
253. Naczynski, D.J.*, et al.* Albumin Nanoshell Encapsulation of Near-Infrared-Excitable Rare-Earth Nanoparticles Enhances Biocompatibility and Enables Targeted Cell Imaging. *Small* **6**, 1631-1640 (2010).
254. Tan, M.C., Al-Baroudi, L. & Riman, R.E. Surfactant Effects on Efficiency Enhancement of Infrared-to-Visible Upconversion Emissions of NaYF(4):Yb-Er. *Acs Applied Materials & Interfaces* **3**, 3910-3915 (2011).
255. Tan, M.C., Connolly, J. & Riman, R.E. Optical Efficiency of Short Wave Infrared Emitting Phosphors. *Journal of Physical Chemistry C* **115**, 17952-17957 (2011).
256. Chen, S.*, et al.* Melanoma mouse model implicates metabotropic glutamate signaling in melanocytic neoplasia. *Nature Genetics* **34**, 108-112 (2003).
257. Smith, A.M., Mancini, M.C. & Nie, S. Bioimaging: second window for in vivo imaging. *Nat Nanotechnol* **4**, 710-711 (2009).
258. Chen, C.*, et al.* A primary method for determination of optical parameters of turbid samples and application to intralipid between 550 and 1630nm. *Optics Express* **14**, 7420-7435 (2006).
259. McDonald, D.M. & Choyke, P.L. Imaging of angiogenesis: from microscope to clinic. *Nat Med* **9**, 713-725 (2003).

260. Sanz, J. & Fayad, Z.A. Imaging of atherosclerotic cardiovascular disease. *Nature* **451**, 953-957 (2008).
261. Haglund, M.M., Hochman, D.W., Spence, A.M. & Berger, M.S. Enhanced Optical Imaging of Rat Gliomas and Tumor Margins. *Neurosurgery* **35**, 930-940 (1994).
262. He, X., Gao, J., Gambhir, S.S. & Cheng, Z. Near-infrared fluorescent nanoprobes for cancer molecular imaging: status and challenges. *Trends Mol. Med.* **16**, 574-583.
263. Sparreboom, A.*, et al.* Cremophor EL-mediated alteration of paclitaxel distribution in human blood: Clinical pharmacokinetic implications. *Cancer Res.* **59**, 1454-1457 (1999).
264. Desai, N., Trieu, V., Damascelli, B. & Soon-Shiong, P. SPARC Expression Correlates with Tumor Response to Albumin-Bound Paclitaxel in Head and Neck Cancer Patients. *Translational Oncology* **2**, 59-64 (2009).
265. Desai, N., Trieu, V. & Yao, Z. Increased antitumor activity, intratumor paclitaxel concentrations, and endothelial cell transport of cremophor-free, albumin-bound paclitaxel, ABI-007, compared with cremophor-based paclitaxel (vol 12, pg 1317, 2006). *Clinical Cancer Research* **12**, 3869-3869 (2006).
266. Podhajcer, O.L.*, et al.* The role of the matricellular protein SPARC in the dynamic interaction between the tumor and the host. *Cancer and Metastasis Reviews* **27**, 691-705 (2008).
267. Stehle, G.*, et al.* Plasma protein (albumin) catabolism by the tumor itself - implications for tumor metabolism and the genesis of cachexia. *Crit. Rev. Oncol. Hematol.* **26**, 77-100 (1997).
268. Alexis, F., Pridgen, E., Molnar, L.K. & Farokhzad, O.C. Factors affecting the clearance and biodistribution of polymeric nanoparticles. *Mol. Pharm.* **5**, 505-515 (2008).
269. Rao, J.H. Shedding Light on Tumors Using Nanoparticles. *ACS Nano* **2**, 1984-1986 (2008).
270. Davis, M.E., Chen, Z.G. & Shin, D.M. Nanoparticle therapeutics: an emerging treatment modality for cancer. *Nat Rev Drug Discov* **7**, 771-782 (2008).
271. Hobbs, S.K.*, et al.* Regulation of transport pathways in tumor vessels: Role of tumor type and microenvironment. *Proceedings of the National Academy of Sciences of the United States of America* **95**, 4607-4612 (1998).
272. Vogel, S.M., Minshall, R.D., Pilipovic, M., Tiruppathi, C. & Malik, A.B. Albumin uptake and transcytosis in endothelial cells in vivo induced by albumin-binding protein. *American Journal of Physiology-Lung Cellular and Molecular Physiology* **281**, L1512-L1522 (2001).
273. Lipinski, C.A., Lombardo, F., Dominy, B.W. & Feeney, P.J. Experimental and computational approaches to estimate solubility and permeability in drug discovery and development settings. *Advanced Drug Delivery Reviews* **46**, 3-26 (2001).
274. Rabinow, B.E. Nanosuspensions in drug delivery. *Nature Reviews Drug Discovery* **3**, 785-796 (2004).

275. Hambley, T.W. Is Anticancer Drug Development Heading in the Right Direction? *Cancer Research* **69**, 1259-1261 (2009).
276. Tannock, I.F., Lee, C.M., Tunggal, J.K., Cowan, D.S.M. & Egorin, M.J. Limited penetration of anticancer drugs through tumor tissue: A potential cause of resistance of solid tumors to chemotherapy. *Clinical Cancer Research* **8**, 878-884 (2002).
277. Gottesman, M.M., Fojo, T. & Bates, S.E. Multidrug resistance in cancer: Role of ATP-dependent transporters. *Nature Reviews Cancer* **2**, 48-58 (2002).
278. Morgillo, F. & Lee, H.Y. Resistance to epidermal growth factor receptor-targeted therapy. *Drug Resistance Updates* **8**, 298-310 (2005).
279. Smalley, K.S.M.*, et al.* Multiple signaling pathways must be targeted to overcome drug resistance in cell lines derived from melanoma metastases. *Molecular Cancer Therapeutics* **5**, 1136-1144 (2006).
280. Flaherty, K.T.*, et al.* Inhibition of Mutated, Activated BRAF in Metastatic Melanoma. *New England Journal of Medicine* **363**, 809-819 (2010).
281. Hawkins, M.J., Soon-Shiong, P. & Desai, N. Protein nanoparticles as drug carriers in clinical medicine. *Advanced Drug Delivery Reviews* **60**, 876-885 (2008).
282. Gelderblom, H., Verweij, J., Nooter, K. & Sparreboom, A. Cremophor EL: the drawbacks and advantages of vehicle selection for drug formulation. *European Journal of Cancer* **37**, 1590-1598 (2001).
283. Kearns, C.M. Pharmacokinetics of the taxanes. *Pharmacotherapy* **17**, S105-S109 (1997).
284. Mross, K., Hollander, N., Hauns, B., Schumacher, M. & Maier-Lenz, H. The pharmacokinetics of a 1-h paclitaxel infusion. *Cancer Chemotherapy and Pharmacology* **45**, 463-470 (2000).
285. Cortes, J. & Saura, C. Nanoparticle albumin-bound (nab (TM))-paclitaxel: improving efficacy and tolerability by targeted drug delivery in metastatic breast cancer. *Ejc Supplements* **8**, 1-10 (2010).
286. Ferrari, M. Cancer nanotechnology: opportunities and challenges. *Nat Rev Cancer* **5**, 161-171 (2005).
287. Cho, K.J., Wang, X., Nie, S.M., Chen, Z. & Shin, D.M. Therapeutic nanoparticles for drug delivery in cancer. *Clinical Cancer Research* **14**, 1310-1316 (2008).
288. Larsen, A.K., Escargueil, A.E. & Skladanowski, A. Resistance mechanisms associated with altered intracellular distribution of anticancer agents. *Pharmacology & Therapeutics* **85**, 217-229 (2000).
289. Cirstea, D.*, et al.* Dual Inhibition of Akt/Mammalian Target of Rapamycin Pathway by Nanoparticle Albumin-Bound-Rapamycin and Perifosine Induces Antitumor Activity in Multiple Myeloma. *Molecular Cancer Therapeutics* **9**, 963-975 (2010).
290. Allen, T.M. & Cullis, P.R. Drug delivery systems: Entering the mainstream. *Science* **303**, 1818-1822 (2004).
291. Maeda, H. The enhanced permeability and retention (EPR) effect in tumor vasculature: The key role of tumor-selective macromolecular drug targeting. *Advances in Enzyme Regulation, Vol 41* **41**, 189-207 (2001).

292. Allen, T.M. Ligand-targeted therapeutics in anticancer therapy. *Nature Reviews Cancer* **2**, 750-763 (2002).
293. Sugahara, K.N.*, et al.* Tissue-penetrating delivery of compounds and nanoparticles into tumors. *Cancer Cell* **16**, 510-520 (2009).
294. Goodman, T.T., Olive, P.L. & Pun, S.H. Increased nanoparticle penetration in collagenase-treated multicellullar spheroids. *International Journal of Nanomedicine* **2**, 265-274 (2007).
295. Ibrahim, N.K.*, et al.* Multicenter phase II trial of ABI-007, an albumin-bound paclitaxel, in women with metastatic breast cancer. *Journal of Clinical Oncology* **23**, 6019-6026 (2005).
296. Harries, M., Ellis, P. & Harper, P. Nanoparticle albumin-bound paclitaxel for metastatic breast cancer. *Journal of Clinical Oncology* **23**, 7768-7771 (2005).
297. Fasano, M.*, et al.* The extraordinary ligand binding properties of human serum albumin. *Iubmb Life* **57**, 787-796 (2005).
298. Gottesman, M.M. Mechanisms of cancer drug resistance. *Annual Review of Medicine* **53**, 615-627 (2002).
299. Hu, C.M.J. & Zhang, L.F. Therapeutic Nanoparticles to Combat Cancer Drug Resistance. *Current Drug Metabolism* **10**, 836-841 (2009).
300. Primeau, A.J., Rendon, A., Hedley, D., Lilge, L. & Tannock, I.F. The distribution of the anticancer drug doxorubicin in relation to blood vessels in solid tumors. *Clinical Cancer Research* **11**, 8782-8788 (2005).
301. Lu, P.F., Weaver, V.M. & Werb, Z. The extracellular matrix: A dynamic niche in cancer progression. *Journal of Cell Biology* **196**, 395-406 (2012).
302. Szakacs, G., Paterson, J.K., Ludwig, J.A., Booth-Genthe, C. & Gottesman, M.M. Targeting multidrug resistance in cancer. *Nature Reviews Drug Discovery* **5**, 219-234 (2006).
303. Kuhn, S.J., Finch, S.K., Hallahan, D.E. & Giorgio, T.D. Proteolytic surface functionalization enhances in vitro magnetic nanoparticle mobility through extracellular matrix. *Nano Letters* **6**, 306-312 (2006).
304. Aggarwal, B.B. & Sung, B. Pharmacological basis for the role of curcumin in chronic diseases: an age-old spice with modern targets. *Trends in Pharmacological Sciences* **30**, 85-94 (2009).
305. Bush, J.A., Cheung, K.J., Jr. & Li, G. Curcumin induces apoptosis in human melanoma cells through a Fas receptor/caspase-8 pathway independent of p53. *Exp Cell Res* **271**, 305-314 (2001).
306. Odot, J.*, et al.* In vitro and in vivo anti-tumoral effect of curcumin against melanoma cells. *Int J Cancer* **111**, 381-387 (2004).
307. Garg, A.K., Buchholz, T.A. & Aggarwal, B.B. Chemosensitization and radiosensitization of tumors by plant polyphenols. *Antioxidants & Redox Signaling* **7**, 1630-1647 (2005).
308. Anand, P., Kunnumakkara, A.B., Newman, R.A. & Aggarwal, B.B. Bioavailability of curcumin: Problems and promises. *Molecular Pharmaceutics* **4**, 807-818 (2007).
309. Pollock, P.M.*, et al.* Melanoma mouse model implicates metabotropic glutamate signaling in melanocytic neoplasia. *Nat Genet* **34**, 108-112 (2003).

310. J. Namkoong, S.S.S., H. J. Lee, Y. E. Marin, B. A. Wall, J. S. Goydos, S. Chen,. Metabotropic Glutamate Receptor 1 and Glutamate Signaling in Human Melanoma. *cancer research*, 2298-2305 (2007).
311. Alelyunas, Y.W.*, et al.* Experimental solubility profiling of marketed CNS drugs, exploring solubility limit of CNS discovery candidate. *Bioorganic & Medicinal Chemistry Letters* **20**, 7312-7316 (2010).
312. Timmins, N.E., Dietmair, S. & Nielsen, L.K. Hanging-drop multicellular spheroids as a model of tumour angiogenesis. *Angiogenesis* **7**, 97-103 (2004).
313. Sutherland, R.M. Cell and environment interactions in tumor microregions: the multicell spheroid model. *Science* **240**, 177-184 (1988).
314. Bond, M.D. & Vanwart, H.E. Purification and Separation of Individual Collagenases of Clostridium-Histolyticum Using Red-Dye Ligand Chromatography. *Biochemistry* **23**, 3077-3085 (1984).
315. Bond, M.D. & Vanwart, H.E. Characterization of the Individual Collagenases from Clostridium-Histolyticum. *Biochemistry* **23**, 3085-3091 (1984).
316. Vertegel, A.A., Siegel, R.W. & Dordick, J.S. Silica nanoparticle size influences the structure and enzymatic activity of adsorbed lysozyme. *Langmuir* **20**, 6800-6807 (2004).
317. Petros, R.A. & DeSimone, J.M. Strategies in the design of nanoparticles for therapeutic applications. *Nat Rev Drug Discov* **9**, 615-627 (2010).
318. Bertucci, C. & Domenici, E. Reversible and covalent binding of drugs to human serum albumin: Methodological approaches and physiological relevance. *Curr. Med. Chem.* **9**, 1463-1481 (2002).
319. Karasic, T.B., Hei, T.K. & Ivanov, V.N. Disruption of IGF-1R signaling increases TRAIL-induced apoptosis: a new potential therapy for the treatment of melanoma. *Exp. Cell Res.* **316**, 1994-2007 (2010).
320. Cardones, A.R., Murakami, T. & Hwang, S.T. CXCR4 enhances adhesion of B16 tumor cells to endothelial cells in vitro and in vivo via beta-1 integrin. *Cancer Res.* **63**, 6751-6757 (2003).
321. Scala, S., Ottaiano, A. & Ascierto, P.A. Expression of CXCR4 predicts poor prognosis in patients with malignant melanoma. *Clin. Cancer Res.* **11**, 1835-1841 (2005).
322. Bensimon, G., Lacomblez, L. & Meininger, V. A controlled trial of riluzole in amyotrophic lateral sclerosis. *N. Engl. J. Med.* **3**, 585-591 (1994).
323. Namkoong, J.*, et al.* Metabotropic glutamate receptor 1 and glutamate signaling in human melanoma. *Cancer Res* **67**, 2298-2305 (2007).
324. Yip, D.*, et al.* A phase 0 trial of Riluzole in patients with resectable stage III and IV melanoma. *Clin. Cancer Res.* **15**, 3896-3902 (2009).
325. Zhang, H., Xu, D., Huang, Y. & Duan, X.F. Highly spectral dependent enhancement of upconversion emission with sputtered gold island films. *Chem. Commun.* **47**, 979-981 (2011).
326. Prahl, S.A., Vangemert, M.J.C. & Welch, A.J. Determining the Optical-Properties of Turbid Media by Using the Adding-Doubling Method. *Appl. Opt.* **32**, 559-568 (1993).

327. Simpson, C.R., Kohl, M., Essenpreis, M. & Cope, M. Near-infrared optical properties of ex vivo human skin and subcutaneous tissues measured using the Monte Carlo inversion technique. *Phys. Med. Biol.* **43**, 2465-2478 (1998).
328. Prahl, S.A. Everything I think you should know about inverse adding-doubling. (Oregon Medical Laser Center, St. Vincent Hospital 2011).
329. Liu, J.-n.*, et al.* Simultaneous nuclear imaging and intranuclear drug delivery by nuclear-targeted multifunctional upconversion nanoprobes. *Biomaterials* **33**, 7282-7290.
330. Zhou, J.*, et al.* Dual-modality in vivo imaging using rare-earth nanocrystals with near-infrared to near-infrared (NIR-to-NIR) upconversion luminescence and magnetic resonance properties. *Biomaterials* **31**, 3287-3295 (2010).
331. Ogan, M.D.*, et al.* Albumin Labeled with Gd-Dtpa - an Intravascular Contrast-Enhancing Agent for Magnetic-Resonance Blood Pool Imaging - Preparation and Characterization. *Investig. Radiol.* **22**, 665-671 (1987).
332. Wang, L.V. Multiscale photoacoustic microscopy and computed tomography. *Nat. Photonics* **3**, 503-509 (2009).
333. Banerjee, S.S. & Chen, D.H. A multifunctional magnetic nanocarrier bearing fluorescent dye for targeted drug delivery by enhanced two-photon triggered release. *Nanotechnology* **20**(2009).

CURRICULUM VITAE
DOMINIK JAN NACZYNSKI

EDUCATION

RUTGERS UNIVERSITY, Piscataway, NJ October 2012
- Ph.D. in chemical and biochemical engineering
- NIH Biotechnology Predoctoral Training Fellow

CORNELL UNIVERSITY, Ithaca, NY May 2006
- Bachelor of Science in chemical and biomolecular engineering
- Minor in biomedical engineering

EXPERIENCE

RUTGERS UNIVERSITY, Piscataway, NJ 2006-2012
- Graduate research assistant to Drs. Prabhas Moghe and Charles Roth
- Co-author of an R-21 grant proposal (NIH R21 EB015169-01)
- Teaching assistant and undergraduate mentor

NCI CANCER RESEARCH IMAGING CAMP, Nashville, TN June 2012
- Participant of a special intensive course on cancer imaging

HOFFMAN-LA ROCHE INC., Nutley, NJ June 2008-August 2008
- Senior scientific intern in pharmaceutical and analytical R & D

PUBLICATIONS AND PATENTS

D. J. Naczynski*, T. Andelman*, D. Pal, S. Chen, R. E. Riman, C. M. Roth, P. V. Moghe, "Albumin nanoshell encapsulation of near-infrared-excitable rare-earth nanoparticles enhances biocompatibility and enables targeted cell imaging", *Small*, 2010, *6*, 1631. **(Featured on Cover)** 2010 ISI Impact Factor: 7.33

D. J. Naczynski, M. Tan, M. Zevon, B. Wall, J. Kohl, T. Kulesa, S. Chen, R. Riman, C. Roth, P. Moghe, "Rare-earth doped nanoparticles as bioactive probes for shortwave infrared in vivo imaging". *(In Preparation for submission to Nature Nanotechnology, Expected Submission Date: September 2012)*

D. J. Naczynski, **M. Zevon, M. Cui, C.M. Roth, P.V. Moghe**, "Collagenase modified albumin nanoparticles for enhanced tumor penetration and multi-drug delivery". *(In Preparation for submission to Advanced Functional Materials, Expected Submission Date: October 2012)*

B. Paladini, **D. J. Naczynski**, P. V. Moghe, L. Fabris, Gold Nanoparticle "Dimers for SERS-based Targeted Detection of Human Glioblastoma Cells". *(In Preparation for submission to Advanced Materials, Expected Submission Date: October 2012)*

D. J. Naczynski, M. C. Tan, C. M. Roth, R. Riman, P. V. Moghe. 2012. Multifunctional infrared-emitting composites. USA. Patent filed May 2012.